Charles University

Faculty of Science

Study programme: Geology

Study subject: Geology

Bc. Václav Santolík

Petrogenesis and evolution of the Davle Volcanic Complex

Vznik a vývoj davelského vulkanického komplexu

Diploma thesis

Supervisor: doc. Mgr. Lukáš Ackerman, PhD.

Consultant: doc. RNDr. Václav Kachlík, CSc.

Prague, 2021

Prohlašuji, že jsem závěrečnou práci zpracoval samostatně a že jsem uvedl všechny použité informační zdroje a literaturu. Tato práce ani její podstatná část nebyla předložena k získání jiného nebo stejného akademického titulu.

Praha, 18. května 2021 .....

Acknowledgments

I would like to thank my supervisor Lukáš Ackerman for thorough guidance, giving me the opportunity to be familiar with many analytical methods and for inspiring discussions. Next, I want to thank my consultant Václav Kachlík for leading me during fieldwork, providing me insight into the regional geology and helping with petrography. I also thank Jiří Sláma for consultation regarding geochronological methods and tutoring me in zircon separation. Noemi Mesároszová is acknowledged for thorough and professional assistance with mineral microprobe analysis and Jan Rejšek for TIMS operation and his resounding laugh. I am also grateful to other colleagues from the Institute of the Geology of the Czech Academy of Sciences where I conducted most of my research and my family for their kind support.

Abstract

The Davle Volcanic Complex (DVC) situated in the Teplá-Barrandian unit (TBU) of the Bohemian Massif, is considered as a Neoproterozoic–Cambrian magmatic arc that developed on the northern active margin of Gondwana supercontinent during Cadomian accretionary orogeny. This study combines data obtained from fieldwork, petrography, rock-forming mineral microanalysis, major and trace element analysis, Sr–Nd–Pb isotopic systematics and U–Pb zircon geochronology in order to reveal the petrogenesis and evolution of the DVC. At least three-stage metamorphism including Cadomian seafloor alteration, Variscan regional metamorphism as well as contact metamorphism related to the emplacement of the Central Bohemian Plutonic Complex affected the DVC. The studied rocks follow calc-alkaline trend whereas tholeiitic trend previously reported is rather related to younger magmatic events. The northern part of the DVC is dominated by felsic subvolcanic (plagiogranite), volcanic (dacite-rhyolite) and pyroclastic (dacitic-rhyolitic tuffs and breccias) rocks with a few outcrops of basaltic andesite-andesite pillow lavas documenting the subaqueous activity of the DVC. These rocks are Na-rich, but K-poor, the plagiogranite contains albite most likely primary in origin, and exhibit highly radiogenic ε_{Nd} values (~ +6 to +11), enrichment in large-ion lithophile elements, but depletion in high-field strength elements that collectively argue for their derivation from a depleted mantle source fluxed by subduction-related fluids characteristic for an intra-oceanic subduction (island arc) geotectonic setting. Geochemical modelling indicates that the origin of plagiogranite and related rhyolite by fractionation of the pillow lavas is unlikely. By contrast, their formation can be best explained by ~20% melting of subduction-related metasomatized mantle and subsequent high degree of fractional crystallization. The southern section of the DVC is dominated by orthogneiss and related volcanic and pyroclastic rocks. New ICP-MS U–Pb zircon geochronological data constrained age of these rocks at 608 ± 8 Ma for the mafic orthogneiss and 637 ± 11 Ma for a rhyolite dyke cross-cutting the felsic orthogneiss, the latter being influenced by zircon inheritance. Compared to the rocks from the northern DVC section, the orthogneiss has higher K, Rb, Ba, Th, U and LREE concentrations but lower Na_2O contents, which together with their overall negative ε_{Nd} values (–5.1 to –3.1) indicate their derivation from an evolved (Gondwana?) continental crust. Geochemical modelling suggests that these rocks can be produced by fractional crystallization of andesite lavas/dykes widespread in the DVC with enhanced degrees of assimilation of continental crust. The andesites, present in both (north and south) sections, show subduction-related trace element characteristics and ε_{Nd} values ranging from –1.5 to +3.6 arguing for a complex evolution of their source. The whole volcanic sequence is penetrated by boninite dykes with ε_{Nd} values of +3.7 to +5.8 that formed by high degree melting of depleted mantle caused by slab break-off and associated heat increase of parental mantle source due to influence of asthenospheric mantle. Based on the data collected, a new preliminary geotectonic model for the Neoproterozoic–Cambrian evolution of the DVC is presented interpreting the northern DVC section as an island arc while the southern DVC section is representative for a continental arc. These two sections are considered as spatially separated segments within the Cadomian orogen.

Abstrakt

Davelský vulkanický komplex (DVC), který je součástí tepelsko-barrandienské jednotky Českého masivu, představuje vulkanický oblouk neoproterozoického až kambrického stáří, zformovaný během kadomské akreční orogeneze na severním okraji superkontinentu Gondwana. Tato diplomová práce kombinuje data získaná z terénního výzkumu, petrografie, mikroanalýzy horninotvorných minerálů, analýzy hlavních a stopových prvků, izotopů Sr-Nd-Pb a U-Pb geochronologie na zirkonech za účelem objasnění petrogeneze a vývoje DVC. Na základě těchto dat je zřejmá minimálně třístupňová metamorfóza zahrnující alteraci během extruze magmatu na mořské dno, variskou regionální metamorfózu a variskou kontaktní metamorfózu související s intruzí Středočeského plutonického komplexu. Zkoumané horniny vykazují vápenato-alkalický trend, zatímco bazalty vykazující tholeiitický trend, dříve popsané z této oblasti, jsou považovány za produkty mladších událostí. V severní části DVC dominují felsické subvulkanické (plagiogranit), vulkanické (dacit-ryolit) a pyroklastické (daciticko-ryolitické tufy a brekcie) členy s několika výchozy bazalto-andezitových až andezitových polštářových láv dokumentující mořské prostředí extruze. Tyto horniny mají vysoký podíl sodíku, a naopak nízký podíl draslíku, přičemž plagiogranit obsahuje albit, který se zdá že je primárního charakteru. Horniny vykazují vysoce radiogenní hodnoty ε_{Nd} (~ +6 až +11), jsou obohacené o prvky s vysokým iontovým poloměrem, a naopak ochuzené o prvky s velkým iontovým nábojem, což značí derivaci z primárně ochuzeného pláště, který byl ale následně metasomatizován subdukčními fluidy, což je charakteristické pro geotektonické prostředí spojené s vnitro-oceánskou subdukcí – s ostrovním obloukem. Výsledky geochemického modelování dokazují, že vznik plagiogranitů a ryolitů DVC nelze vysvětlit frakční krystalizací původního magmatu o složení výše zmíněných polštářových láv. Na druhou stranu, jejich vznik lze vysvětlit 20 % parciálním tavením metasomatizovaného plášťového peridotitu a následným vysokým stupněm frakční krystalizace mateřských tavenin. V jižní části DVC naopak dominují ortoruly s geochemicky podobnými vulkanickými a pyroklastickými horninami. Nové datování metodou U-Pb na zirkonech poskytlo stáří 608 ± 8 milionů let protolitu mafické ortoruly a stáří 637 ± 11 milionů let ryolitové žíly pronikající felsickou ortorulu, která ovšem pravděpodobně obsahuje velké množství zděděných zirkonů. Oproti horninám severní části DVC, mají ortoruly vyšší koncentrace K, Rb, Ba, Th, U a lehkých vzácných zemin, ale nižší obsahy Na_2O, což spolu s jejich zápornými hodnotami ε_{Nd} (–5,1 až –3,1) značí derivaci z geochemicky vyvinuté kontinentální kůry. Výsledky geochemického modelování ukazují, že tyto horniny mohly vzniknout frakční krystalizací andezitových láv/žil z DVC s vysokým stupněm asimilace kontinentální kůry. Tyto andezity se nachází v obou částech DVC (severní i jižní) a vykazují subdukční charakteristiku stopových prvků a hodnoty ε_{Nd} v rozmezí od –1,5 do +3,6, což značí komplexní vývoj jejich zdroje. Celá sekvence vulkanických hornin je pronikána boninitovými žilami s hodnotami ε_{Nd} +3,7 až +5,8, které pravděpodobně vznikly vysokým stupněm parciálního tavení ochuzeného pláště, což bylo zapříčiněno odlomením subdukující oceánské desky a s tím spojeným průnikem astenosférického plášťového materiálu do plášťového klínu. Na závěr práce je představen nový, předběžný, geotektonický model neoproterozoického až kambrického vývoje DVC. V něm jsou severní a jižní část DVC prezentovány jako oddělené segmenty kadomského orogenu, přičemž severní část reprezentuje ostrovní vulkanický oblouk, zatímco jižní část odpovídá kontinentálnímu vulkanickému oblouku.

Table of contents

1. Introduction 1
2. Magmatism at Earth`s plate tectonic boundaries 2
3. Island arc magmatism 3
   3.1. Island arc cross section 3
   3.2. Rock characteristics 4
   3.3. Mantle wedge processes 5
   3.4. Spatial and temporal evolution 9
   3.5. Silica-rich magmatism in island arcs 10
4. Geological setting 11
   4.1. Bohemian Massif and Teplá-Barrandian unit 11
   4.2. Davle Volcanic Complex 14
   4.3. Tectonic and metamorphic evolution 16
5. Methods 18
   5.1. Sampling and sample processing 18
   5.2. Major and minor element microanalysis of rock-forming minerals 20
   5.3. U–Pb zircon dating 20
   5.4. Whole-rock major and trace element analyses 21
   5.5. Sr–Nd–Pb isotopic analyses 22
   5.6. Geochemical modelling 23
6. Results 24
   6.1. Petrography and mineral compositions 24
      6.1.1. Pillow lavas 24
      6.1.2. Andesite dykes and lavas 25
      6.1.3. Dacitic and rhyolitic dykes and lavas 25
      6.1.4. Dacitic and rhyolitic tuff 26
      6.1.5. Plagiogranite 26
      6.1.6. Orthogneiss and related rhyolite 27
      6.1.7. Boninite 28
   6.2. U-Pb geochronology 33
   6.3. Whole-rock geochemistry 33
      6.3.1. Major element compositions 33
      6.3.2. Trace element geochemistry 37
   6.4. Sr–Nd–Pb isotope geochemistry 42
7. Discussion 45
   7.1. Metamorphism and its impact on the composition of the DVC 45
   7.2. Overview and new constrains on the temporal evolution of the DVC 48

7.3. Petrogenesis of the DVC magmatic suite 49
7.3.1. Basaltic-andesitic and andesitic pillow lavas 50
7.3.2. Andesite lavas and dykes 50
7.3.3. Dacitic lava and tuff 51
7.3.4. Plagiogranite and rhyolite 51
7.3.5. Orthogneiss and related rhyolite dyke 55
7.3.6. Boninite 55
7.4. Davle volcanic arc evolution and implications for the late Neoproterozoic–Cambrian evolution of Teplá-Barrandian unit 56
8. Conclusions 61
9. References 62
Appendix 71

List of figures

Figure 1. Simplified plate-tectonic scheme showing the major geotectonic settings of magmatism – volcanic island arc, hot spot plume-related seamount, mid-ocean ridge, volcanic continental arc, and rift zone. Modified after José F. Vigil and Robert I. Tilling, courtesy of U.S. Geological Survey..... 3

Figure 2. Typical island arc cross-section after Winter, 2010. 4

Figure 3. A schematic cut through the subducted slab showing the dehydration and melting process (after Zheng, 2019). 7

Figure 4. Radiogenic Sr, Nd, Pb isotope mantle source reservoirs (DMM, EM1, EM2 and HIMU, see text for details) inferred from ocean island basalts (OIB) and mid-ocean ridge basalts (MORB) (after Zheng, 2019). 9

Figure 5. (a) Overview map of the Cadomian relics incorporated in European Variscan belt, Hajná et al., 2014 and refs. therein. (b) Palinspastic reconstruction of the Avalonian–Cadomian belt on the northern active margin of Gondwana during the late Neoproterozoic; OM - Ossa Morena, AR – Armorican Massif, SX – Saxothuringian unit, TBU – Teplá–Barrandian unit, after Ackerman et al., 2019. (c) Simplified geological map of the Teplá–Barrandian unit, Hajná et al., 2014 and refs. therein. 13

Figure 6. Geologic map of the Davle Volcanic Complex (A), with a detail of the northern part of the Jílové belt (B) and a geologic profile (C-D). Redrafted from geological map of the Czech Republic 1:50,000 published by the Czech Geological Survey. The positions of the collected samples are shown by black stars. 15

Figure 7. Stratigraphic profiles of the DVC: north and south section of the Jílové belt (modified after Ackerman et al., 2021). U-Pb ages are from: (1) Hajná et al., 2018, (2) Dörr et al., 2002, (3) Ackerman et al., 2021 and this study. 16

Figure 8. Lithologic features of the DVC documented on images from the field (V. Santolík). A: Andesitic pillow lavas from the Zbraslav section. B, C: Plagiogranite intercalated by andesitic lava screens near Třebenice village, which developed most probably during Variscan deformation related to the emplacement of Central Bohemian Plutonic Complex. D: Outcrop of felsic orthogneiss near Simínský mlýn village, sample X8. E: Layers of alternating rhyolitic and dacitic tuff, volcanic breccia and graywacke in Zbraslav quarry, Zbraslav section. 19

Figure 9. Photomicrographs documenting petrography of andesite and basaltic andesite pillow lavas from DVC. A, B: plane polarized light, samples 17CB01/1 and 17CB23, respectively. C, D: back-scattered (BSE) images, samples 17CB01/1 and 17CB23, respectively; Plg-plagioclase, Amp-amphibole, Ab-albite, Chl-chlorite, Ttn-titanite, Qtz-quartz, Hbl-hornblende, Act-actinolite, And-andesine, Ep-epidote. 24

Figure 10. Photomicrographs illustrating petrography of andesite dykes and lavas. A, B: spherulitic texture in andesite from Zbraslav section, plane polarized light, sample V-1098. C: fine-grained andesite from Jílové belt, plane polarized light, sample V-487. D: fine-grained foliated andesite from Jílové belt, BSE image, sample V.470; Plg-plagioclase, Act-actinolite, Hbl-hornblende, And-andesine, Chl-chlorite, Ab-albite, Mag-magnetite. 25

Figure 11. Photomicrographs illustrating petrography of rhyolitic and dacitic lavas and tuffs. A: rhyolitic lava, plane polarized light, sample 17CB26. B: dacitic tuff, plane polarized light, sample 17CB07/26. C: albite phenocryst in rhyolitic lava, BSE image, sample 17CB26. D: dacitic tuff, BSE image, sample 17CB29/1; Plg-plagioclase, Ab-albite, Olg-oligoclase, Chl-chlorite, Qtz-quartz, Mag-magnetite, Bt-biotite, Ep-epidote. 26

Figure 12. Photomicrograph illustrating petrography of plagiogranites. A, B: sample V-490, polarizing microscope, parallel Nicols and crossed Nicols, respectively; Qtz-quartz, Mag-magnetite, Chl-chlorite, Ab-albite. 27

Figure 13. Photomicrograph illustrating petrography of orthogneiss. A: mafic orthogneiss, plane polarized light, sample V-102. B: felsic orthogneiss, plane polarized light, sample X6. C: mafic orthogneiss, BSE image, sample V-102. D: felsic orthogneiss, BSE image, sample X6; Qtz-quartz, Amp-amphibole, Plg-plagioclase, And-andesine, Hbl-hornblende, Mag-magnetite, Kfs-K-feldspar, Act-actinolite, Chl-chlorite, Ab-albite, Bt-biotite. 28

Figure 14. Photomicrograph illustrating petrography of boninites. A: foliated texture with clinopyroxene phenocryst, sample 17CB24, plane polarized light. B: weakly deformed and metamorphosed boninite, sample M-2, BSE image; Amp-amphibole, Px-pyroxene, Olg-oligoclase, Lab-labradorite, An-anorthite, Act-actinolite, Prg-pargasite, Di-diopside, Di-Hd - diopside-hedenbergite, Chr-chromite, Ep-epidote. 29

Figure 15. Classification diagrams for spinel from basaltic andesite, boninite, mafic orthogneiss and plagiogranite of the DVC, after Barnes and Roeder, 2001. All analyzed rocks contain spinels of nearly pure magnetite component, mafic orthogneiss contains a slightly Cr-enriched component in addition and boninite contains chromite grains in addition. 29

Figure 16. Ternary diagrams illustrating feldspar composition from different rock types of the DVC. Note that plagioclase prevails in most samples, only orthogneisses contain larger amounts of K-feldspars. 30

Figure 17. Binary diagram showing plagioclase composition of different rock types from the DVC. Albite prevails in most cases, oligoclase and andesine are also quite common but labradorite to anorthite composition is present only rarely in boninite and andesitic pillow lava. 31

Figure 18. Pyroxene classification diagram after Morimoto (1988), showing diopside-augite composition of the phenocryst grains and diopside-hedenbergite composition of the grains in matrix of boninites from the DVC. 31

Figure 19. Amphibole classification diagram after Leake et al. (1997), showing actinolite composition of the grain cores but hornblende-pargasite composition of the grain rims of different rock types from the DVC. 32

Figure 20. Concordia diagrams of samples V-107 (A) and X7 (B). 33

Figure 21. Whole-rock compositions of DVC rocks plotted in the Total Alkali – Silica (TAS) diagram after Le Bas et al. (1986). 34

Figure 22. Whole-rock major element compositions of the DVC rocks expressed in Harker‘s diagrams. 35

Figure 23. Samples of the DVC displayed in AFM Diagram; A = $Na_2O + K_2O$, M = MgO, F = FeO_t. 36

Figure 24. Samples of the DVC plutonic and subvolcanic rocks displayed in diagram for granitic rocks after Frost et al. (2001). 36

Figure 25. Samples of the DVC plutonic and subvolcanic rocks displayed in diagram for granitic rocks after O’Connor (1965). 37

Figure 26. Incompatible element spider diagrams for all samples normalized to primitive mantle (McDonough and Sun, 1995). 38

Figure 27. REE spider diagrams for all samples normalized to primitive mantle (McDonough and Sun, 1995). 39

Figure 28. Variations of REEs with SiO_2 contents for the DVC samples. 39

Figure 29. Variations of selected trace elements with SiO_2 contents of the DVC samples..... 40

Figure 30. Geotectonic discrimination diagrams Th/Yb vs. Nb/Yb (Pearce, 2014) and Zr vs Ti (Pearce, 1982) showing subduction affinity of the DVC rocks..... 41

Figure 31. Melt source discrimination diagrams after (Hawkesworth et al., 1997). Most of the DVC samples follow the Ba/Th and U/Th enrichment trend arguing for fluid enriched source but orthogneisses and dacitic tuff 17CB29/1 follow Th enrichment trend which stands for magma source enriched in sediment derived melt..... 41

Figure 32. Sr-Nd-Pb isotopic compositions of the studied samples from the DVC. (A) ε_{Nd} vs $^{87}Sr/^{86}Sr$ (i) diagram with different geochemical reservoirs and a decoupling trend displayed. (B) ε_{Nd} vs. Age diagram showing curves of two-stage model ages (Liew and Hofmann, 1988). (C), (D) $^{207}Pb/^{204}Pb$ (i) vs. $^{206}Pb/^{204}Pb$ (i) and $^{208}Pb/^{204}Pb$ (i) vs. $^{206}Pb/^{204}Pb$ (i) diagrams, respectively, showing a wide scatter in $^{206}Pb/^{204}Pb$ (i) ratios likely caused by later disruption of the isotopic system, NHRL was calculated using equations from Rollinson (1993), curves of Upper continental crust (UCC) and Depleted mantle (DM) isotopic evolution are from Zartman and Doe (1981) and curve of two-stage lead isotope evolution (SK) is from Stacey and Kramers (1975). 44

Figure 33. Zones of contact metamorphism in the northeastern part of the DVC, modified after Röhlich (1972)..... 47

Figure 34. Relationship between composition of plagioclase from DVC magmatic rocks and metamorphic overprint. 47

Figure 35. Relationship of amphibole composition and metamorphic evolution (regional vs. contact metamorphism) of the DVC. 48

Figure 36. Results of geochemical modeling using mean DVC pillow lava composition to possibly explain the composition of plagiogranite. (A) and (B): REE spider diagrams normalized to primitive mantle (McDonough and Sun, 1995) with different proportion of crystalizing minerals. The red field stands for the range of plagiogranite composition and F stands for the fraction of remaining magma in percent. Ol=olivine, Opx=orthopyroxene, Cpx=clinopyroxene, Amp=amphibole, Pl=plagioclase, Mag=magnetite..... 52

Figure 37. Results of geochemical modeling using average DMM (Workman and Hart, 2005) as source for partial melting in (A) and (B) and fractional crystallization of the melt produced by 20% partial melting of this source in (C) and (D). Presented spider diagrams are normalized to primitive mantle (McDonough and Sun, 1995), panels (A) and (C) show spider diagrams of REEs whereas panels (B) and (D) show other incompatible elements. The red field stands for the range of plagiogranite composition and F in (C) and (D) stands for the fraction of remaining magma in percent. Ol=olivine, Opx=orthopyroxene, Cpx=clinopyroxene, Spl=spinel, Amp=amphibole, Pl=plagioclase, Mag=magnetite..... 53

Figure 38. Results of geochemical modeling using average minimum values of andesite as primary magma for assimilation - fractional crystallization model. Presented spider diagrams, (A) for REEs and (B) for incompatible trace elements, are normalized to primitive mantle (W. F. McDonough and Sun, 1995). The pink field stands for the range of orthogneiss composition while F stands for the fraction of remaining magma (%). Opx=orthopyroxene, Cpx=clinopyroxene, Amp=amphibole, Pl=plagioclase, Mag=magnetite, Ap=apatite. 55

Figure 39. A sketch of the new geotectonic model proposed for the DVC evolution on the northern margin of Gondwana taking into account previous assumptions on the DVC evolution (Ackerman et al., 2021; Drost et al., 2011; Hajná et al., 2018, and refs. therein), not to scale. FC = fractional crystallization, AFC = assimilation–fractional crystallization, SCLM = subcontinental lithospheric mantle, OC = oceanic crust, SOLM = suboceanic lithospheric mantle..... 57

Figure 40. Geologic map of the DVC presenting the new geotectonic model, see text for details. 58

List of tables

Table 1. Relative proportions of volcanic rock types from different island-arcs, after Winter (2010). .. 5
Table 2. List of analyzed samples and methods used. 18
Table 3. Sr–Nd isotopic compositions of the studied samples from the DVC. 43
Table 4. Pb isotopic compositions of the studied samples from the DVC. 43

1. Introduction

The geotectonic setting of magmatic arcs represents one of the most fundamental principles in the development of modern Earth (Gill, 1981; Kelemen et al., 2003; Moyen and Martin, 2012; Winter, 2010). Magmatic arcs develop above subduction zones and are responsible for production of large amounts of magma from juvenile mantle sources representing a key environment for crustal growth (Frost et al., 2016; Gill, 1981; Haase et al., 2016; Hawkesworth et al., 2019, 2009; Moyen and Martin, 2012; Nguyen et al., 2019; Rollinson, 2009). Continental arcs are formed when an oceanic lithospheric plate is subducted beneath a continental plate, whereas island arcs are formed when an oceanic plate is subducted beneath another oceanic plate (Winter, 2010). The processes responsible for magma generation in a subduction environment are very complex and differ in respect to the oceanic or continental character of the upper plate (Gill, 1981; Kelemen et al., 2003; Winter, 2010; Zheng, 2019). A great advancement during the course of scientific research in understanding these processes (e.g. Moyen and Martin, 2012; Zheng, 2019 for review) enable to accurately reconstruct the past geotectonic environment of a certain area through petrography and geochemistry of the outcropped rocks.

During the Neoproterozoic, a supercontinent Gondwana (Pannotia) situated on the southern hemisphere dominated the continents presented on the Earth (Dalziel, 1997; Hawkesworth et al., 2019; Nance and Murphy, 2019; Nance et al., 2010). An outstanding belt of continental and island arcs, fore-arc and back-arc basins and associated accretionary wedges called the Avalonian–Cadomian orogen formed at its northern margin (Chantraine et al., 2001; Dalziel, 1997; Hajná et al., 2018; Linnemann et al., 2014; Nance et al., 2010) resembling the modern western pacific in many ways (Ackerman et al., 2019). Remnants of this orogen are nowadays dispersed from North America (e.g. Martens et al., 2010; Thompson and Crowley, 2020; White et al., 2021), through Europe and northern Africa (e.g. Balintoni and Balica, 2016; Chantraine et al., 2001; Errami et al., 2021; Fernández-Suárez et al., 2014; Hajná et al., 2018; Linnemann et al., 2014; Waldron et al., 2019) to southern Asia (e.g. Gürsu et al., 2015; Horton et al., 2008; Moghadam et al., 2017).

This diploma thesis focuses on the evolution of the Davle Volcanic Complex, a magmatic arc situated at the southeastern edge of the Teplá-Barrandian unit of the Bohemian Massif (Hajná et al., 2011; Waldhausrová, 1984) that formed during the Avalonian–Cadomian orogeny (Ackerman et al., 2021, 2019; Drost et al., 2011, 2007; Hajná et al., 2018, 2017, 2011; Sláma et al., 2008; Žák et al., 2020; Žák and Sláma, 2018). In order to decipher its petrogenesis and magmatic evolution, various methods including fieldwork, optical microscopy, rock-forming mineral microanalysis, major and trace element analysis, Sr–Nd–Pb isotopic systematics and U–Pb zircon geochronology were conducted. Geochemical modelling based on trace element patterns was applied to explain the generation of different magmatic rocks and a new preliminary geotectonic model is presented to explain the Neoproterozoic–Cambrian evolution of the magmatic arc.

2. Magmatism at Earth`s plate tectonic boundaries

Magmatism (or magmatic/igneous activity) is a process responsible for formation of igneous rocks. Igneous rocks can be either volcanic/effusive when the magma erupts on the Earth surface, or plutonic/intrusive when the magma solidifies below the Earth surface. The igneous rocks show a wide variety of mineralogical and geochemical characteristics that reflect the conditions and processes responsible for their formation. In this respect, geotectonic setting is a key factor that controls these conditions and processes (Winter, 2010).

There are three main geotectonic (plate-tectonic) settings on Earth – convergent/divergent plate boundaries and intraplate setting (Figure 1) (Winter, 2010). As the term suggests, the intraplate magmatism occurs within a single tectonic plate, either oceanic or continental. It is driven by upwelling mantle caused by mantle plume or continental rifting. The magmatic rocks are usually alkaline, basaltic in oceanic environment and bimodal (basaltic to rhyolitic) in continental environment and can be derived both from mantle or crustal sources (Ebinger and Sleep, 1998; Gao et al., 2008). Divergent plate boundaries occur at mid-ocean ridges where two tectonic plates are drawn apart forming a new oceanic crust. At such setting, magma is derived from depleted mantle and is characterized by tholeiitic trend and predominantly basaltic composition. By contrast, at convergent plate boundaries, magmatic products are extremely diverse since the nature of the magma source and crust involved is various (Winter, 2010). If two oceanic plates converge, one is subducted beneath the other (intra-oceanic subduction) and an island arc is formed on the Earth surface. Nowadays, basalts, basaltic andesites and andesites following a calc-alkaline trend are the predominant rocks in this setting (Gill, 1981) whereas during Archean, tonalite-trondhjemite-granodiorite (TTG) suite originate (Moyen and Martin, 2012). At oceanic crust– continental crust convergent margin (active continental margin), an oceanic lithospheric plate is subducted beneath a continental plate. Analogous to the intra-oceanic subduction, calc-alkaline trend is typical at active continental margin and the processes are very complex, nonetheless, the igneous rocks are generally more siliceous since continental crustal source is more involved in their formation (Gill, 1981; Tatsumi, 2005). At convergent boundary of two continental lithospheric plates, the buoyant continental crust is less likely to subduct deep into the mantle, which results in accumulation of great amounts of continental material and an orogenic belt is formed. Magmatism in this environment is usually siliceous, dominated by re-melting of continental crust, forming typical peraluminous granitic magmas (Didier et al., 1982; Frost et al., 2016).

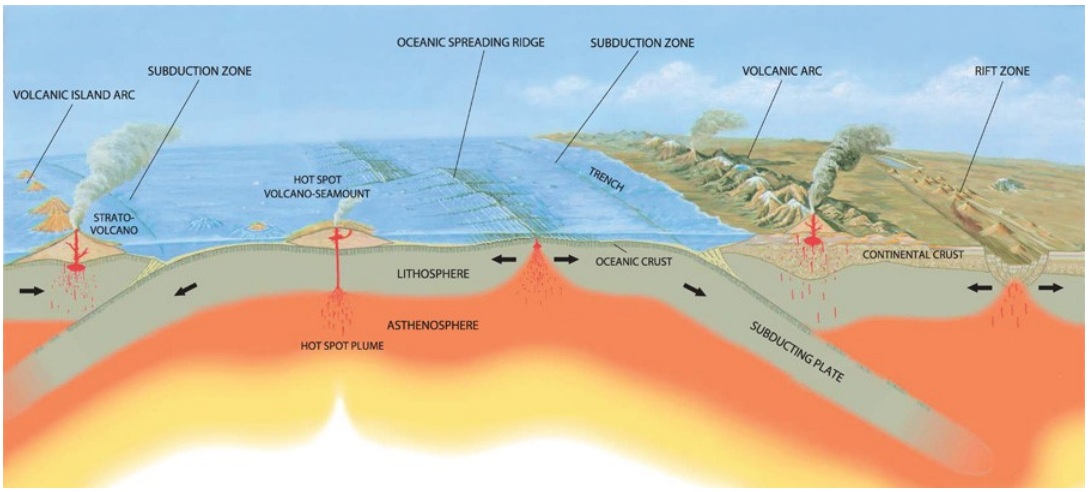

Figure 1. Simplified plate-tectonic scheme showing the major geotectonic settings of magmatism – volcanic island arc, hot spot plume-related seamount, mid-ocean ridge, volcanic continental arc, and rift zone. Modified after José F. Vigil and Robert I. Tilling, courtesy of U.S. Geological Survey.

3. Island arc magmatism

Island arcs occur on a convergent margin of two oceanic plates, where one oceanic plate is subducted beneath another one. Many examples of this tectonic setting can be found on today's plate tectonic map, for instance Aleutians, Japan, Izu-Bonin-Mariana, Lesser Antilles and other island chains. Large amounts of magma are generated in such setting with a calc-alkaline character and predominance of intermediate products such as basaltic andesite and andesite. However, the magma characteristics can be influenced by many circumstances like the composition of parental mantle wedge, age and angle of the subducting slab, composition of subduction-related fluids, the thickness of the arc crust, etc. Island arcs have been studied for decades (see e.g. Gill, 1981; Moyen and Martin, 2012; Pearce et al., 2005), nevertheless, new insights are still being revealed and discussed, which force the scientific community to reconsider the previously generally accepted principles of formation and evolution of island arc systems (Castillo, 2012; Zheng, 2019). In the following chapter, the most important facts about island arc magmatism will be reviewed.

3.1. Island arc cross section

A schematic cross section through a typical island arc is shown in Figure 2. It constitutes of:

1) A trench. Trench is the junction of two plates.
2) A fore-arc. Fore-arc is the area between trench and volcanic arc. It is composed of rocks derived from both plates – volcanic, pyroclastic and sedimentary rocks derived from an upper plate as well as subducting plate. The rocks are usually highly deformed and piled up. Fore-arc is sometimes also referred to as an accretionary prism or accretionary wedge.
3) A volcanic arc. Volcanic arc itself consists of volcanoes, typically stratovolcanoes that can be exposed either below or above sea level. It is mostly relatively narrow linear belt parallel to the trench line and can be thousands of km long. Its distance from the

trench is variable and largely depends on the subduction angle. In a recent flat subduction regime, the volcanic arc can be up to 300 km far from the trench, whereas in steep subduction regime, the volcanic arc is closer to the trench, ca. 150 km far.

4) A back-arc. Due to roll-back of the subducted slab, the volcanic arc is pulled towards the trench, which induces crust extension in the back-arc settings and formation of back-arc basin. This environment is characterized by extensional regime, mantle upwelling and associated melt production and sometimes also formation of new mid-ocean ridge system.
5) A mantle wedge. Mantle wedge constitutes a mantle part of the upper plate in subduction environment. The processes occurring therein are very complex and will be discussed in chapter **Chyba! Nenalezen zdroj odkazů.**.

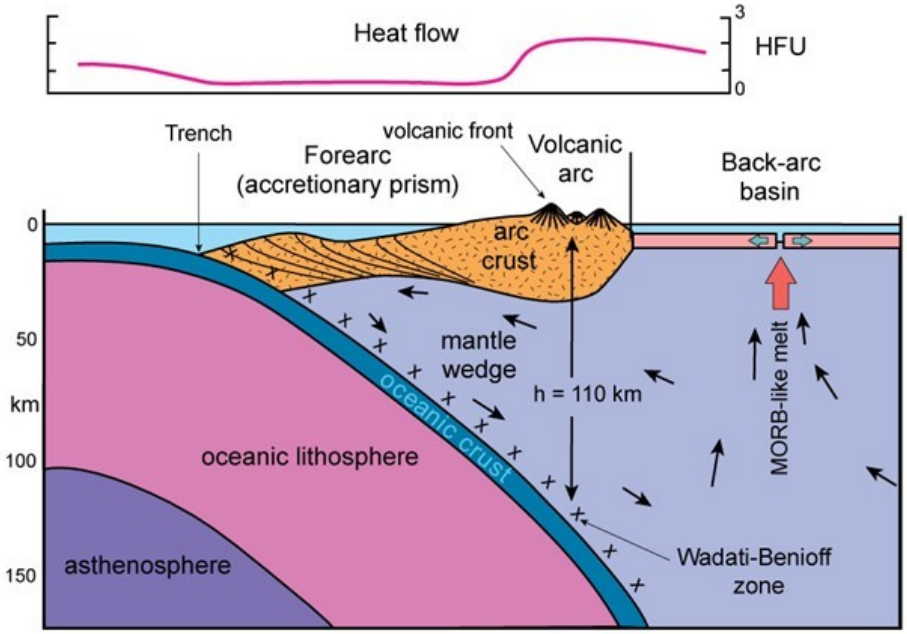

Figure 2. Typical island arc cross-section after Winter, 2010.

3.2. Rock characteristics

Island arcs are build up by volcanic and pyroclastic rocks of various composition. Gill, 1981, described population of different volcanic rock types in recent island arcs (Table 1) and stated that although the database is not complete, the observed rock lithology is representative for this environment. The number of chemical analyses of island arc volcanic rocks has grown significantly since then, many exceptions and unique rock types have been revealed, but the main trend still stands similar – the island arcs are dominated by basic to intermediate volcanic rocks (Zheng, 2019). The majority of them fall into the field of andesite and basaltic andesite, accompanied by a subordinate dacite and basalt, while rhyolite is rather rare type of rock. Island arcs can be also intruded by plutonic, subvolcanic or dyke rocks. These can vary in composition from gabbroic to granitic composition with various intrusion styles (Beard, 1986; Winter, 2010).

Relative Proportions of Analyzed Island-Arc Volcanic Rock Types (vol. %)					
Locality	**B**	**B-A**	**A**	**D**	**R**
Mt. Misery, Antilles (lavas)	17	22	49	12	0
Average Antilles	17	(42)		39	2
Lesser Antilles	71	22	5	(3)	
Nicaragua, NW Costa Rica	64	33	3	(0)	
W Panama, SE Costa Rica	34	49	16	(1)	
Aleutians east of Adak	55	36	9	0	0
Aleutians Adak and west	20	31	38	(10)	
Average Japan (lava, ash falls)	14	(85)		2	0
Izu-Bonin/Mariana	36	31	7	10	17
Kuriles	34	38	25	(3)	
Talasea, Papua	9	23	55	9	4
Scotia	65	33	2	(0)	

Table 1. Relative proportions of volcanic rock types from different island-arcs, after Winter (2010). B – basalt, B-A – basaltic andesite, A – andesite, D – dacite, R – rhyolite.

In terms of mineralogy, the individual rock types follow the characteristics described in Gill (1981). Basalts are dominated by olivine, clinopyroxene, plagioclase and magnetite. Basaltic andesite and andesite can contain orthopyroxene and amphibole in addition, and finally dacite and rhyolite are lacking olivine and clinopyroxene but contain quartz in addition. If the amount of K_2O is elevated, K-feldspar and biotite can be present, too (Gill, 1981; Wilson, 1989; Winter, 2010).

In terms of geochemistry, the island arc magmas are dominated by calc-alkaline trend. In comparison to MORB (mid-ocean ridge basalt) magmas, calc-alkaline magmas are depleted in FeO and CaO but enriched in Al_2O_3, Na_2O and K_2O (Chin et al., 2018; Gill, 1981; Winter, 2010). The trace elements display, on one hand, typically low abundances of compatible elements like Ni, Cr, V, and incompatible HFSE (high field strength elements) like Nb, Ta, Hf, Zr, on the other hand, typically elevated abundances of highly mobile elements like U, Pb and LILE (large-ion lithophile elements), for example Cs, Rb and Ba (Pearce et al., 2005; Tatsumi, 2005; Winter, 2010). The isotopic composition of the island arc magmas reflects the heterogeneity of processes and melt sources. They can either reflect enriched (low $^{144}Nd/^{143}Nd$, $^{176}Hf/^{177}Hf$ and high $^{87}Sr/^{88}Sr$) or depleted (high $^{144}Nd/^{143}Nd$, $^{176}Hf/^{177}Hf$ and low $^{87}Sr/^{88}Sr$) sources with a variable modification induced by evolution of parental magmas during emplacement such as assimilation-fractional crystallization (Arakawa et al., 1998; Klaver et al., 2020; Nguyen et al., 2019; Rudnev et al., 2020; Zheng, 2019).

3.3. Mantle wedge processes

The magma generation at subduction zones is driven by processes operating in the mantle wedge between subducted slab and oceanic arc. There are many methods of studying the mantle wedge composition and processes, including geochemical, thermodynamic and seismic tomography modeling (Bénard et al., 2017; Ma et al., 2019; Pearce et al., 2005; Syracuse et al., 2010; Vogt et al., 2012; Wada et al., 2012), high-pressure and high-

temperature experiments (Defant and Drummond, 1990; Grove et al., 2006; Rapp et al., 1999; Reynard, 2013), mantle xenoliths (Bénard et al., 2017; McInnes et al., 2001) and ophiolite studies (Alabaster et al., 1982; Chaib et al., 2021; Rollinson, 2009). The processes are very complex and underwent many reconsiderations throughout the course of research (Zheng, 2019). They include (1) slab metamorphic reactions, dehydration and melting, (2) transfer of slab-derived components to the mantle wedge and melting column, (3) mantle wedge melting and (4) reaction of mantle/slab-derived melts with arc crust (Bénard et al., 2017; Kelemen et al., 2003; Pearce and Peate, 1995; Spandler and Pirard, 2013; Zheng, 2019).

The first key process in island-arc magma generation occurs within the subducted oceanic slab (Figure 3). The slab, rich in water (either pore water or chemically bounded to sedimentary and volcanic rocks) and other volatiles, descends deep into the mantle, where it gets dehydrated and metamorphosed in the blueschist and, further in the mantle, eclogite facies. Traditionally, the melting of the subducted slab was rejected and the released aqueous fluids were considered to be the only (or most dominant) agent of transfer of the slab-derived components to the mantle wedge in modern arcs (Pearce and Peate, 1995; Tatsumi, 2005; Winter, 2010) comparing to Archean ones (Moyen and Martin, 2012). However, there is an increasing evidence that the main transfer agent are rather slab-derived hydrous melts (Hermann et al., 2006; Schiano et al., 1995; Spandler and Pirard, 2013; Zheng, 2019). This discrepancy is caused by the character of slab-derived fluids. At ultra-high pressures (>30 kbar), where the slab dehydrates, there is a continuous miscibility between aqueous fluid and hydrous melt, sometimes referred to as the super-critical fluid (Hermann et al., 2006; Zheng, 2019). The fluid component (H_2O) is derived predominantly from the mafic crust, whereas the solute (mineral) component is derived mainly from the subducted sediments (Hermann et al., 2006). Some authors distinguish between different subduction sources and transfer agents for different elements, namely, Th, P and light rare earth elements (LREE) are derived from subducted sediment at deeper subduction levels and transferred via hydrous melt ("deep subduction component"), whereas Rb, Ba, U, K, Pb and Sr are derived at shallower subduction levels ("shallow subduction component") and transferred via aqueous fluid (Elliott et al., 1997; Pearce et al., 2005).

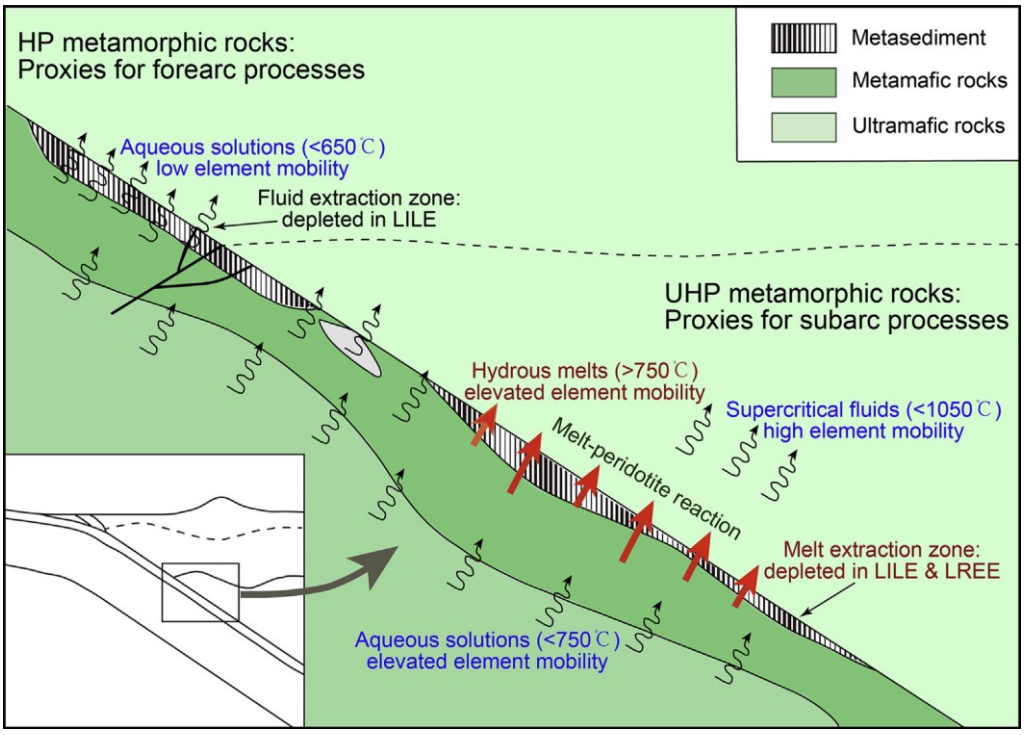

Figure 3. A schematic cut through the subducted slab showing the dehydration and melting process (after Zheng, 2019).

The enrichment and depletion of certain elements in slab-derived melts is controlled by their partition among metamorphic minerals and stability of these minerals (Hermann et al., 2006; Zheng, 2019). For instance, garnet incorporates heavy rare earth elements (HREE) in its structure, and since it is stable in the sub-arc high pressure-temperature (P–T) environment, the slab-derived melt such as adakite is HREE-depleted (Defant and Drummond, 1990; Moyen, 2009). Similarly, eclogitic rutile is responsible for high field strength elements (HFSE) depletion (Foley et al., 2000).

The fluids and melts derived from subducted oceanic lithosphere ascend into the overlying mantle wedge and cause metasomatism and partial melting of the mantle peridotite due to volatile influx (Grove et al., 2006; Sisson and Grove, 1993; Winter, 2010). The studies of orogenic peridotites and mantle wedge xenoliths provide important insights into the nature of sub-arc mantle (Bodinier and Godard, 2003; McInnes et al., 2001; Tollan et al., 2017; Zhao et al., 2019; Zheng, 2019). These investigations corroborate that the sub-arc mantle is very heterogeneous. On one hand, it is enriched in LILE, LREE, Th, U and Pb and depleted in HFSE and HREE due to metasomatism by subduction-derived melts/fluids (Pearce and Peate, 1995; Tollan et al., 2017; Zheng, 2019). On the other hand, it comprises usually refractory mantle consisting mainly of harzburgite, dunite and pyroxenite that can originate both from reaction between silica and water-rich melt with lherzolite or by high degrees of melt extraction (Bénard et al., 2017; Kelemen et al., 1992; Piccardo et al., 2007). Both of these processes occur in mantle wedge setting. Moreover, in most island arcs containing mantle xenoliths, several different types of peridotites have been found, indicating common existence of a heterogeneous mantle in a single arc (Tollan et al., 2017; Zheng, 2019).

The subsequent magmatic processes are very complicated and can result in melts of very diverse composition. Primitive magmas derived from the mantle wedge have the composition of high-Mg andesite (HMA) or boninite (Bénard et al., 2017; Castillo, 2012). In these H_2O-rich magmas, Fe–Ti oxides are likely to crystallize soon and remain in the deep lithosphere

causing the calc-alkaline trend of the resulting melt (Chin et al., 2018; Tatsumi, 2005). However, the calc-alkaline trend can be also attributed to subsequent processes of interaction between the mantle-derived magmas, mantle lithosphere and crust, which include assimilation, magma mixing, and fractional crystallization (Kelemen et al., 2003; Tatsumi, 2005). During these processes, the magma composition can change from basaltic, picritic or boninitic to andesitic, dacitic or rhyolitic, which causes the wide variety of volcanic and plutonic products at island arcs (Bénard et al., 2017; Frost et al., 2016; Gill, 1981; Kelemen et al., 2003; Meng et al., 2018; Nguyen et al., 2019).

An important process, wildly and hotly debated in the scientific community, is the melting of mafic, either oceanic or continental crust. There are many possibilities regarding the source of mafic crust, such as subducted oceanic crust, underplating basaltic magmas, or delaminated mafic lower crust (Atherton and Petford, 1993; Castillo, 2012; Defant and Drummond, 1990; Frost et al., 2016; Koepke et al., 2007; Moyen, 2009; Rudnev et al., 2020). It is believed that the mafic oceanic slab can melt only when it is anomalously hot (Defant and Drummond, 1990). This was probably quite common in the Archean era, giving rise to the characteristic and widespread TTG (tonalite-trondhjemite-granodiorite) suite (Moyen and Martin, 2012). In Phanerozoic arcs, however, temperatures elevated enough to cause the melting of subducted slab can be reached only when the convergence rate is low and the subducting plate is young (Defant and Drummond, 1990). These magmas are referred to as adakites and resemble in characteristic signature like high Na_2O content and high Sr/Y and La/Yb ratios, similar to Archean TTGs (Castillo, 2012; Kay, 1978; Martin, 1986; Martin et al., 2005; Moyen, 2009; Moyen and Martin, 2012). However, it is rather unlikely for these magmas to reach the Earth surface retaining their adakite signature, since it would require very large magma portions in order not to be homogenized with the mantle peridotite (Rapp et al., 1999). Moreover, melting of delaminated mafic lower crust or simply lower crustal amphibolites, can result in similar major and trace element characteristics (if garnet is present in the melting residue; e.g. Castillo, 2012; Defant and Drummond, 1990; Qian and Hermann, 2013). Therefore, such processes are recently preferred in explaining the adakite signature in most cases (Atherton and Petford, 1993; Bao et al., 2007; Castillo, 2012; Qian and Hermann, 2013; Rudnev et al., 2020).

In terms of radiogenic isotopes, island arc magmas are very heterogeneous. This results from the variety of processes and mantle/crustal reservoirs involved in the magma generation (Abati et al., 2018; Arakawa et al., 1998; Liu et al., 2018; Rudnev et al., 2020; Samson et al., 2004). Several mantle source reservoirs have been proposed to explain the isotopic variety of ocean island basalts (OIB) and mid-ocean ridge basalts (MORB), most importantly DMM (depleted MORB mantle), EM1 and EM2 (enriched mantle 1 and 2) and HIMU (high μ, $\mu = {}^{238}U/{}^{204}Pb$). The DMM is a typical depleted reservoir characterized by high $^{143}Nd/^{144}Nd$, $^{176}Hf/^{177}Hf$ and low $^{87}Sr/^{86}Sr$ and $^{206}Pb/^{204}Pb$ ratios. The enriched reservoirs (EM1, EM2 and HIMU) are variously enriched in different isotopic ratios (see Figure 4) and their origin is still quite controversial (Hofmann, 1997; Tatsumi, 2005; Zheng, 2019). Lower crust, corresponding to older crust, is characterized by very low $^{143}Nd/^{144}Nd$ and $^{176}Hf/^{177}Hf$ ratios and moderate $^{87}Sr/^{86}Sr$ and $^{206}Pb/^{204}Pb$ values, whereas for upper crust, corresponding to younger crust, moderate $^{143}Nd/^{144}Nd$ and $^{176}Hf/^{177}Hf$ values and high $^{87}Sr/^{86}Sr$ and $^{206}Pb/^{204}Pb$ values are characteristic (Rollinson, 1993; Winter, 2010). Most island arc volcanic rocks are probably derived from the DMM reservoir or follow the so-called mantle array (Gill, 1981), however, there are plenty enriched source characteristics that suffer from the various processes described above (Arakawa, 1998; Gill, 1981; Liu et al., 2018; Samson et al., 2004).

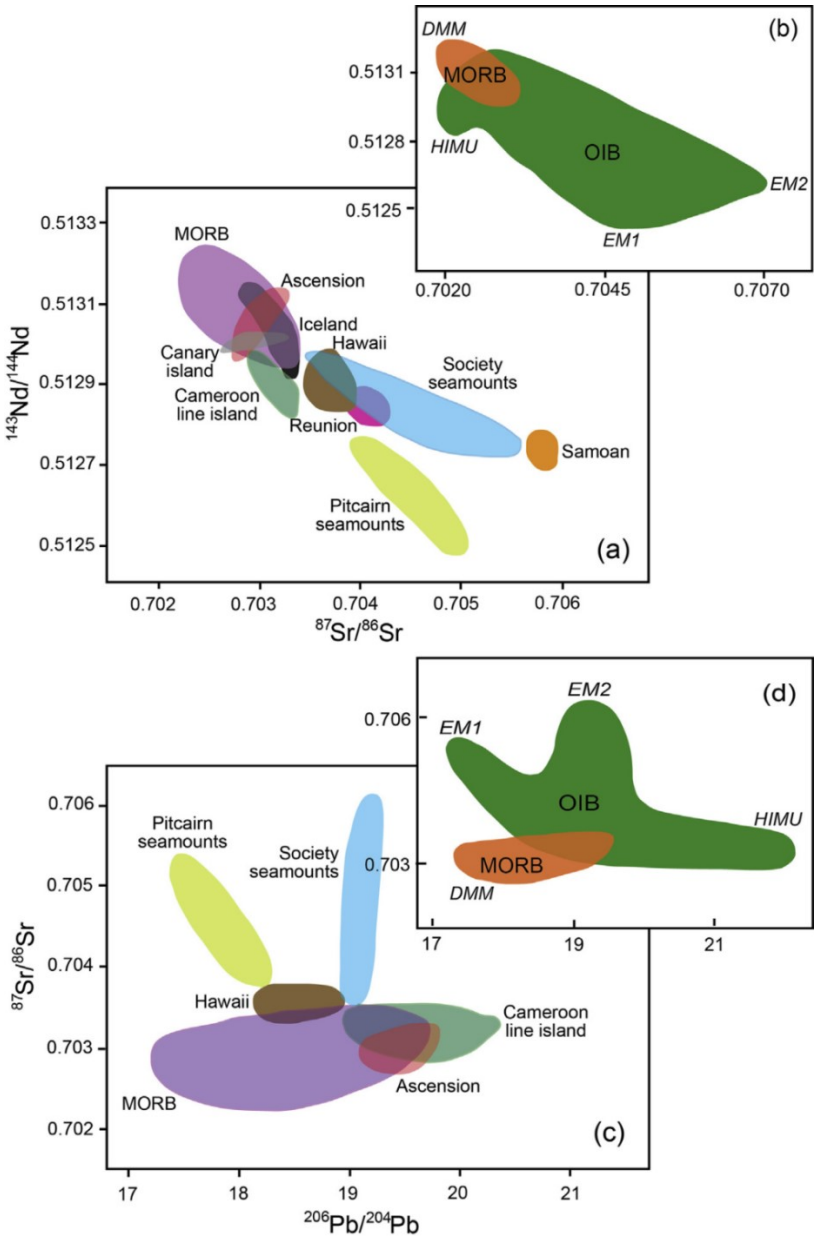

Figure 4. Radiogenic Sr, Nd, Pb isotope mantle source reservoirs (DMM, EM1, EM2 and HIMU, see text for details) inferred from ocean island basalts (OIB) and mid-ocean ridge basalts (MORB) (after Zheng, 2019).

3.4. Spatial and temporal evolution

There are some general rules observed in recent island arcs considering their spatial and temporal evolution. Initiation of subduction and an island arc formation is characterized by production of tholeiitic magmas (Chin et al., 2018; Winter, 2010). This is because tholeiitic magmas are formed by decompression melting at lower pressures and with no addition of volatile component. Since arc crust is not thick enough and mantle wedge is not so metasomatized to trigger early crystallization of Fe–Ti oxides, magmas that erupt on the surface, follow tholeiitic trend (Chin et al., 2018; Dilek and Thy, 2009; Gill, 1981). When the arc grows older, however, crust gets thicker and mantle wedge more metasomatized, and the generated magmas follow calc-alkaline trend (Chin et al., 2018; Gill, 1981). In old, mature or

collapsing arcs, even alkaline trend with high K_2O contents has been observed (Eyüboğlu, 2010; Gill, 1981; Zhang et al., 2011). Similar variability of magmatic products is observed in a cross section through a volcanic arc, where tholeiitic magmas occur mainly closer to the trench, where, due to slab roll-back, the crust is thinner and mantle wedge less metasomatized (Dilek and Thy, 2009; Gill, 1981). In contrast, calc-alkaline to shoshonitic (high K_2O) magmas occur farther from the trench. This variability includes also trace elements characteristic for each magma differentiation trend. However, these variations reflect just differentiation trends, there have not been reported many cases of variations in SiO_2 contents linked to spatial and temporal evolution (Gill, 1981; Winter, 2010; Zheng, 2019).

3.5. Silica-rich magmatism in island arcs

Since silica-rich magmatic rocks form a large part of the Davle Volcanic Complex targeted in this study (rhyolite, dacite, plagiogranite and orthogneiss; see the following chapters), the generation of silica-rich magmas in island arc setting is of particular interest. As proposed by Gill (1981) and other studies given above, the island arcs compositions are dominated by basaltic and andesitic rocks, while acidic magmas are relatively rare. Nevertheless, the database of volcanic arc rock analyses has grown since the 1980's and in almost every present-day island arc, there has been some amount of silica-rich volcanic rocks recognized (Leat et al., 2003; Price et al., 2005; Shukuno et al., 2006). Moreover, a significant effort in understanding the generation of silica-rich magmas in island arc setting has been made (Brophy, 2008; Frost et al., 2016; Koepke et al., 2007; Pu et al., 2014). Two major petrogenetic processes have been proposed for these peculiar rocks: (1) extensive fractional crystallization of mantle-derived hydrous basaltic melt, and (2) dehydration melting of lower crustal amphibolite (Brophy, 2008; Frost et al., 2016; Pu et al., 2014). Distinguishing between these two processes can be very difficult, since both resemble similar major/trace element and isotopic signatures.

Fractional crystallization of mantle-derived melt is characterized by (1) production of large plutonic intrusions (Nguyen et al., 2019) to small felsic veins (Chaib et al., 2021; Chen et al., 2019), (2) highly positive ε_{Nd} and ε_{Hf} values typical for depleted mantle (e.g. Haase et al., 2016), (3) higher TiO_2 contents (Koepke et al., 2007), (4) progressively increasing concentrations of incompatible elements such as K, Na, Zr, Y and REE with increasing SiO_2 content (Brophy, 2008; DePaolo, 1981).

By contrast, dehydration melting of amphibolite can be ascribed to: (1) production of either large plutonic intrusions (Atherton and Petford, 1993; Rudnev et al., 2020), migmatites or veins and dykes (Sawyer, Edward, 2008), (2) highly positive to highly negative ε_{Nd} and ε_{Hf} values depending on their source nature (Liu et al., 2018; Rudnev et al., 2020), (3) lower TiO_2 content (Koepke et al., 2007), (4) constant LREE concentration with increasing SiO_2 and slightly decreasing HREE concentration with increasing SiO_2 content (Brophy, 2008; Pu et al., 2014).

However, all these aspects, notably TiO_2 and REE distinguishing approach, must be used with special caution, because they are strongly dependent on pressure, temperature, H_2O contents and maybe more unknowns that are still to be deciphered.

4. Geological setting

4.1. Bohemian Massif and Teplá-Barrandian unit

The Bohemian Massif is one of the largest exposed parts of the Variscan orogenic belt (Figure 5) (Matte, 1991). It occupies large area of Central Europe to north of the Alps and south from the North European Plain. It consists of several crustal blocks amalgamated during the Variscan orogeny at ~380–340 Ma, however, their exact relationships are still a matter of debate (Collett et al., 2021; Faryad and Kachlík, 2013; Jedlicka and Faryad, 2017; Kroner and Romer, 2013; Maierová et al., 2021; Matte, 1991; Schulmann et al., 2009; Žák and Sláma, 2018). The Teplá-Barrandian unit was positioned in an upper-plate position during the Variscan orogeny, which is documented by its boundary faults dipping beneath it and much weaker metamorphic overprint than in the neighboring units: Saxothuringian unit in the north and Moldanubian unit in the south (Hajná et al., 2011; Matte, 1991; Žák et al., 2005a). Many of the igneous rocks and sedimentary successions in all Variscan units were formed during Neoproterozoic and Lower Paleozoic (Dörr et al., 2002; Hajná et al., 2011; Košler et al., 2014; Linnemann et al., 2014; Mazur et al., 2015; Žák and Sláma, 2018). Additionally, there are some meta-igneous rocks in the Moldanubian unit dated at ~2.1 and 1.4 Ga (Friedl et al., 2004; Wendt et al., 1993), however, the Neoproterozoic rocks formed during the Cadomian orogeny are documented in all major units of the Bohemian massif and represent the oldest larger crustal segments preserved (Dörr et al., 2002; Friedl et al., 2004; Hajná et al., 2018, 2017; Kröner et al., 1994; Mazur et al., 2003; Teipel et al., 2004).

The Teplá-Barrandian unit (TBU) represents probably the best preserved and outcropped cross-section through a Cadomian accretionary wedge (Hajná et al., 2011). It is composed of four essential parts which from NW to SE are: (1) Mariánské lázně ophiolite complex composed of amphibolite, metagabbro, eclogite and serpentinized spinel peridotite representing a remnant of subducting oceanic plate, (2) Blovice Accretionary Complex that represents an accretionary wedge composed of graywacke, shale, siltstone, volcanic rocks and minor other rock types such as black shale, chert and carbonate, (3) Davle Volcanic Complex (DVC) consisting of volcanic/subvolcanic and volcanosedimentary rocks that stands as a relic of an island arc and (4) overlying Štěchovice Group and Svrchnice Formation representing post-volcanic intra-arc and back-arc sedimentary basins respectively (Hajná et al., 2019, 2011, and references therein).

The Cadomian accretionary orogeny formed during the late Neoproterozoic to early Cambrian era at the northern margin of supercontinent Gondwana. It is characterized by a formation of large belt that comprises several volcanic arcs, accretionary wedges, fore-, intra- and back-arc basins in the length of up to 10,000 km (Nance et al., 1991). Nowadays, relicts of this orogeny can be found in Europe (e.g. Bohemian, Armorican and Iberian massifs) and in North America (e.g. Nova Scotia, Florida, Yucatan) (Franke, 1989; Nance et al., 1991; Nance and Linnemann, 2008).

The onset of subduction in the TBU remains enigmatic, however, there is an increasing evidence on the latest stages of sedimentation and magmatic activity and the termination of orogenic activity (Ackerman et al., 2021, 2019; Cháb and Pelc, 1968; Drost et al., 2007; Hajná et al., 2018; Kříbek et al., 2000; Sláma et al., 2008; Waldhausrová, 1984; Žák et al., 2020). Interestingly, the main sedimentation and magmatic activity do not precisely correlate with each other. While the magmatic activity is bracketed between ~608 and 563 Ma, the

sedimentation and accretion continued to ~527 Ma (Hajná et al., 2018). Therefore, while the volcanic activity in the DVC already ceased, the sedimentary and accretionary processes in the Blovice accretionary prism continued and developed to presently aligned volcano-sedimentary belts (Hajná et al., 2018; Pin and Waldhausrová, 2007; Žák et al., 2020). Hajná et al. (2018) explained this controversy as change of dip of subduction or slab roll-back and trench migration. The end of the Cadomian cycle in the TBU is documented by initiation of rifting and formation of Cambrian continental basins at ca. 513 Ma (Hajná et al., 2018) that unconformably overlie the Cadomian basement.

As mentioned above, apart from the volcanic suite of the island arc (DVC), there is cross-section through all sedimentary successions preserved in the TBU (Figure 5). The Blovice Accretionary Complex consists of belts composed of typical turbidite sequences of graywacke, shale, siltstone and chert (Belt I–III), and belts composed of chaotic mélange of sediments with MORB and OIB-like basalts (Belt 1–3) accompanied by cherts, black shales and rarely carbonates (Cháb and Pelc, 1968; Hajná et al., 2019, 2011; Pin and Waldhausrová, 2007). In this section, the Štěchovice Group and Svrchnice Formation are thick sequences of siltstone, shale and graywacke successions developed from turbidite flows upon the eroded and submerged island arc after the termination of volcanic activity (Drost, 2008; Hajná et al., 2011; Kříbek et al., 2000; Sláma et al., 2008).

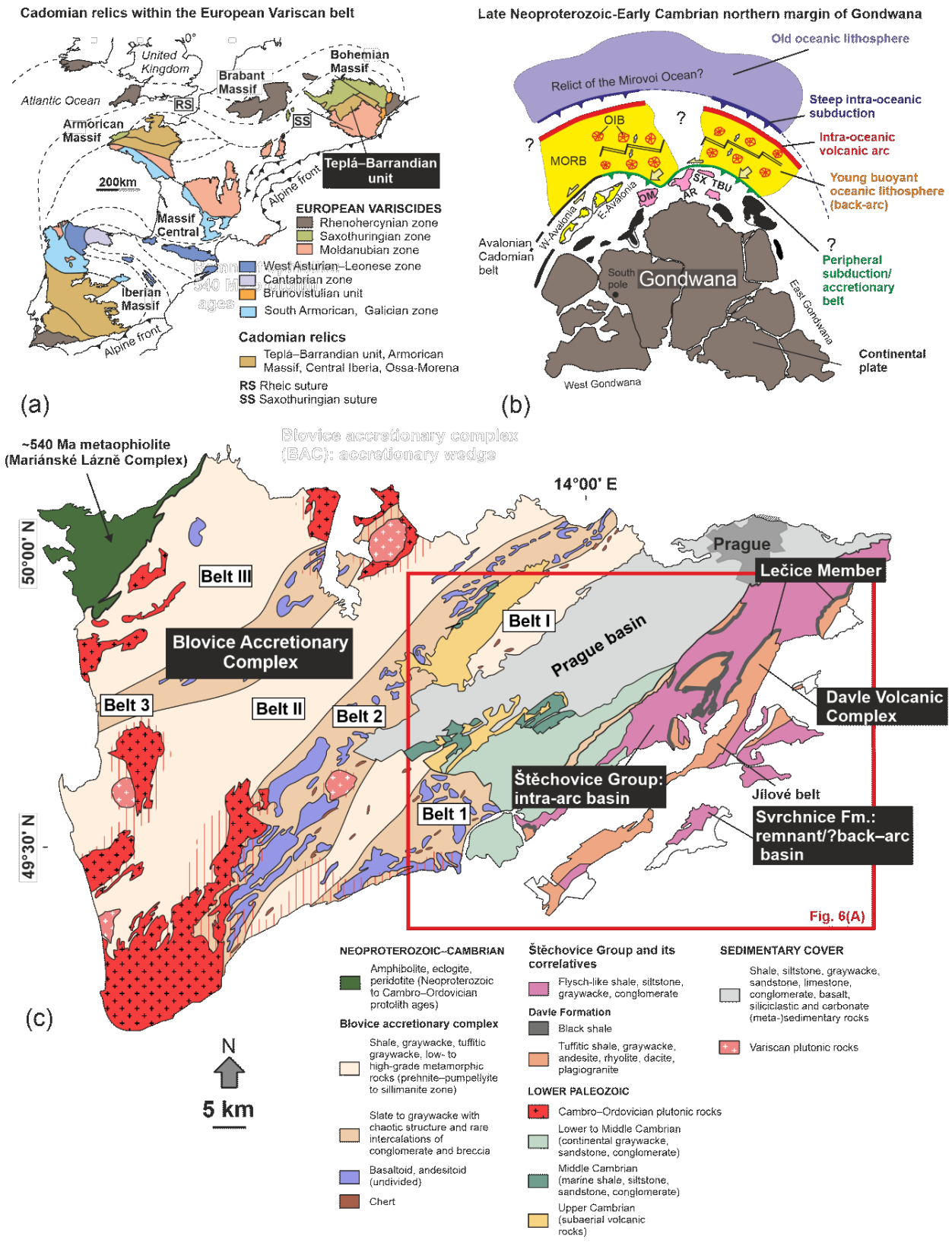

Figure 5. (a) Overview map of the Cadomian relics incorporated in European Variscan belt, Hajná et al., 2014 and refs. therein. (b) Palinspastic reconstruction of the Avalonian–Cadomian belt on the northern active margin of Gondwana during the late Neoproterozoic; OM - Ossa Morena, AR – Armorican Massif, SX – Saxothuringian unit, TBU – Teplá–Barrandian unit, after Ackerman et al., 2019. (c) Simplified geological map of the Teplá–Barrandian unit, Hajná et al., 2014 and refs. therein.

4.2. Davle Volcanic Complex

Davle Volcanic Complex (DVC) crops out in several anticline structures located to south of Prague. These include Jílové belt, partly Pičín belt, and small segments in field size (up to few kilometers in size) like Zbraslav, Bojov and Kozí Hory segments (see Figure 6). The Jílové belt represents a major part of the DVC exposing itself in a ~65 km long and up to ~3 km wide belt spreading from Mirovice in the SW to Jílové u Prahy in the NE (Hajná et al., 2011; Morávek and Röhlich, 1971; Waldhausrová, 1984). The Pičín belt is generally assumed to be a part of the Blovice Accretionary Complex, however, it contains also volcanic rocks such as rhyolite and plagiogranite belonging to the DVC (Hajná et al., 2011; Mráček, 2015). Altogether, the DVC consists of more than 1500 m thick volcanic sequence of basaltic andesite to rhyolite accompanied by subaqueous felsic pyroclastics represented by banded and massive ash-flows and ash-falls with horizons of coarse-grained lithic pyroclastic and epiclastic breccias and re-deposited tuffs (Hajná 2011). The sequence is intruded by subvolcanic plagiogranite in the northern Jílové belt and accompanied by orthogneiss in the southern Jílové belt. The end of volcanic activity is documented by sedimentation of 50–200 m thick layer of deep marine (black)shales called Lečice Member (Ackerman et al., 2021) and intrusion of boninite dykes (Fediuk, 1992; Kachlík et al., 1999).

Geochronological data from the TBU provide evidence of late Neoproterozoic (Ediacaran) age of the DVC (e.g. Hajná et al., 2018). The data from sedimentary rocks of the Blovice Accretionary Complex and Štěchovice Group indicate peak volcanic activity at ~650–580 Ma, ceasing at ~550 Ma (Drost et al., 2011; Hajná et al., 2019, 2018, 2017; Žák et al., 2020). Samples of rhyolite and rhyolitic tuff pebble from a conglomerate in the Štěchovice Group provided ages of 585 ± 7 and 568 ± 3 Ma, respectively (Dörr et al., 2002). Trondhjemite pebble from the Svrchnice Formation gave age of 610 ± 17 Ma (Sláma et al., 2008). A rhyolitic tuff from the uppermost part of the DVC provided Neoproterozoic ages ranging from 580 to 650 Ma with main cluster at around 607 Ma and interpreted sedimentation age at 583 +9/–15 Ma. This tuffitic layer is directly overlain by the black shales of the Lečice Member and the age of 583 +9/–15 Ma is therefore interpreted as the end of volcanic activity in the DVC (Ackerman et al., 2021).

During the emplacement of Variscan Central Bohemian Plutonic Complex at ~380–340 Ma (Holub et al., 1997; Tomek et al., 2015; Žák et al., 2005a), the DVC and surrounding Cadomian sediments were penetrated by lamprophyre dykes and ore veins with Au–Ag–Pb–Zn–U mineralizations (Hrouda et al., 2019; Morávek and Röhlich, 1971; Škácha et al., 2009; Zachariáš et al., 2014, 2013).

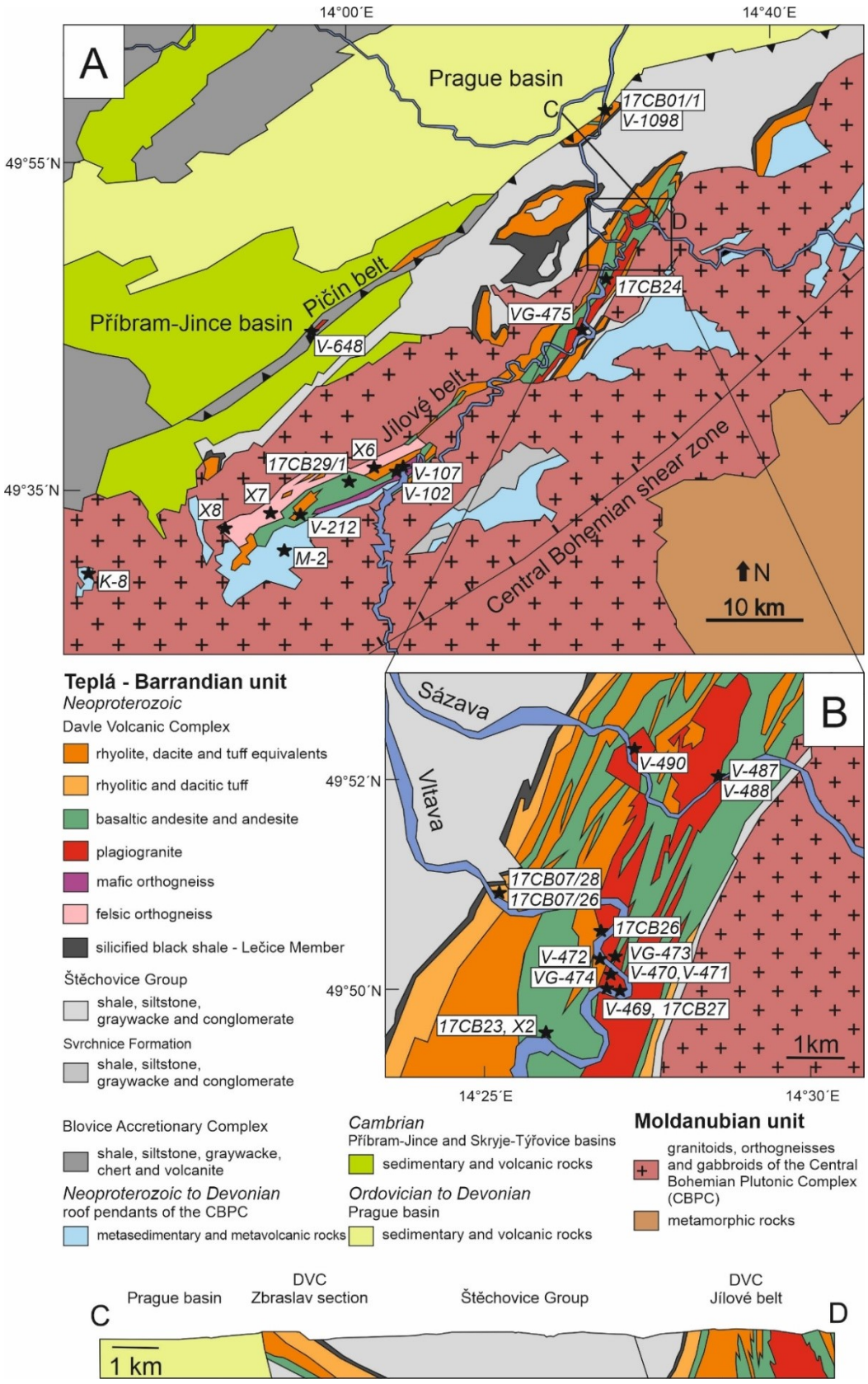

Figure 6. Geologic map of the Davle Volcanic Complex (A), with a detail of the northern part of the Jílové belt (B) and a geologic profile (C-D). Redrafted from geological map of the Czech Republic 1:50,000 published by the Czech Geological Survey. The positions of the collected samples are shown by black stars.

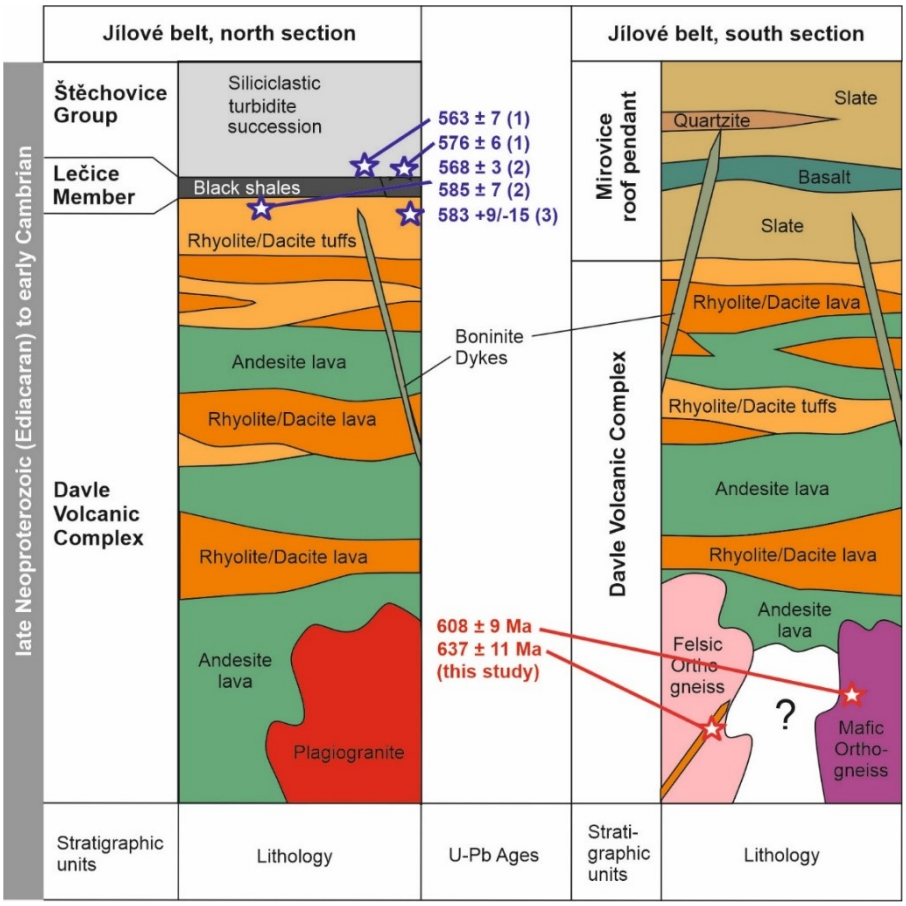

Figure 7. Stratigraphic profiles of the DVC: north and south section of the Jílové belt (modified after Ackerman et al., 2021). U-Pb ages are from: (1) Hajná et al., 2018, (2) Dörr et al., 2002, (3) Ackerman et al., 2021 and this study.

4.3. Tectonic and metamorphic evolution

During the Variscan orogeny, the TBU underwent a considerable deformation and metamorphism. Previously, it was assumed that, in the DVC, crucial tectonic overprint was driven by Cadomian orogenic processes, however, more detailed studies proved that more important overprint occurred during the Variscan orogeny (Rajlich et al., 1988; Žák et al., 2005b). The SE part the TBU (DVC and overlying Štěchovice Group) were folded into large-scale folds, where the DVC is exposed in anticline and the Štěchovice Group in syncline structures. In the Jílové belt, which is closer to the Central Bohemian Shear Zone in the SE, even a steep cleavage in NNE-SSW direction was developed (so called "Jílové cleavage"). Lineation is well developed on the cleavage domains and is sub-horizontally inclined mostly to the NNE to NE. The cleavage is more apparent in more brittle rocks (andesite) and closer to the Central Bohemian Shear Zone. Also, many parallel as well as perpendicular faults developed especially in the Jílové belt segment during the operation of Variscan deformation, due to which the primary structures of the volcanic sequence are strongly hindered. On the SW edge of the TBU, regional strain and metamorphism was accompanied by intrusion of Central Bohemian Plutonic Complex, which heated the surrounding rocks creating a thermal aureole (Morávek and Röhlich, 1971; Rajlich et al., 1988; Žák et al., 2005b).

Similarly to tectonic evolution, the main event in metamorphic evolution took place during the Variscan orogeny, however, three-stage metamorphic evolution should be considered (Röhlich, 1972). Since most of the volcanism was subaqueous (Fiala, 1987), the first metamorphic stage took place during the contact of lava with seawater. These changes may include chloritization and epidotization of amphibole and pyroxene and albitization of plagioclase. Röhlich (1972) and many following authors stressed the importance of Cadomian regional metamorphism, however, newer studies proved that, although it is quite difficult to distinguish between the three metamorphic events, the most important overprint of rock structure and composition happened during the Variscan orogeny (Rajlich et al., 1988; Žák et al., 2005b). Despite lying in the innermost part of the Variscan orogenic belt, the SE part of the TBU was affected by only weak regional metamorphism but close to the Central Bohemian Shear Zone, where the Jílové belt lies, regional metamorphism becomes more accentuated. This leads to recrystallization in the greenschist facies with new minerals like albite, muscovite, chlorite and quartz. Finally, due to emplacement of the Central Bohemian Plutonic Complex which intruded into the Central Bohemian Shear Zone, the DVC was affected by HT–LP metamorphism. Both regional and contact metamorphic grade is lowest in the NW and rises towards the plutonic complex in the SE (Fediukova and Fediuk, 2000; Röhlich, 1972; Waldhausrová, 1984).

5. Methods

5.1. Sampling and sample processing

Samples with locations and methods applied are summarized in Table 2 and Figure 6. They were collected from well-exposed outcrops during several field campaigns lead either by Václav Kachlík, Lukáš Ackerman or myself. In addition, all these localities were further visited and examined by myself in order to document rock relationships and overall geology of the DVC. From all sampled rocks, thin sections were prepared, and petrography of the rocks was examined in detail using microscope Olympus BX51 equipped with camera DP50 housed at the Institute of Geology of the Czech Academy of Sciences (IG CAS).

Table 2. List of analyzed samples and methods applied

Sample	Locality	Rock Type	Habitus	Coordinates (WGS 84)		Methods			
				Latitude N	Longitude E	Sr-Nd-Pb isotopes	U-Pb isotopic zircon age	Microanalysis	
								silicates	oxides
17CB23	Slapy	basaltic andesite	pillow lava	49.8258	14.4327	x		x	x
17CB01/1	Zbraslav	andesite	pillow lava	49.9657	14.3990	x		x	
V-470	Třebenice	andesite	lava	49.8364	14.4487	x		x	
VG-473	Třebenice	andesite	lava	49.8379	14.4482	x			
V-487	Žampach	andesite	lava	49.8688	14.4802	x			
V-1098	Zbraslav	andesite	lava	49.9657	14.3990	x	N/A*		
V-212	Nestrašovice	andesite	lava	49.5537	14.0380	x			
17CB27	Stěchovice	dacite	lava	49.8326	14.4512	x		x	
17CB07/26	Stěchovice	dacitic tuff	tuff	49.8502	14.4183				
17CB29/1	Pteč	dacitic tuff	tuff	49.5861	14.1050	x		x	
17CB07/28	Stěchovice	rhyolitic tuff	tuff	49.8502	14.4183				
17CB26	Stěchovice	rhyolite	lava	49.8423	14.4465	x		x	
V-472	Třebenice	rhyolite	lava	49.8379	14.4460	x	N/A*		
V-469	Třebenice	plagiogranite	subvolcanic	49.8326	14.4516	x			
V-471	Třebenice	plagiogranite	subvolcanic	49.8368	14.4479	x	N/A*	x	x
VG-474	Třebenice	plagiogranite	subvolcanic	49.8336	14.4482			x	
VG-475	Křeničná	plagiogranite	subvolcanic	49.7628	14.4032	x			
V-648	Kardavec	plagiogranite	subvolcanic	49.7279	14.0324	x			
V-488	Žampach	plagiogranite	subvolcanic	49.8688	14.4802	x			
V-490	Luka pod Medníkem	plagiogranite	subvolcanic	49.8720	14.4553	x			
17CB24	Slapy	metaboninite	dyke	49.8150	14.4288	x		x	x
M-2	Mirovice	boninite	dyke	49.5178	14.0247			x	x
K-8	Kasejovice	metaboninite	dyke	49.4739	13.7571				
X2	Třebenice	metaboninite	dyke	49.8253	14.4335	x		x	
V-107	Solenice	mafic orthogneiss	plutonic	49.6134	14.1866	x	x		
V-102	Solenice	mafic orthogneiss	plutonic	49.6100	14.1621	x		x	x
X6	Bohostice	felsic orthogneiss	plutonic	49.6045	14.1364	x		x	
X7	Stražiště	rhyolite	volcanic	49.5504	14.0029	x	x		
X8	Simínský mlýn	felsic orthogneiss	plutonic	49.5311	13.9423	x			

* Samples collected for U–Pb geochronology that were processed through the zircon separation process but were lacking zircons

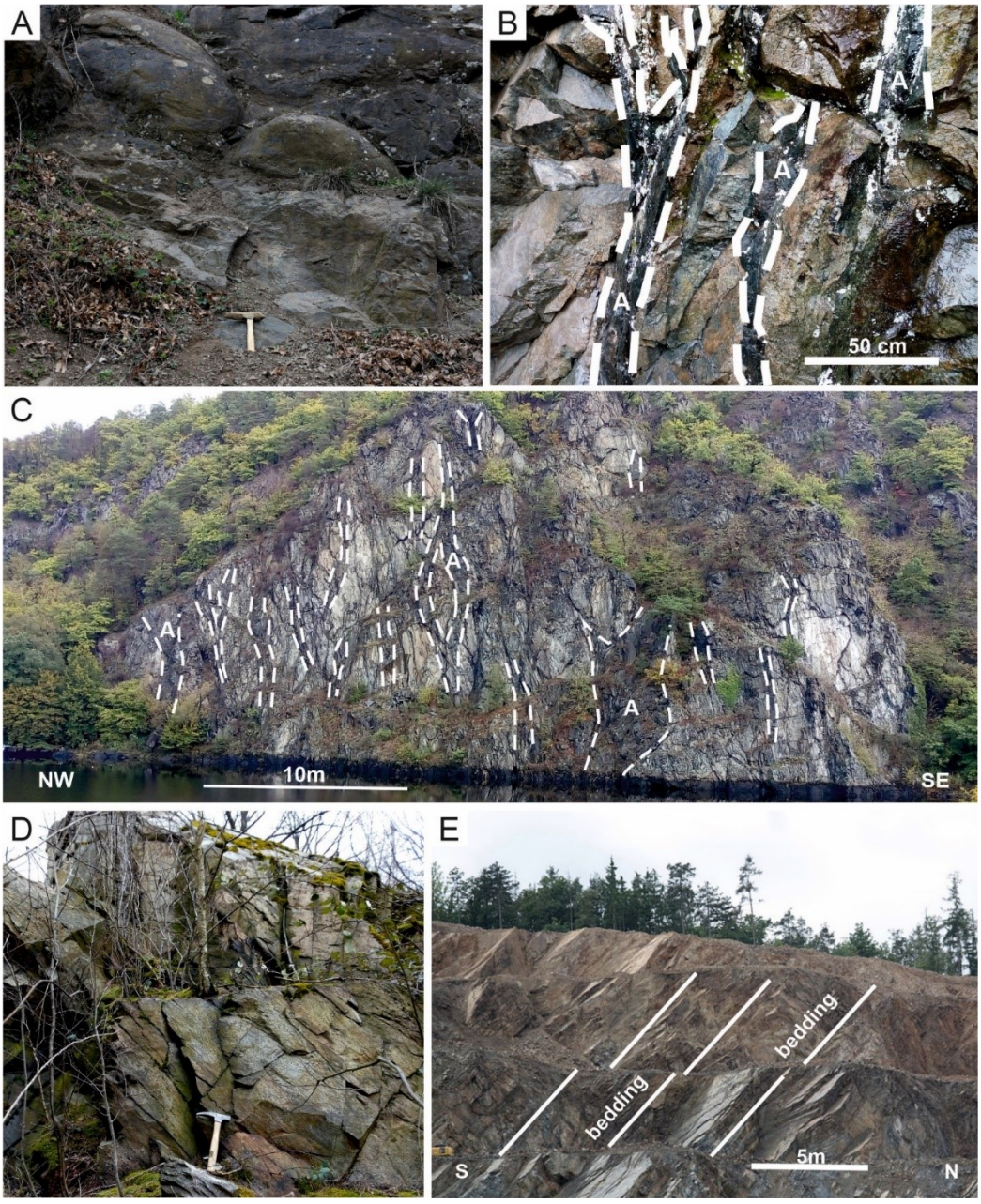

Figure 8. Lithologic features of the DVC documented on images from the field (V. Santolík). A: Andesitic pillow lavas from the Zbraslav section. B, C: Plagiogranite intercalated by andesitic lava screens near Třebenice village, which developed most probably during Variscan deformation related to the emplacement of Central Bohemian Plutonic Complex. D: Outcrop of felsic orthogneiss near Simínský mlýn village, sample X8. E: Layers of alternating rhyolitic and dacitic tuff, volcanic breccia and graywacke in Zbraslav quarry, Zbraslav section.

5.2. Major and minor element microanalysis of rock-forming minerals

Major and minor element compositions of major rock-forming silicate minerals and selected oxides were obtained using electron microprobe analyzer JEOL 8230 housed at IG CAS equipped with five WDS and one EDS detectors. The summary of analytical conditions is given in Appendix, Table 3a whereas the results are given in Appendix, Table 3b. Elements measured on WDS crystals from silicates were Si, Mg, Al, Na, K, Cr, Mn, Ca, Ti and Fe, with detection limits ~60–700 ppm (1σ) and from oxides were Si, Al, Mg, Ca, Ti, Fe, V, Ti, Zn, Cr and Mn, with detection limits ~50–1200 ppm (1σ). Different natural as well as synthetic materials were used as standards for the analysis. The analytical conditions were 15 kV accelerating voltage, 10 nA beam current and beam diameter of 2 μm for silicates and 1 μm for oxides. During the measurement of oxides, overlap correction was made for Cr and V analyses. The mineral formulas for individual species were calculated using methods described in Deer et al. (1992).

5.3. U–Pb zircon dating

Several samples of different rock types were sampled for U–Pb zircon dating, however, only two samples (mafic orthogneiss V-107 and rhyolitic dyke crosscutting felsic orthogneiss X7) yield sufficient zircon population and reliable ages. These were collected by Václav Kachlík (Faculty of Science, Charles University) and analyzed by Jiří Sláma (Bergen University/IG CAS). The other samples (plagiogranite, rhyolite and basaltic andesite) collected and processed through the mineral separation by the author unfortunately lack zircon grains. Fresh samples were collected from well-exposed outcrops and subsequently washed and crushed at the Czech Geological Survey. Zircon grains were separated using Wilfley shaking table, diiodomethane, Frantz isodynamic magnetic separator, hand-picked under binocular microscope, mounted in epoxy-filled block and polished at Bergen University, Norway. Subsequently, the sample mounts were carbon-coated and cathodoluminescence (CL) images were obtained by a scanning electron microscope Zeiss Supra 55 VP with a CL detector at Bergen University. Prior to the analysis, the carbon coating was removed and the sample surfaces were cleaned with ethanol and deionized water.

Laser ablation ICP-MS (LA–ICP–MS) U–Pb isotopic analyses of mafic orthogneiss, sample V-107, closely followed the technique described in detail in Košler et al. (2002) and in Košler and Sylvester (2003). A Thermo-Finnigan Element 2 sector field ICP-MS coupled to a 193 nm ArF excimer laser (Resonetics RESOlution M-50 LR) at the Bergen University, Norway, was used to measure Pb/U and Pb isotopic ratios. The sample introduction system was modified to enable simultaneous nebulization of a tracer solution and laser ablation of the solid sample (Horn et al., 2000). Natural Tl ($^{205}Tl/^{203}Tl = 2.3871$; (Dunstan et al., 1980), ^{209}Bi and enriched ^{233}U and ^{237}Np (>99%) solutions were aspirated to the plasma in an argon–helium carrier gas mixture through an Apex desolvation nebulizer (Elemental Scientific) and a T-piece tube attached to the back end of the plasma torch. The laser was fired at a repetition rate of 5 Hz and energy of 80 mJ. Linear laser rasters (30–100 μm) were produced by repeated scanning of the laser beam at a speed of 10 microns/second across the zircon sample surface. Typical acquisitions consisted of 40 second measurement of blank followed by measurement of U and Pb signals from the ablated zircon for another 110 seconds. The data were acquired in time resolved – peak jumping – pulse counting mode. Raw data were

corrected for dead time of the electron multiplier and processed offline in a spreadsheet-based program (LAMDATE; Košler et al., 2002). Data reduction included correction for gas blank, laser-induced elemental fractionation of Pb and U and instrument mass bias. No common Pb correction was applied to the data but the low concentrations of common Pb was controlled by observing $^{206}Pb/^{204}Pb$ ratio during measurements. Residual elemental fractionation and instrumental mass bias were corrected by normalization to the natural zircon reference material GJ-1 (Jackson et al., 2004). Zircon reference material 91500 (Wiedenbeck et al., 1995) was periodically analyzed during the measurement for quality control and the obtained mean values of 1062 ± 8 Ma (2σ) correspond with the published reference values (1065 Ma, Wiedenbeck et al., 1995). Zircon Pb/U isotope ratios that are more than >12% discordant were filtered and removed and all uncertainties of individual analyses are reported at the 2σ level.

Laser ablation ICP-MS (LA–ICP–MS) U–Pb isotopic analyses of zircons from rhyolite crosscutting the felsic orthogneiss, sample X7, closely followed the technique described in detail in Žák and Sláma (2018). A Thermo Scientific Element 2 sector field ICP-MS coupled to a 193-nm ArF excimer laser (Teledyne Cetac Analyte Excite laser) at the IG CAS, was used to measure the Pb/U and Pb isotopic ratios. Zircon reference materials GJ-1 (Jackson et al., 2004) and 91500 (Wiedenbeck et al., 1995) were periodically analyzed during the measurement for quality control. Mean Concordia age values of 1066 ± 5 Ma (2σ) for 91500 (concordance MSWD = 1.03, probability = 0.53) and slightly discordant (concordance MSWD = 2.5, probability = 0.11) Concordia age of 603 ± 4 Ma (2σ) for GJ-1 were obtained from analyses performed over the courses of different analytical sessions. These values correspond perfectly and are less than 1% within the published reference values: $^{207}Pb/^{206}Pb$ age of 1065.4 ± 0.3 Ma (Wiedenbeck et al., 1995) for 91500; $^{206}Pb/^{238}U$ age of 600.5 ± 0.4 Ma (Schaltegger et al., 2015) and $^{207}Pb/^{206}Pb$ age of 608.53 ± 0.4 Ma (Jackson et al., 2004) for GJ-1. Zircon Pb/U isotope ratios that are more than >5% discordant were filtered and removed and all uncertainties of individual analyses are reported at the 2σ level.

5.4. Whole-rock major and trace element analyses

Major element concentration analyses were carried out at the Faculty of Science, Charles University and the Czech Geological Survey, Prague. At both labs, major element concentrations were obtained by wet-chemical methods following the procedure described in Dempírová et al. (2010), combining titration, atomic absorption spectrometry, pyrohydrolysis, photometric analyses and C–S analysis. The precision of the analyses was better than ± 5% while accuracy was monitored by analysis of SY-4 syenite reference material (Canmet), which yielded results that were in excellent agreement (± 8%) with published data (Jochum and Nohl, 2008). Trace element concentrations were determined at the Faculty of Science, Charles University. The analytical protocol closely followed the procedure described by Strnad et al. (2005) and includes dry ashing at 700 °C for 6 h, modified sample digestion in mineral acids (HF–$HClO_4$) and borate fusion (Na_2CO_3 + $Na_2B_4O_7$) in Pt crucibles, and subsequent solution ICP-MS analyses (Thermo iCAP-Q). The precision of the analyses for all elements was better than ± 5% whereas accuracy was monitored by analysis of BCR-2 basalt reference material (USGS), which yielded results that were mostly in excellent agreement (< 10%) with published data (Jochum and Nohl, 2008). Only Cs and Cr contents were ~20%

lower than recommended while Hf values were ~20% higher than recommended. Data handling and plotting were carried out using R-based GCDkit toolkit (Janoušek et al., 2006) with final graphical outputs produced using CorelDRAW X7 software.

5.5. Sr–Nd–Pb isotopic analyses

The analytical procedure that include sample decomposition and elemental separation in a clean laboratory environment and instrumental analysis of Sr–Nd–Pb isotopic compositions using the Triton Plus thermal ionization mass spectrometer (TIMS; Thermo) was carried out at the IG CAS. About 150 mg of each sample was weighted, doped with appropriate amount of ^{150}Nd–^{149}Sm spike and decomposed in a mixture of 23 M HF and 7 M HNO_3 for 3 days on a hot plate at 140 °C in closed Savillex beakers. Subsequently, the samples were dried and residues repeatedly dissolved in 14 M HNO_3 and 10 M HCl in order to decompose all fluorides. The final residue was dissolved in 2 ml of 1 M HNO_3 and 100–200 mg of ascorbic acid was added to each sample to reduce Fe^{3+} to Fe^{2+} (Pin et al., 2014). Strontium, Nd, Sm and Pb were separated by ion exchange chromatography followed the procedure described in detail in Pin et al., 2014. A Sr resin (Triskem, France) was used for isolation of Sr and Pb fraction whereas combination of TRU and LN resins (Triskem, France) were used for REE isolation and extraction of Nd and Sm from the rest of REE fraction.

Strontium was loaded onto outgassed W filament, covered by Ta_2O_5 activator and analyzed by TIMS technique in a static mode with a correction for mass fractionation using $^{88}Sr/^{86}Sr = 8.3752$. In comparison, outgassed Re and Re–Ta double-filament configuration were used for Nd and Sm, respectively, and both elements were analyzed by TIMS employed in a static mode. For mass fractionation correction, $^{146}Nd/^{144}Nd = 0.7219$ for Nd and $^{147}Sm/^{152}Sm = 0.56081$ for Sm were used. The external reproducibility of Sr and Nd isotopic analyses was monitored by the periodic measurements of the NIST SRM 987 solution, which yielded a $^{87}Sr/^{86}Sr$ ratio of 0.710247 ± 0.000013 (2σ, $n = 34$) and JNdi-1 solution with a $^{143}Nd/^{144}Nd$ ratio of 0.512100 ± 0.000008 (2σ, $n = 24$). For Pb isotopic analyses, an outgassed Re filament with a single filament configuration was used. The instrumental mass bias was monitored and corrected by a long-term replicate analyses using NIST SRM 981 standard. Relative to the reference values of Todt et al. (1996), an average mass fractionation factor of 0.136 per mass unit was applied to all Pb isotopic ratios. The external reproducibility (2SD) of $^{206}Pb/^{204}Pb$, $^{207}Pb/^{204}Pb$ and $^{208}Pb/^{204}Pb$ values reflecting the long-term reproducibility of the NIST SRM 981 was ~0.007, ~0.008 and ~0.030, respectively. The measured Sr–Nd–Pb analytical data of BCR-2 reference material (USGS) were in excellent agreement with the values published by Jochum and Nohl (2008).

Isotope data handling was performed in GCDkit software (Janoušek et al., 2006). For calculation of initial Sr isotopic composition, decay constant (λ) for ^{87}Rb of 1.42×10^{-11} yr^{-1} (Steiger and Jäger, 1977) and values for present-day uniform reservoir (UR) of $^{87}Rb/^{86}Sr = 0.0816$ and $^{87}Sr/^{86}Sr = 0.7045$ (Faure, 1986) were used. For calculation of initial Nd isotopic composition, decay constant (λ) for ^{147}Sm of 6.54×10^{-12} yr^{-1} (Lugmair and Marti, 1978) and values for present-day chondritic uniform reservoir (CHUR) of $^{143}Nd/^{144}Nd = 0.512638$ and $^{147}Sm/^{144}Nd = 0.1967$ (Jacobsen and Wasserburg, 1980) were used. The model ages were calculated based on equations given by Goldstein et al. (1984) and Liew and Hofmann (1988) using values for present-day depleted mantle (DM) of $^{143}Nd/^{144}Nd = 0.51316$ and 0.513151,

respectively, and $^{147}Sm/^{144}Nd$ = 0.219. The parameter ε_{Nd} was calculated by the following equation:

$$\varepsilon_{Nd}^{t} = \left[\frac{\left(\frac{143Nd}{144Nd}\right)^{t}_{sample}}{\left(\frac{143Nd}{144Nd}\right)^{t}_{CHUR}} - 1 \right] * 10000$$

5.6. Geochemical modelling

In order to better constrain the processes responsible for generation of the DVC magmatic suite, geochemical modeling utilizing trace element as well as selected isotopic data was conducted. For this purpose, a Microsoft Excel-based program calculating fractional crystallization (FC), assimilation-fractional crystallization (AFC) and partial melting (PM) processes was created by the author. Distribution coefficients for trace elements in rock-forming minerals were taken from Ersoy and Helvaci (2010).

Rayleigh equation was used for calculating FC:

$$C_L = C_0 F^{D-1}$$

where C_L is the concentration of certain element in differentiated melt, C_0 is the concentration of the element in parental melt, F is the fraction of melt remaining and D is the bulk distribution coefficient for the crystalizing phases.

The following equation was used for calculating PM:

$$C_L = C_0 \frac{1}{F}(1 - (1 - F)^{\frac{1}{D}})$$

where C_L is the concentration of certain element in differentiated melt, C_0 is the concentration of element in solid source, F is the degree of melting and D is the bulk distribution coefficient for the residual phases (after melting).

The following equation was used for calculating AFC:

$$C_L = C_0 F^{-z} + \frac{r}{z(r-1)} \frac{C_A}{C_0}(1 - F^{-z}) \text{ , where } z = \frac{r+D-1}{r-1}$$

where C_L is the concentration of certain element in differentiated melt, C_0 is the concentration of the element in parental melt, F is the fraction of melt remaining, D is the bulk distribution coefficient for the crystalizing phases and r is the rate of assimilation to fractional crystallization.

6. Results

6.1. Petrography and mineral compositions

Detailed petrography of the studied samples is presented on Figure 9–Figure 14 showing photomicrographs obtained using optical microscopy. The back-scattered electron (BSE) images and mineral compositions obtained by the SEM imaging and microprobe analyses are presented on Figures 13–23 whereas mineral data obtained and recalculated with respect to mineral compositions are given in Appendix, Table 3b.

6.1.1. Pillow lavas

Two samples of pillow lavas (17CB01/1, 17CB23) were investigated. Sample 17CB01/1 has fine-grained texture with abundant albite and chlorite and rare quartz, titanite, Fe–Ti oxides and carbonate (Figure 9). The albite grains are prismatic, hypidiomorphic, up to 400 μm long, with no zonation and contain almost pure albite component (An_{0-1}, Figure 17). Chlorite occupies space between albite and has allotriomorphic shape. Sample 17CB23 is slightly foliated and contains abundant plagioclase and amphibole, common chlorite, quartz, magnetite, epidote and rare ilmenite, K-feldspar, biotite, muscovite and carbonate (Figure 9). Plagioclase grains vary in composition from albite to labradorite (An_{5-60}) with andesine prevailing (Figure 17). Amphibole is hypidiomorphic, up to 500 μm in size and has typically actinolite core (Si anions per formula unit – apfu > 7.8, Mg# 66–71) [Mg# = 100 x $Mg/(Mg+Fe_{tot})$] rimmed by pargasite-hornblende (Si in formula 6.4–6.9, Na in formula 0.3–0.4, Mg# 43–53, Figure 9, Figure 19). Spinel occurs as small allotriomorphic grains with nearly pure magnetite component (Figure 15).

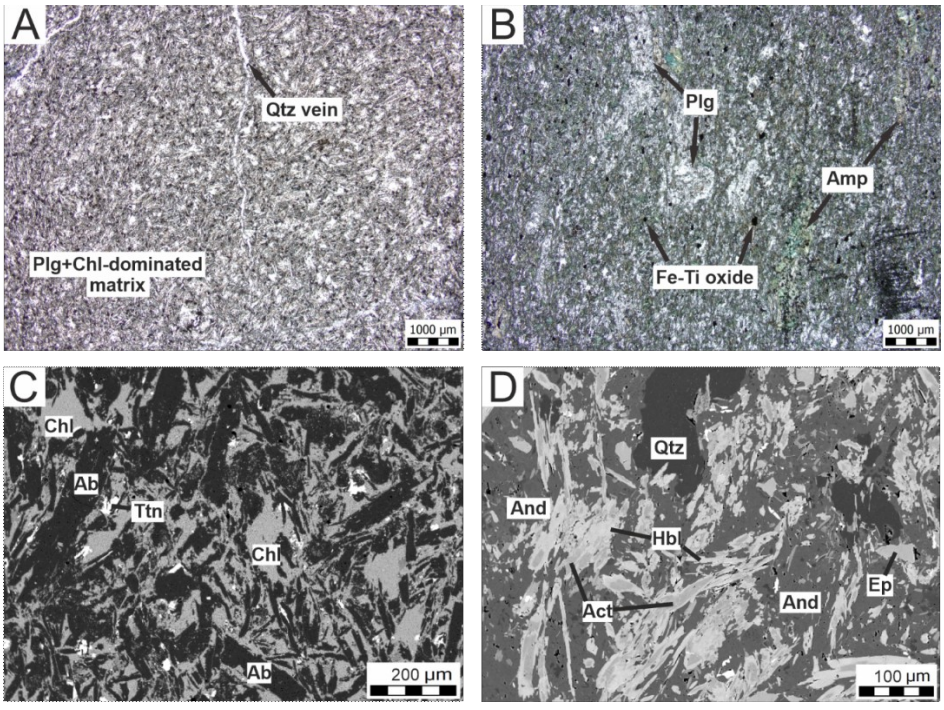

Figure 9. Photomicrographs documenting petrography of andesite and basaltic andesite pillow lavas from DVC. A, B: plane polarized light, samples 17CB01/1 and 17CB23, respectively. C, D: back-scattered (BSE) images, samples 17CB01/1 and 17CB23, respectively; Plg-plagioclase, Amp-amphibole, Ab-albite, Chl-chlorite, Ttn-titanite, Qtz-quartz, Hbl-hornblende, Act-actinolite, And-andesine, Ep-epidote.

6.1.2. Andesite dykes and lavas

Five samples of andesite dykes and lava flows (V-470, VG-473, V-487, V-1098, V-212) have been investigated. Sample V-1098 from the Zbraslav area contains abundant allotriomorphic chlorite and prismatic or spherulitic albite, common quartz and rare Fe–Ti oxides (Figure 10). Other andesitic samples have very fine-grained texture and contain abundant amphibole and plagioclase, common chlorite and Fe–Ti oxides and rare quartz (Figure 10). Plagioclase grains vary in composition from albite to andesine (An_{1-43}, Figure 17). Amphibole grains are generally very small and have actinolite cores (Si apfu 7.3–7.8, Na apfu 0.3–0.35, Mg# 56–68) and pargasite-hornblende rims (Si apfu 6.8–7.2, Mg# 51–59, Figure 10, Figure 19).

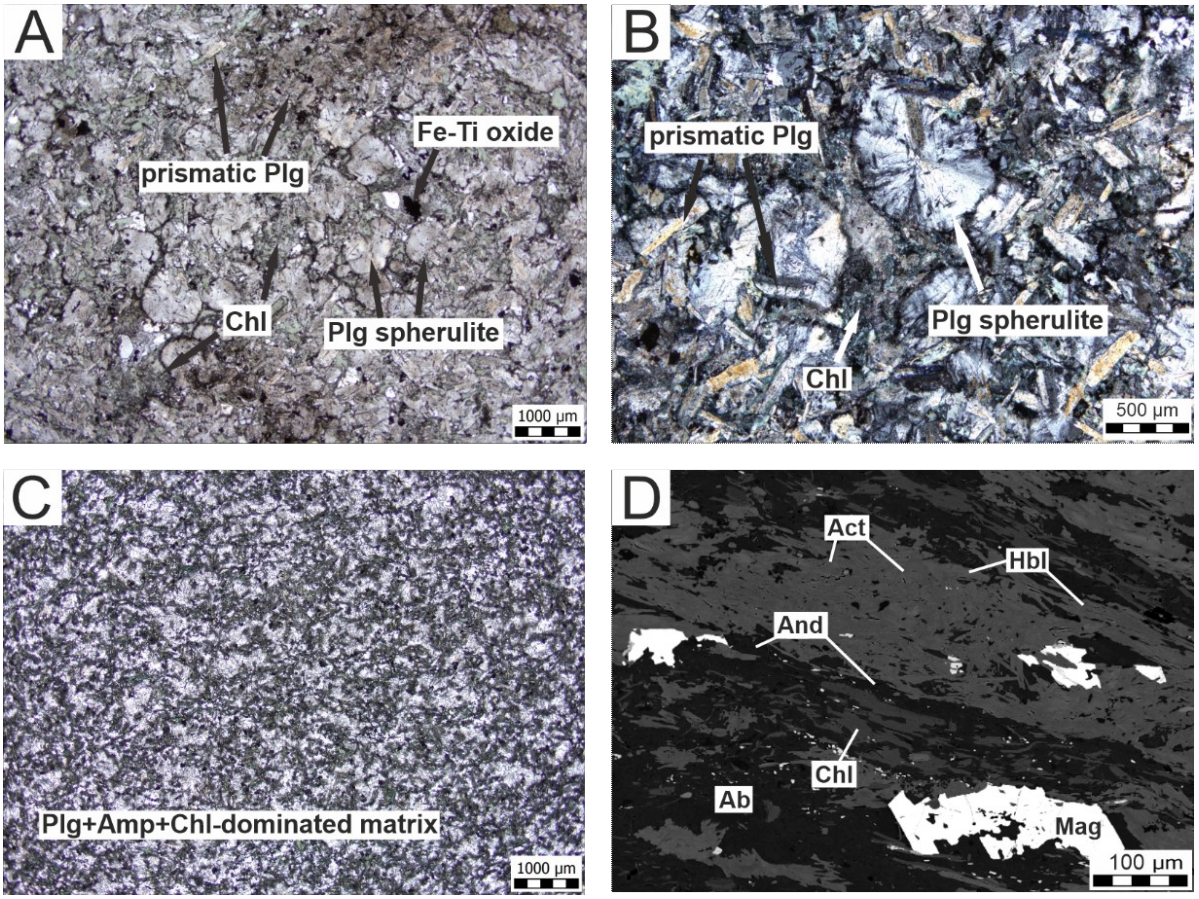

Figure 10. Photomicrographs illustrating petrography of andesite dykes and lavas. A, B: spherulitic texture in andesite from Zbraslav section, plane polarized light, sample V-1098. C: fine-grained andesite from Jílové belt, plane polarized light, sample V-487. D: fine-grained foliated andesite from Jílové belt, BSE image, sample V.470; Plg-plagioclase, Act-actinolite, Hbl-hornblende, And-andesine, Chl-chlorite, Ab-albite, Mag-magnetite.

6.1.3. Dacitic and rhyolitic dykes and lavas

One sample of dacitic (17CB27) and two samples of rhyolitic (17CB26 and V-472) dykes and lavas have been collected. They have porphyric texture with quartz and albite phenocrysts and recrystallized glassy matrix formed of quartz, plagioclase, chlorite and Fe–Ti oxides (Figure 11). In addition, dacitic lava (17CB27) contains rare biotite and amphibole. Albite phenocrysts often form idiomorphic prismatic grains with developed Carlsbad twinning.

Plagioclase in fine grained matrix varies from albite to andesine in composition (An_{0-44}, Figure 17). Amphiboles in sample 17CB27 have actinolite cores (Si apfu ~7.6, #Mg ~54) and pargasite-hornblende rims (Si apfu ~6.8, Na apfu 0.3–0.4, Mg# ~44, Figure 11, Figure 19).

6.1.4. Dacitic and rhyolitic tuff

Two samples of dacitic tuffs (17CB07/26 and 17CB29/1) and one sample of rhyolitic tuff (17CB07/28) have been investigated. They have oriented sedimentary textures with layers comprising abundant plagioclase and quartz and rare chlorite, epidote, biotite, muscovite, calcite and Fe–Ti oxides (Figure 11). Plagioclase varies in composition from albite to oligoclase (An_{2-12}, Figure 17).

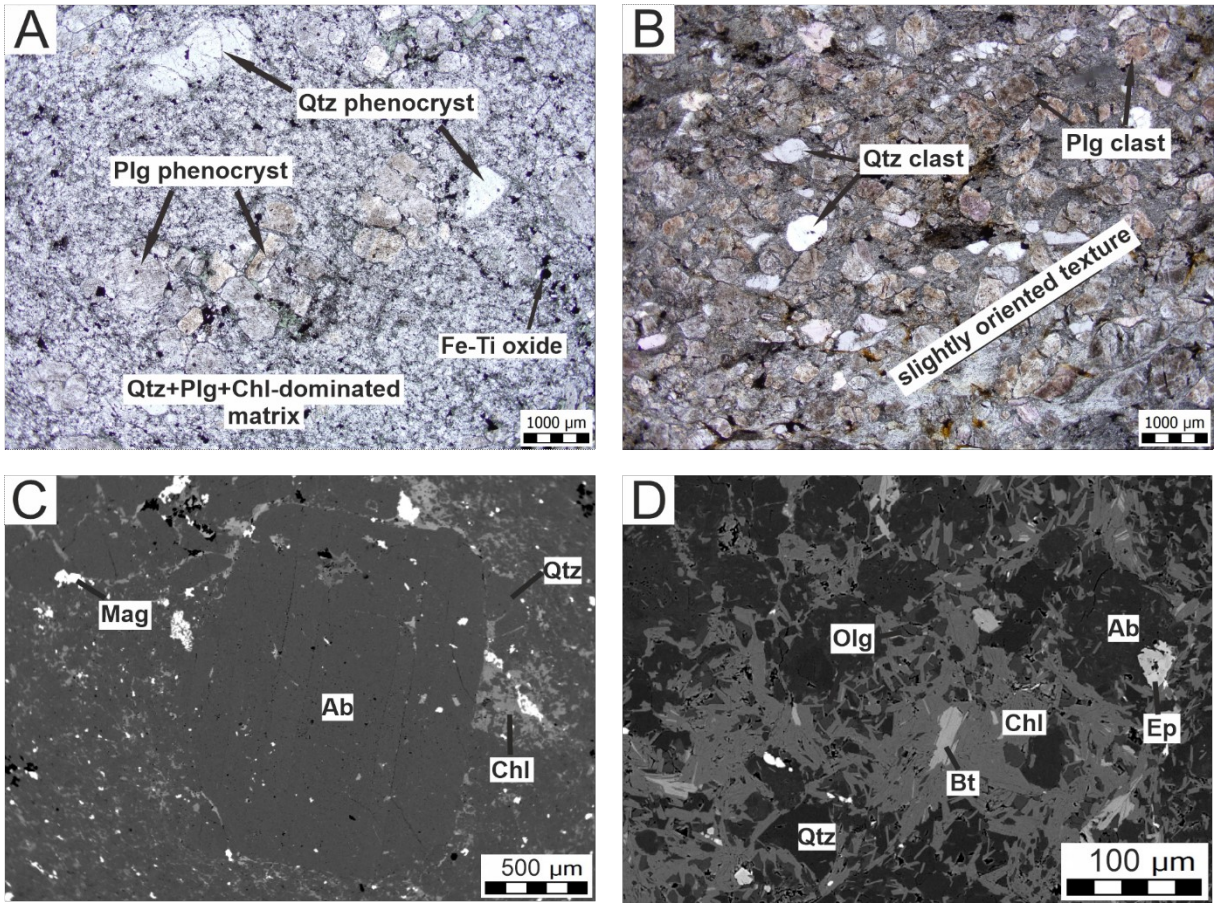

Figure 11. Photomicrographs illustrating petrography of rhyolitic and dacitic lavas and tuffs. A: rhyolitic lava, plane polarized light, sample 17CB26. B: dacitic tuff, plane polarized light, sample 17CB07/26. C: albite phenocryst in rhyolitic lava, BSE image, sample 17CB26. D: dacitic tuff, BSE image, sample 17CB29/1; Plg-plagioclase, Ab-albite, Olg-oligoclase, Chl-chlorite, Qtz-quartz, Mag-magnetite, Bt-biotite, Ep-epidote.

6.1.5. Plagiogranite

Seven samples of plagiogranite have been inspected. They have medium-grained texture comprising abundant albite and quartz, common allotriomorphic chlorite and rare epidote, K-feldspar, muscovite, amphibole, titanite, rutile, magnetite and ilmenite (Figure 12). Plagioclase has prevailing albite composition, rarely oligoclase (An_{1-21}, Figure 17). Amphibole occurs as very rare and small grains with hornblende-actinolite composition (Si

apfu 7.4–7.7, Na apfu 0.1–0.22, Mg# 70–73, Figure 19). Spinel contains almost pure magnetite component (Figure 15), whereas ilmenites have quite substantial Mn substitution for Fe^{2+} (Mn cations per formula unit - cpfu 0.1–0.15).

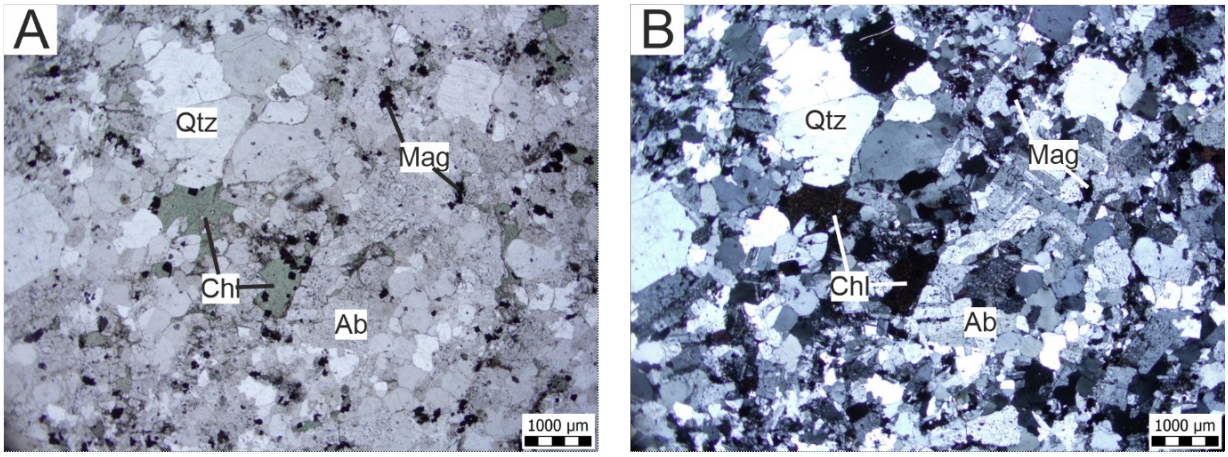

Figure 12. Photomicrograph illustrating petrography of plagiogranites. A, B: sample V-490, polarizing microscope, parallel Nicols and crossed Nicols, respectively; Qtz-quartz, Mag-magnetite, Chl-chlorite, Ab-albite.

6.1.6. Orthogneiss and related rhyolite

Two samples of mafic orthogneiss (V-102 and V-107), two samples of felsic orthogneiss (X6 and X8) and one sample of rhyolite geochemically and spatially related to the felsic orthogneiss (X7) have been investigated. All orthogneiss samples have developed metamorphic foliation and dynamic recrystallization contemporaneous with deformation. Mafic orthogneiss contains abundant quartz, plagioclase and amphibole, common K-feldspar, biotite and chlorite and rare titanite, magnetite and ilmenite (Figure 13). Plagioclase has mainly andesine composition, however, small grains of albite can be found, too ($An_{1\text{-}45}$, Figure 17). K-feldspar contains prevailing Or [Or = K/(K+Na+Ca)] component with a subtle substitution of Na for K ($Or_{93\text{-}98}$, $Ab_{2\text{-}6}$, $An_{0\text{-}0.2}$, Figure 16). As in other rock types, two generations of amphibole are common in mafic orthogneiss, actinolite occurs typically in grain cores (Si apfu 7.1–7.6, Mg# 55–63, Figure 13, Figure 19), whereas hornblende-edenite-pargasite occurs at grain rims (Si apfu 6.8–7.2, Na apfu 0.17–0.28, Mg# 48–56). Mafic orthogneiss contain two types of spinels: more common Cr-magnetite (Cr cpfu 0.2–0.35) and less common pure magnetite (Cr cpfu < 0.001, Figure 15). On contrary, felsic orthogneiss comprises abundant quartz, common plagioclase, K-feldspar and biotite, rare epidote, muscovite, chlorite and Fe–Ti oxides but no amphibole (Figure 13). Plagioclase is oligoclase to andesine in composition ($An_{20\text{-}45}$, Figure 17) and K-feldspar contains prevailing Or component with a subtle substitution of Na for K ($Or_{93\text{-}97}$, $Ab_{3\text{-}6}$, $An_{0\text{-}0.4}$ Figure 16). Rhyolite related to felsic orthogneiss (sample X7) has porphyric and slightly oriented texture. Phenocrysts are mainly quartz, less commonly plagioclase or K-feldspar. Very fine grained and slightly foliated matrix contains abundant quartz and plagioclase, common K-feldspar and biotite, rare Fe–Ti oxides and possibly other minor minerals.

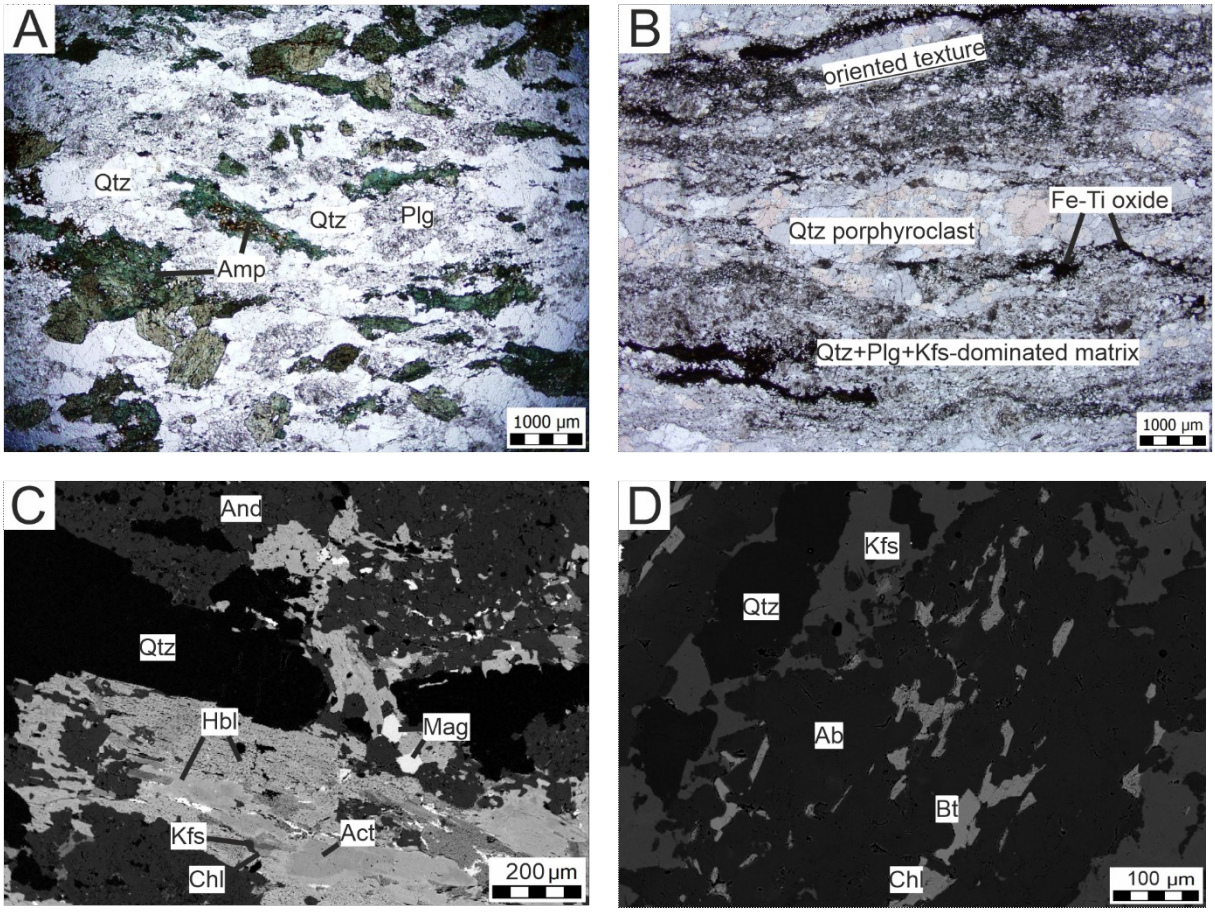

Figure 13. Photomicrograph illustrating petrography of orthogneiss. A: mafic orthogneiss, plane polarized light, sample V-102. B: felsic orthogneiss, plane polarized light, sample X6. C: mafic orthogneiss, BSE image, sample V-102. D: felsic orthogneiss, BSE image, sample X6; Qtz-quartz, Amp-amphibole, Plg-plagioclase, And-andesine, Hbl-hornblende, Mag-magnetite, Kfs-K-feldspar, Act-actinolite, Chl-chlorite, Ab-albite, Bt-biotite.

6.1.7. Boninite

Four samples of boninite have been studied, three of which are considerably metamorphosed and recrystallized (17CB24, K-2 and X2) but one sample (M-2) retains the original magmatic texture and composition. The rocks are porphyric, comprising clinopyroxene or amphibole (uralite) phenocrysts and fine-grained matrix composed of variable amount of plagioclase and amphibole (or pyroxene) and rare K-feldspar, biotite, muscovite, epidote, chlorite and Fe–Ti–Cr oxides (Figure 14). Clinopyroxenes occur as two types. In phenocryst cores, diopside-augite prevails with Mg# 85–90, whereas rims and matrix are dominated by diopside-hedenbergite with Mg# 35–70 (Figure 14, Figure 18). Amphibole occurs also in two varieties. Actinolite is found in grain cores (Si apfu 7.6–7.9, Mg# 64–84) whereas pargasite-hornblende forms grain rims (Si apfu 6–6.7, Na apfu 0.45–0.8, Mg# 47–64, Figure 14, Figure 19). Plagioclase grains have wide range of composition from albite to anorthite (An_{1-97}, Figure 17). Albite is found only in the most deformed and metamorphosed sample (X2) as very small grains in matrix, while plagioclase of labradorite to anorthite composition is found only in the least metamorphosed sample (M-2). The major part of plagioclase grains are oligoclase to andesine in composition and are found in all boninite

samples. Magnetite (Al+Cr cpfu < 0.02) is very rare and small and has allotriomorphic shapes. In contrast, chromite is more common and comprise two types. Firstly, small idiomorphic grains with considerable substitution of Fe^{3+} for Cr (Fe^{3+} cpfu 0.4–0.6) occur as inclusions in pyroxene phenocrysts. Secondly, large allotriomorphic grains with considerable substitution of Al for Cr (Al cpfu ~0.3) occur in the matrix (Figure 15, A-C).

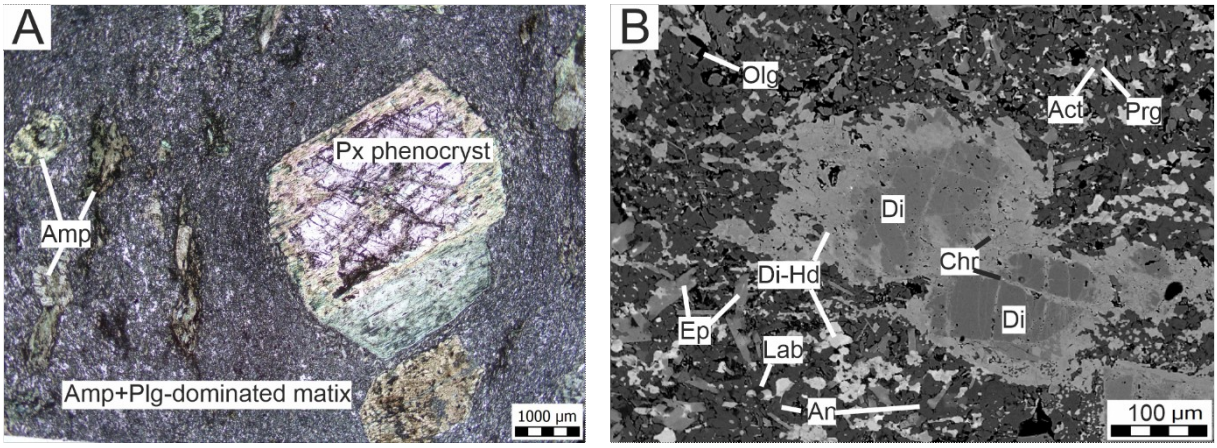

Figure 14. Photomicrograph illustrating petrography of boninites. A: foliated texture with clinopyroxene phenocryst, sample 17CB24, plane polarized light. B: weakly deformed and metamorphosed boninite, sample M-2, BSE image; Amp-amphibole, Px-pyroxene, Olg-oligoclase, Lab-labradorite, An-anorthite, Act-actinolite, Prg-pargasite, Di-diopside, Di-Hd - diopside-hedenbergite, Chr-chromite, Ep-epidote.

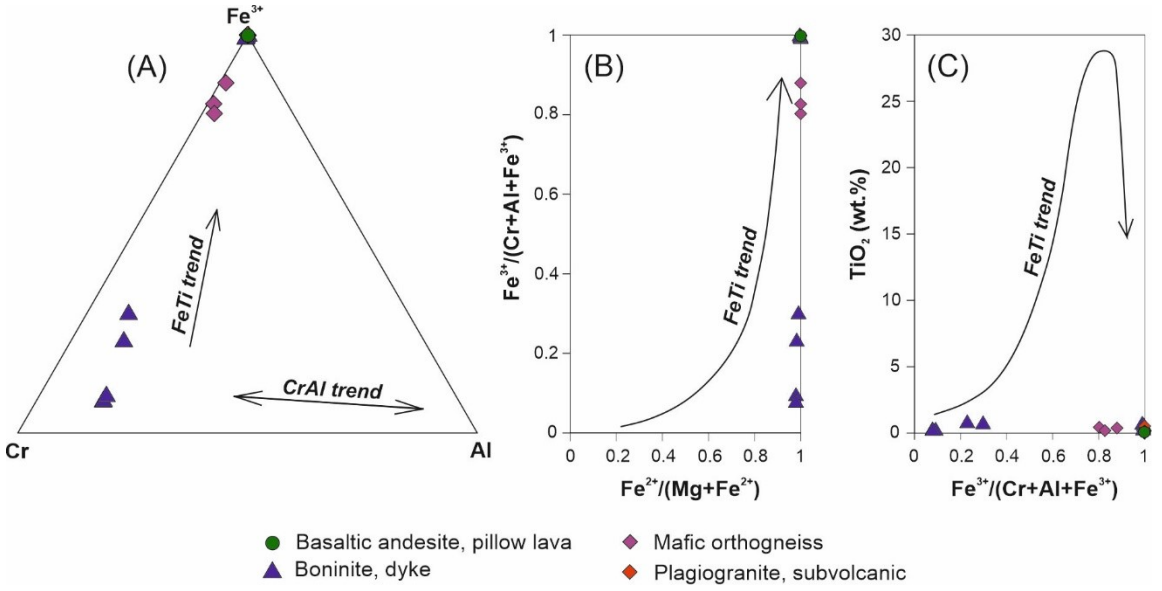

Figure 15. Classification diagrams for spinel from basaltic andesite, boninite, mafic orthogneiss and plagiogranite of the DVC, after Barnes and Roeder, 2001. All analyzed rocks contain spinels of nearly pure magnetite component, mafic orthogneiss contains a slightly Cr-enriched component in addition and boninite contains chromite grains in addition.

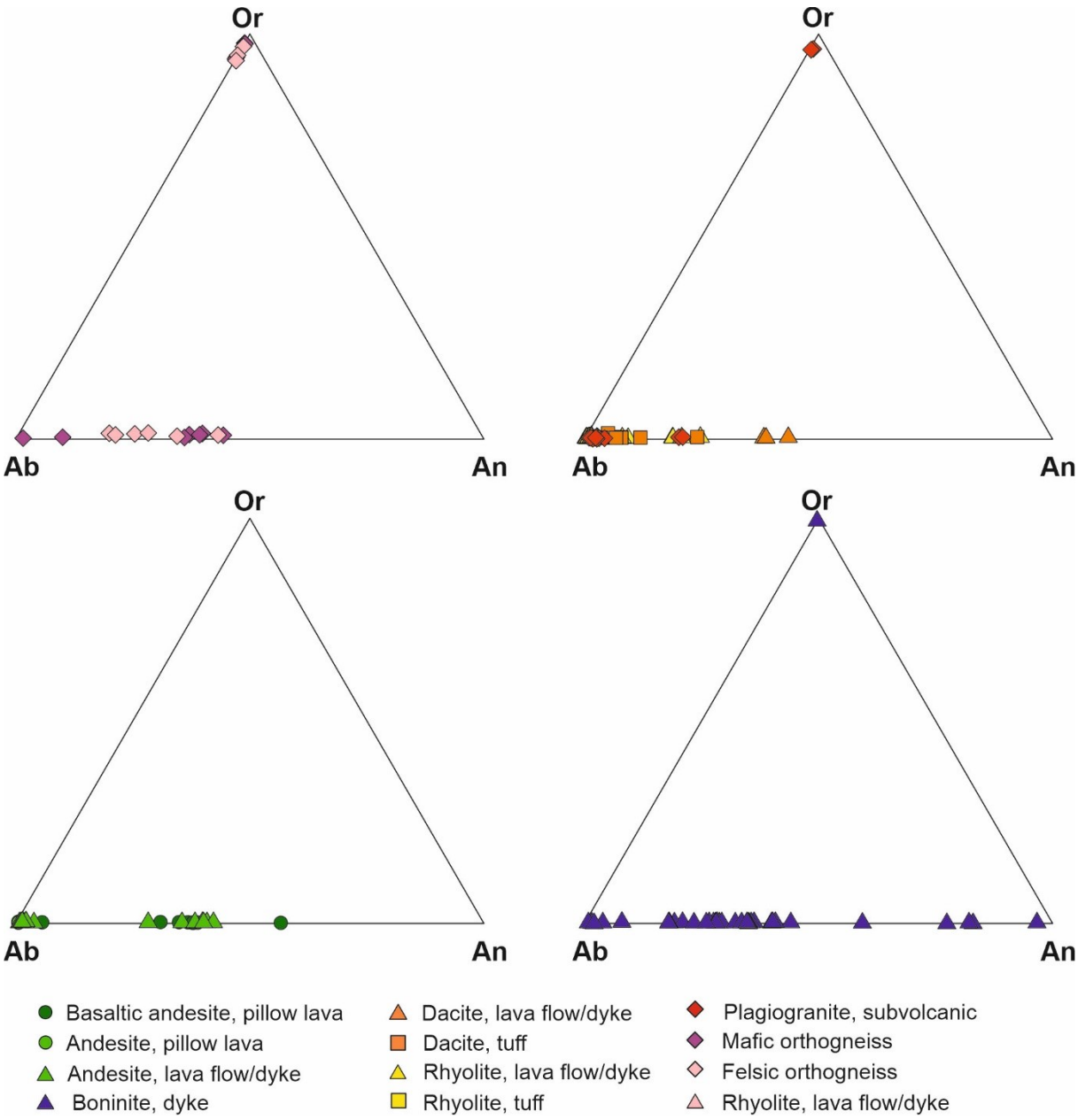

Figure 16. Ternary diagrams illustrating feldspar composition from different rock types of the DVC. Note that plagioclase prevails in most samples, only orthogneisses contain larger amounts of K-feldspars.

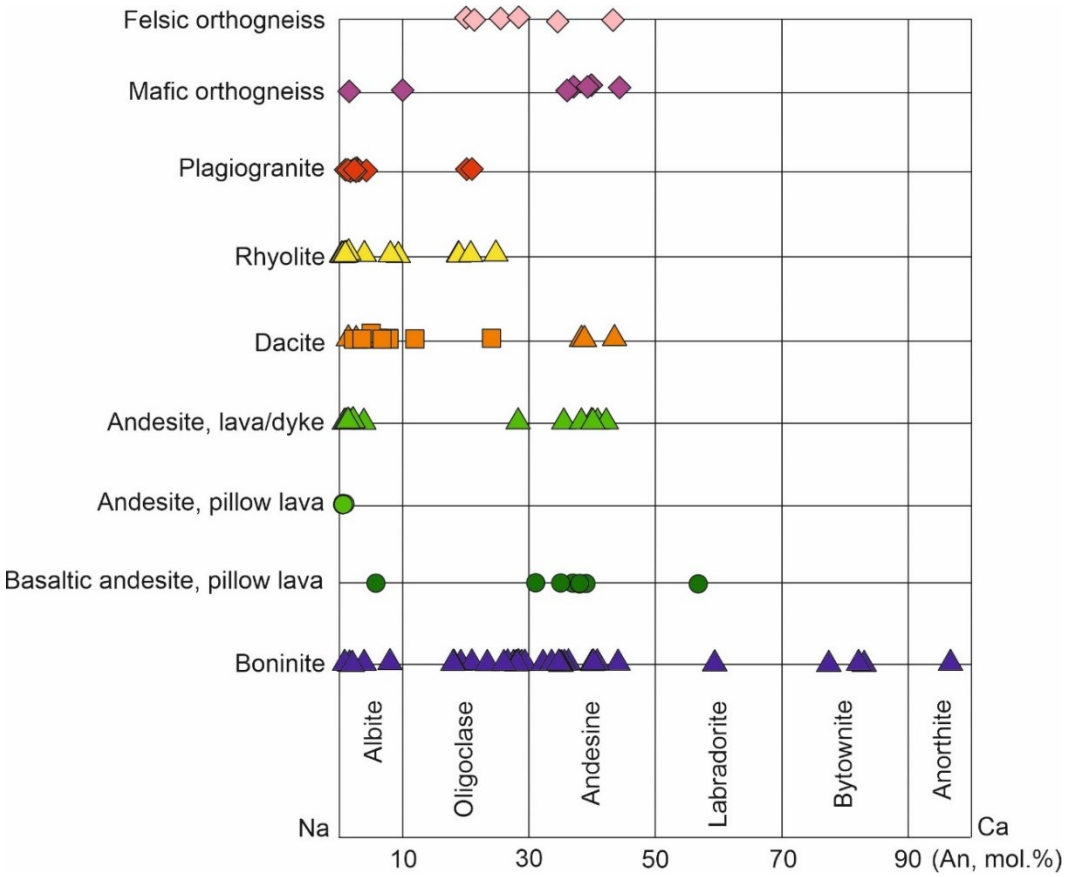

Figure 17. Binary diagram showing plagioclase composition of different rock types from the DVC. Albite prevails in most cases, oligoclase and andesine are also quite common but labradorite to anorthite composition is present only rarely in boninite and andesitic pillow lava.

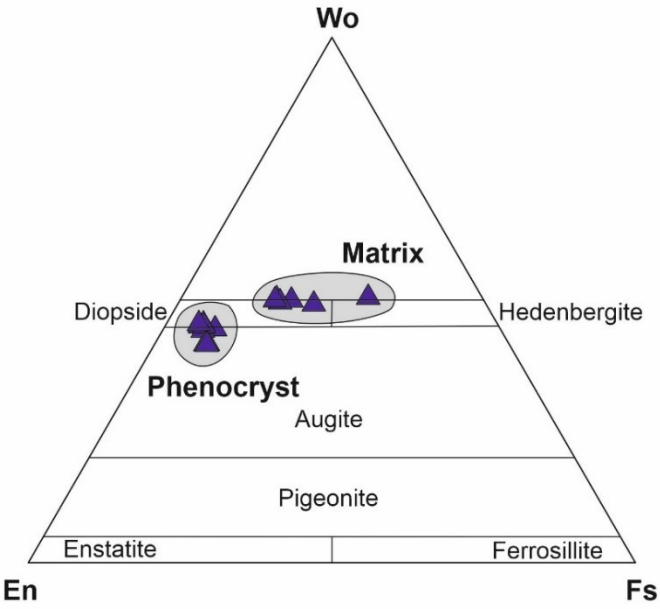

Figure 18. Pyroxene classification diagram after Morimoto (1988), showing diopside-augite composition of the phenocryst grains and diopside-hedenbergite composition of the grains in matrix of boninites from the DVC.

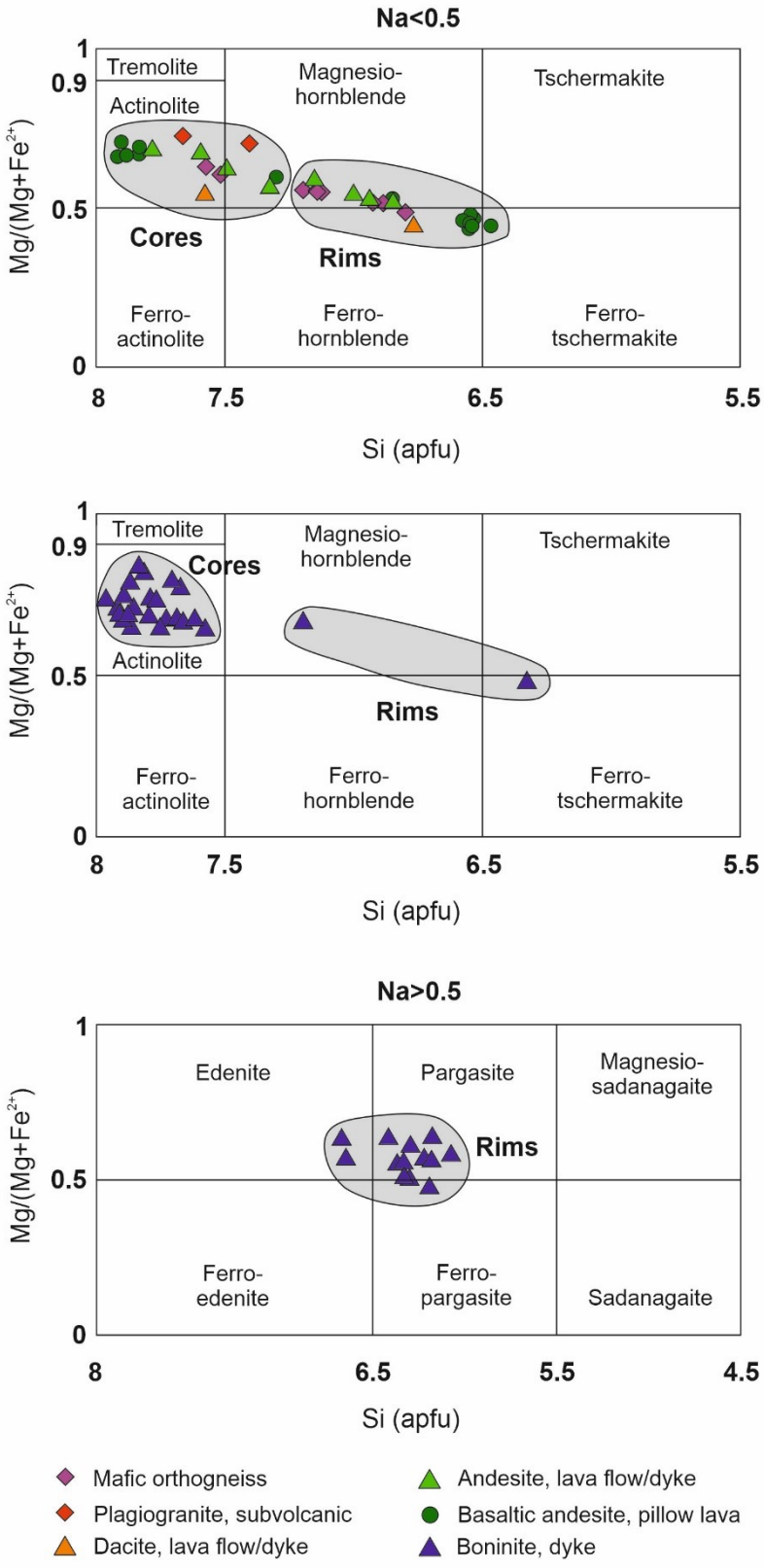

Figure 19. Amphibole classification diagram after Leake et al. (1997), showing actinolite composition of the grain cores but hornblende-pargasite composition of the grain rims of different rock types from the DVC.

6.2. *U-Pb geochronology*

Several attempts have been made to extract zircon from different types of rocks from the DVC (see Methods). However, only in two cases, zircon fraction was gathered, still with rather limited zircon grain amount, but reliable U–Pb zircon ages were obtained. The results are given in Appendix, Table 2, and are displayed on concordia diagrams, Figure 20.

The zircon grains extracted from sample V-107 (mafic orthogneiss) are long-prismatic, often preserve idiomorphic shapes and are 100–300 μm in size. They preserve oscillatory growth with sector zoning and are without inherited cores. One dominant cluster can be seen at the Pb–U concordia diagram giving the age of 608.3 ± 7.8 Ma (MSWD = 0.84, probability = 0.36, 16 analyses, Figure 20), which is interpreted as the age of protolith intrusion.

The zircon grains of sample X7 (rhyolitic dyke cross-cutting the felsic orthogneiss) are prismatic, up to 300 μm in size. They provide $^{207}Pb/^{235}U$ ages that span between 597 and 633 Ma. Eleven grains from the total of 14 grains define a discordia line with upper intercept at 637 ± 11 Ma (MSWD = 2.5, 11 analyses, Figure 20). This age may either represent the age of rhyolite dyke intrusion, the age of felsic orthogneiss protolith intrusion or the age of underlying older lithologies, since volcanic dyke rocks often contain zircon grains from the surrounding lithologies.

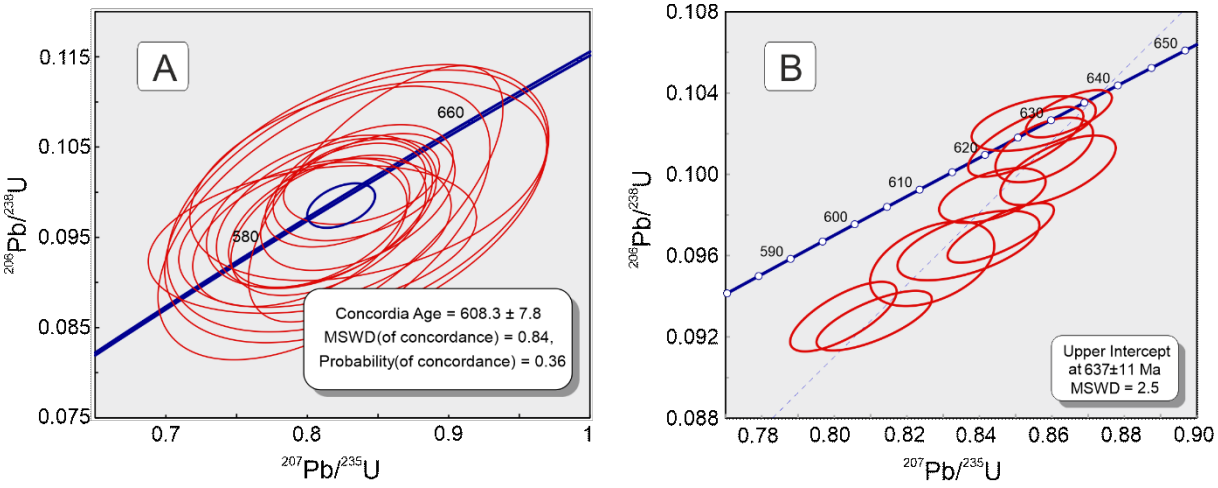

Figure 20. Concordia diagrams of samples V-107 (A) and X7 (B).

6.3. *Whole-rock geochemistry*

Whole-rock geochemical data are presented in Figures 25–36, Table 3 (isotope compositions) and in Appendix, Table 1 (major and trace element concentrations).

6.3.1. *Major element compositions*

The volcanic, subvolcanic and plutonic rocks of the DVC range from basaltic andesite to rhyolite (SiO_2 contents from 49.5 wt. % to 76.8 wt. %, Figure 21) and differ in many aspects, however, there can by stated some general trends valid for all samples, in sense of major elements. These include low TiO_2, low K_2O, low P_2O_5 and high Na_2O contents. Harker diagrams (Figure 22) display negative correlations between MgO, CaO and FeOt with

increasing SiO_2 contents. When boninites are excluded, Al_2O_3 displays also negative correlation with SiO_2 contents while P_2O_5, Na_2O and K_2O display no visible relationship. On AFM diagram (Figure 23), a clear calc-alkaline trend is characteristic for the whole DVC suite. Despite these similarities, distinct rock types differ in various major element aspects. The most distinct group are the boninites that differentiate by their low SiO_2 and Al_2O_3, but high MgO, FeOt and CaO concentrations compared to the rest of the suite. The orthogneisses differ from other samples by higher K_2O contents. Otherwise, the whole suite approximately follows the trends described above.

Three plutonic suites from DVC can be distinguished also in terms of major element compositions. While mafic orthogneiss contains ca. 63.5 wt. % SiO_2, felsic orthogneiss as well as plagiogranite tend to be more siliceous with SiO_2 contents between 72 and 77 wt. % SiO_2 (Figure 21). Mafic orthogneiss has also higher MgO, CaO, FeOt and Al_2O_3 and lower Na_2O contents. All granitic samples follow calc-alkaline trend with a felsic orthogneiss being the most differentiated member of the whole suite (Figure 23). Based on discrimination diagrams designed by Frost et al. (2001), the rocks fall in the calcic and magnesian suites (Figure 24). Based on discrimination diagram designed by O'Connor (1965), the plagiogranite falls in the field of trondhjemite because of their high Na_2O but low CaO and K_2O contents, whereas the mafic and felsic orthogneiss plot on the border between granodiorite and tonalite (Figure 25).

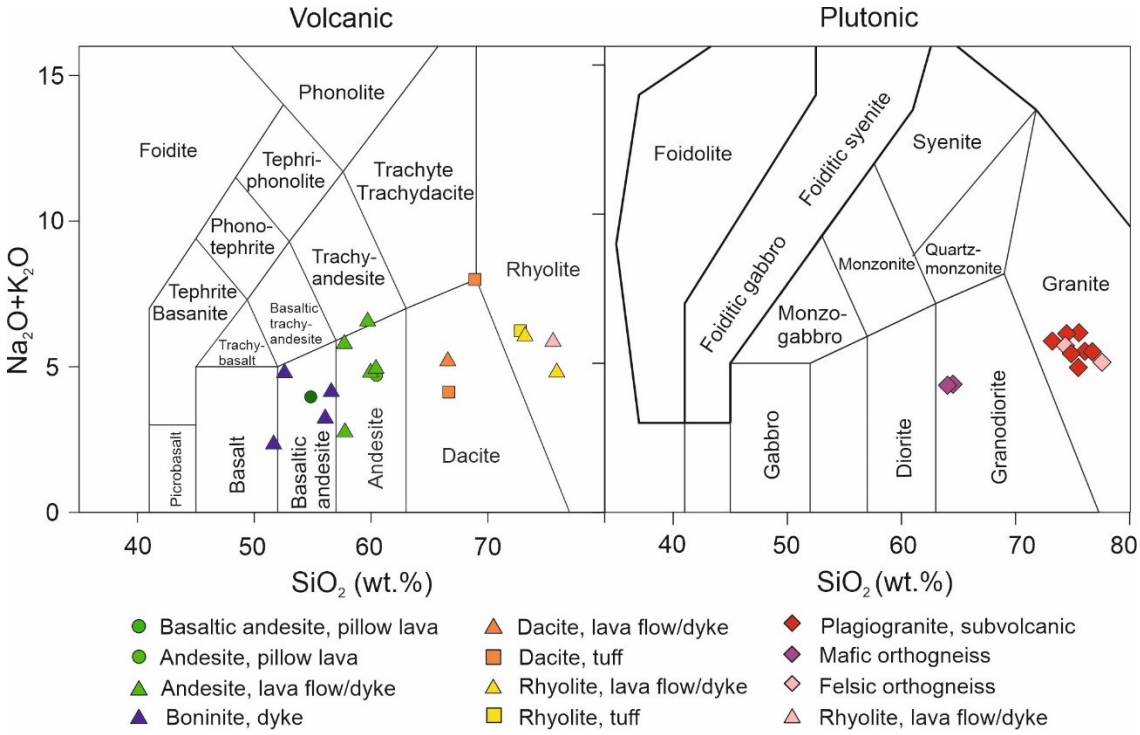

Figure 21. Whole-rock compositions of DVC rocks plotted in the Total Alkali – Silica (TAS) diagram after Le Bas et al. (1986).

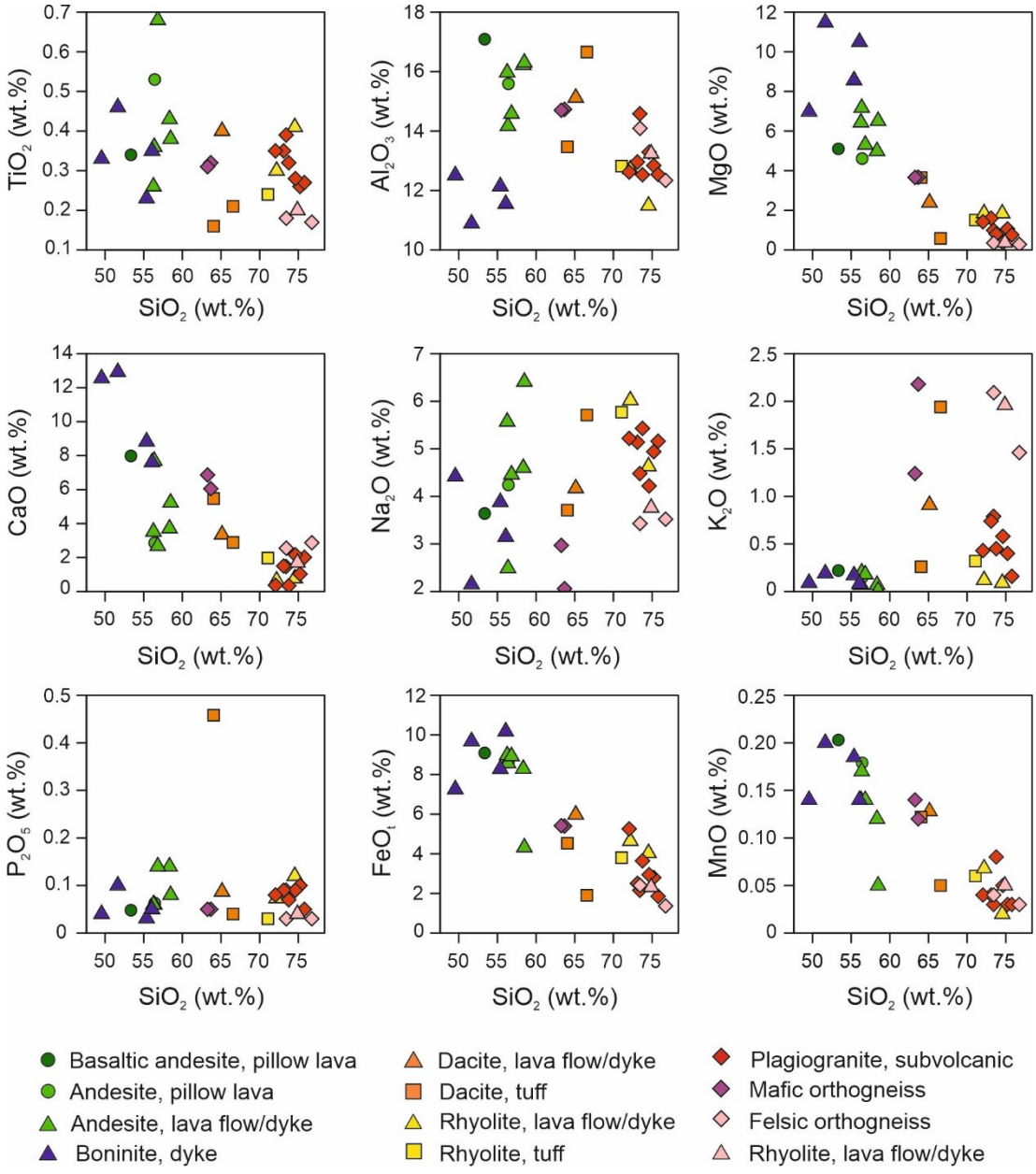

Figure 22. Whole-rock major element compositions of the DVC rocks expressed in Harker's diagrams.

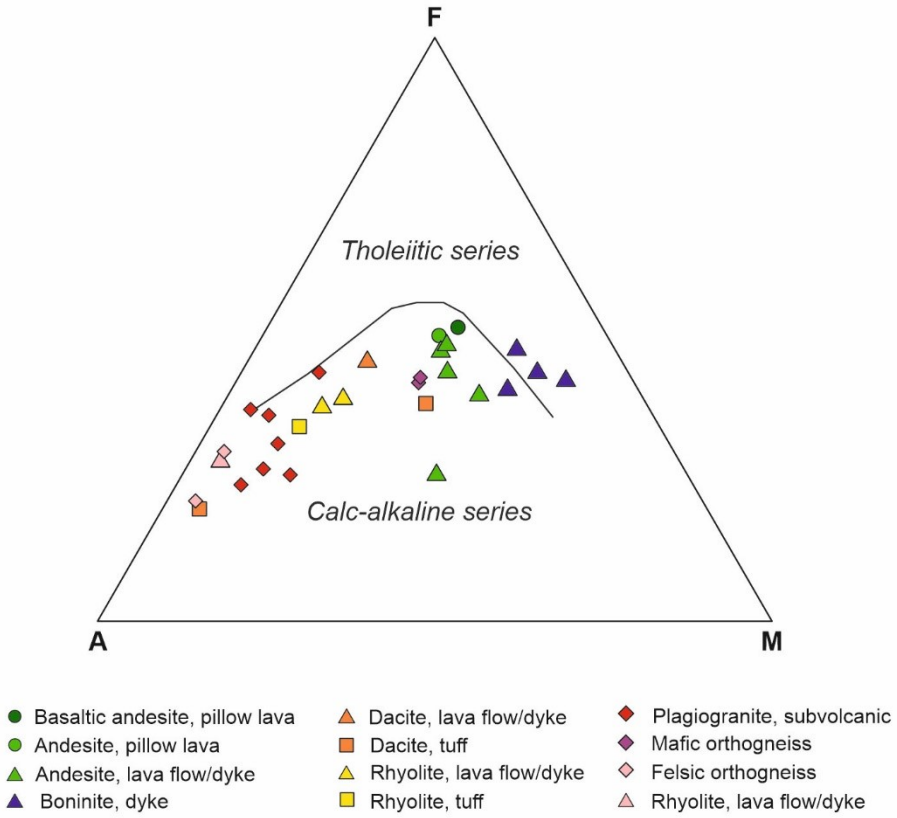

Figure 23. Samples of the DVC displayed in AFM Diagram; A = $Na_2O + K_2O$, M = MgO, F = FeO_t.

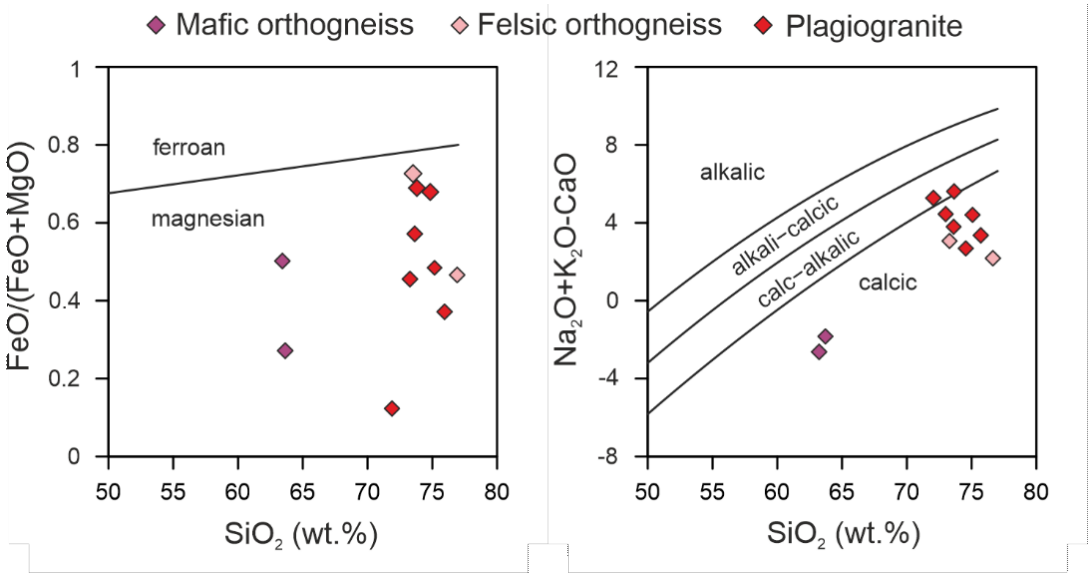

Figure 24. Samples of the DVC plutonic and subvolcanic rocks displayed in diagram for granitic rocks after Frost et al. (2001).

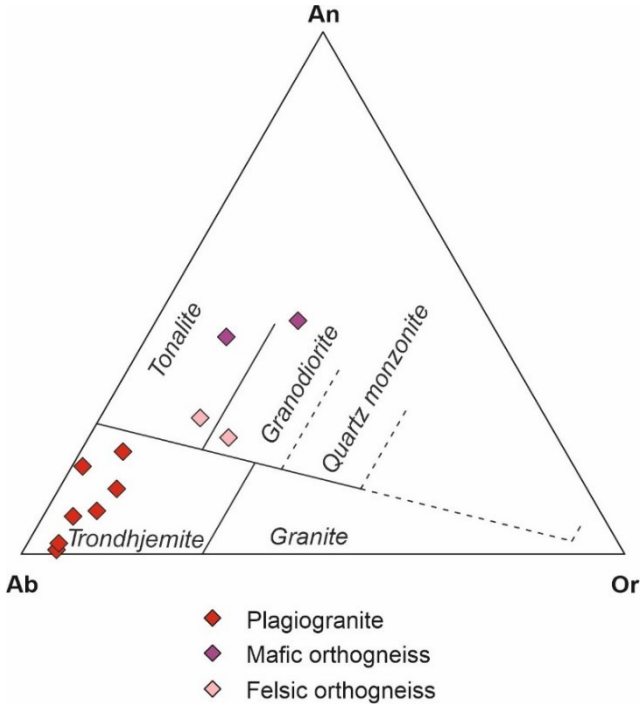

Figure 25. Samples of the DVC plutonic and subvolcanic rocks displayed in diagram for granitic rocks after O'Connor (1965).

6.3.2. Trace element geochemistry

Rare earth elements (REE) patterns normalized to primitive mantle (William F. McDonough and Sun, 1995) have more or less flat distributions $(La/Yb)_N$ = ~1–3 (Figure 27), only orthogneiss, tuffs and two boninite samples are significantly LREE enriched $(La/Yb)_N$ = ~2.5–12). Moderately negative Eu anomaly can be observed in most felsic rocks (Eu/Eu* = ~0.6–1). Looking on the REE variations with SiO_2 contents (Figure 28), two different trends can be distinguished, considering felsic rocks. On one hand, with increasing SiO_2 content, LREEs in orthogneiss show highly positive trend, whereas in plagiogranites and rhyolites, they do not show any considerable relationship. On the other hand, HREEs and Y show highly positive correlation in plagiogranites and rhyolites, but no considerable trend in orthogneiss, with increasing SiO_2 contents.

In terms of other trace element composition, all samples follow typical subduction-related signatures such as LILE enrichment and HFSE depletion (Figure 26). Notably, Cs, Ba, U and Pb are enriched whereas Nb, P and Ti are depleted. Tantalum was removed from the dataset, since many samples show anomalously high contents perhaps due to contamination during whole rock powder preparation whereas some others have data below detection limit. Rubidium is depleted relative to other LILE in all samples $(Rb/Ba)_N$ = ~0.1–0.6) except orthogneiss and 17CB07/26 dacite, both rocks containing larger quantities of K-feldspar and biotite concentrating this element. Strontium is depleted only in felsic rocks ($(Sr/La)_N$ = ~0.2–0.8) since they are lacking basic plagioclase. Chromium and Ni are depleted in all samples except for boninites showing very high contents of these elements most likely bounded to high clinopyroxene contents (Figure 29). Other transitional metals such as Sc, V, Co, Cu and Zn follow fractionation trends, where they are rich in mafic rocks and poor in felsic rocks

(Figure 29). Concentrations of Ba, Th, U and Pb are moderately elevated in most of the rocks: $(Ba)_N$ = ~5–40, $(Th)_N$ = ~3–20, $(U)_N$ = ~15–50, $(Pb)_N$ = ~5–30, however, in orthogneiss, they exhibit highly elevated values: $(Ba)_N$ = ~80–160, $(Th)_N$ = ~50–140, $(U)_N$ = ~80–150, $(Pb)_N$ = ~40–150. Zirconium and Hf do not show considerable anomalies [$(Zr/Nd)_N$ = ~0.8–1.2)]. With an increasing SiO_2 content, their concentration of Zr and Hf increases, too, however, they are more enriched in the orthogneisses compared to the rest of the rocks (Figure 29). When plotting Th vs. U/Th and Th vs. Ba/Th (Figure 31), two major trends can be recognized: (1) a predominant Th poor and U + Ba rich trend that comprises all samples except orthogneiss and (2) U + Ba poor and Th rich trend characteristic for orthogneiss.

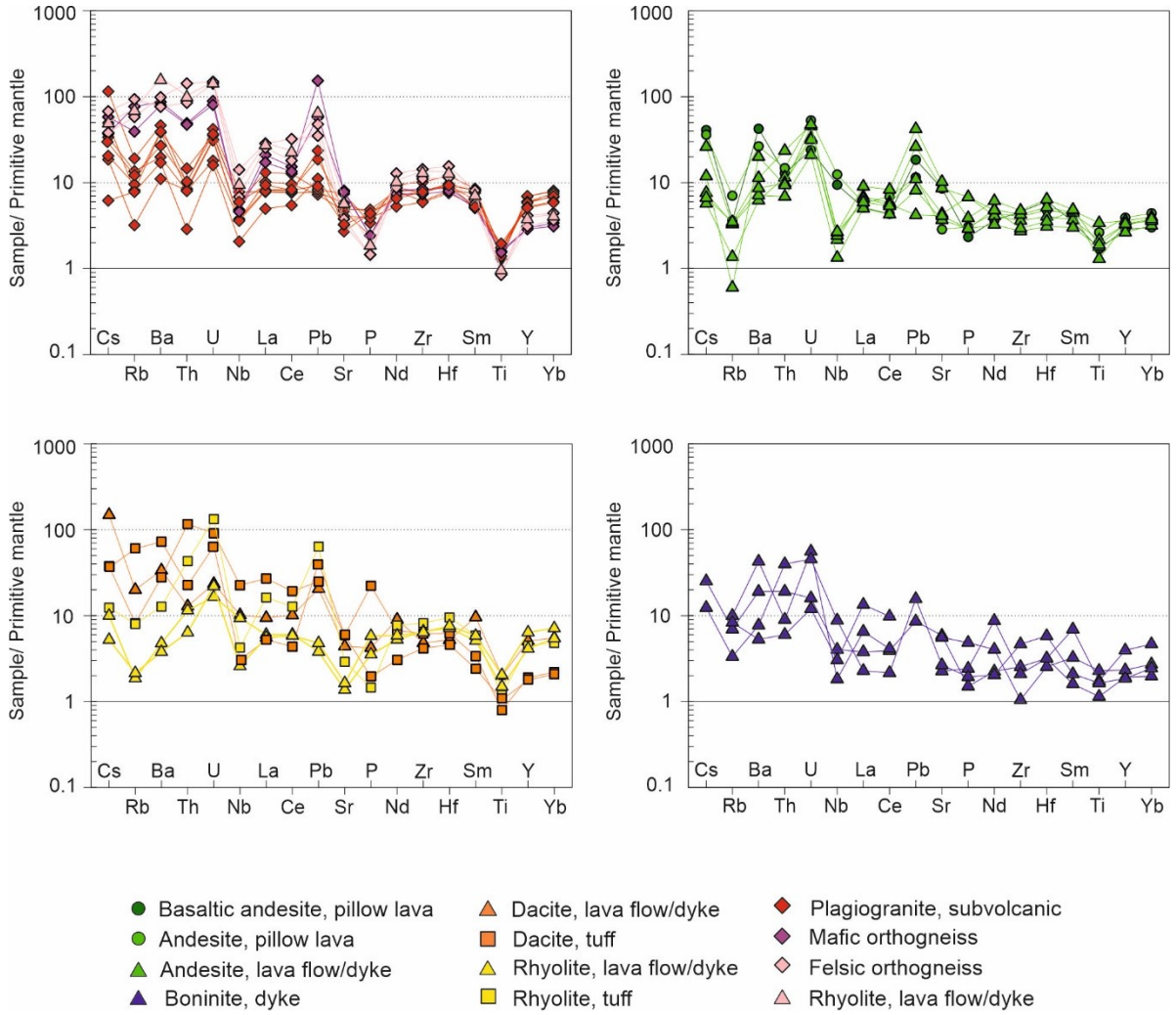

Figure 26. Incompatible element spider diagrams for all samples normalized to primitive mantle (McDonough and Sun, 1995).

.

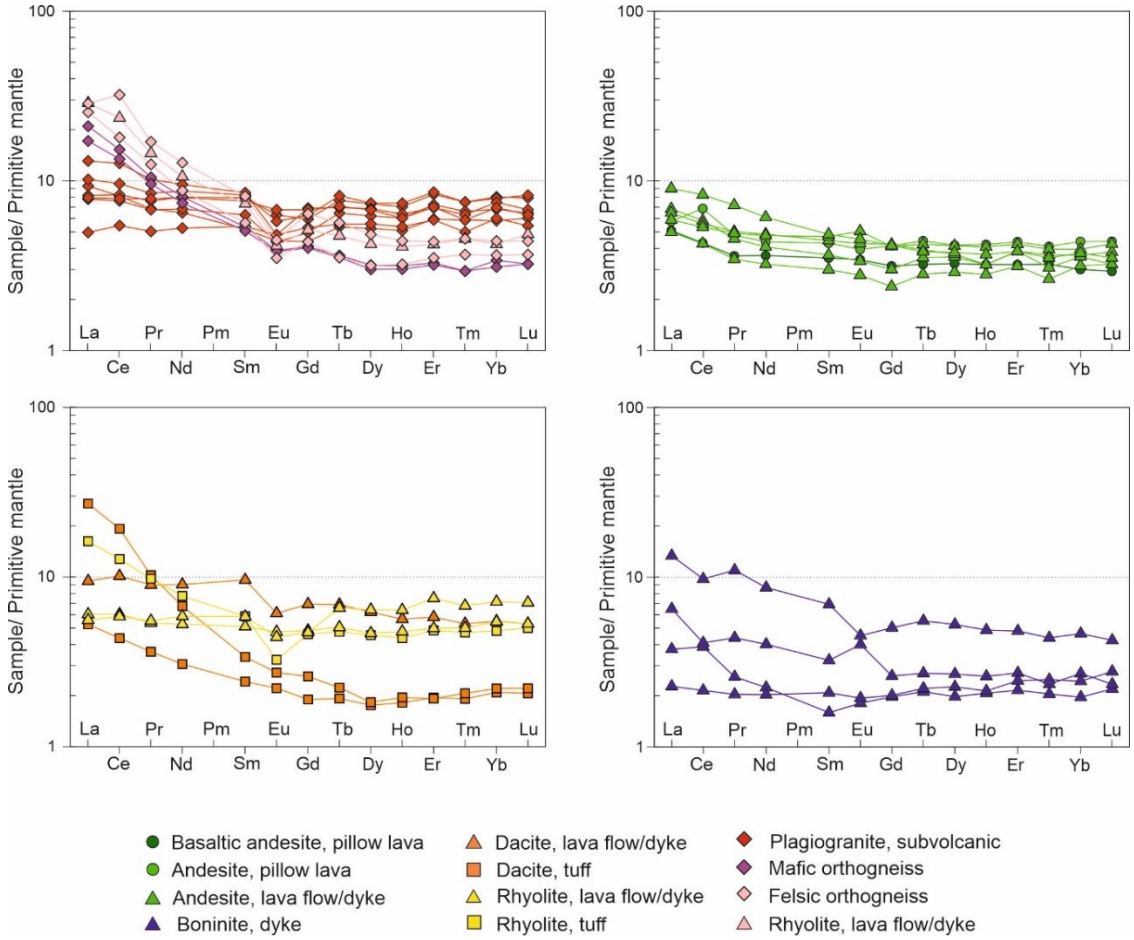

Figure 27. REE spider diagrams for all samples normalized to primitive mantle (McDonough and Sun, 1995).

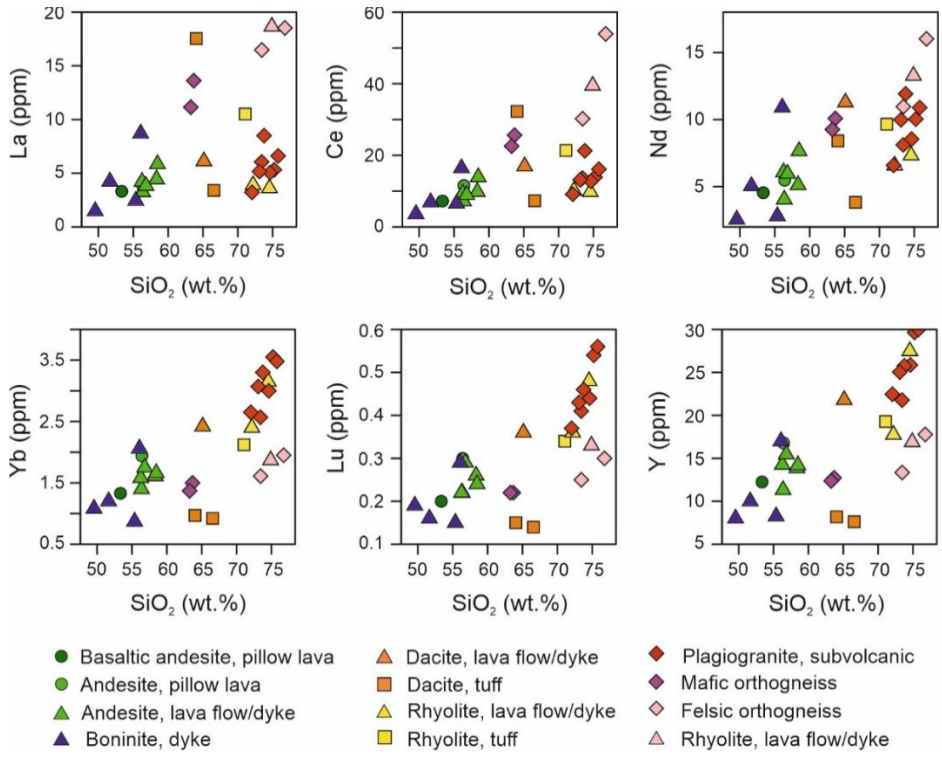

Figure 28. Variations of REEs with SiO_2 contents for the DVC samples.

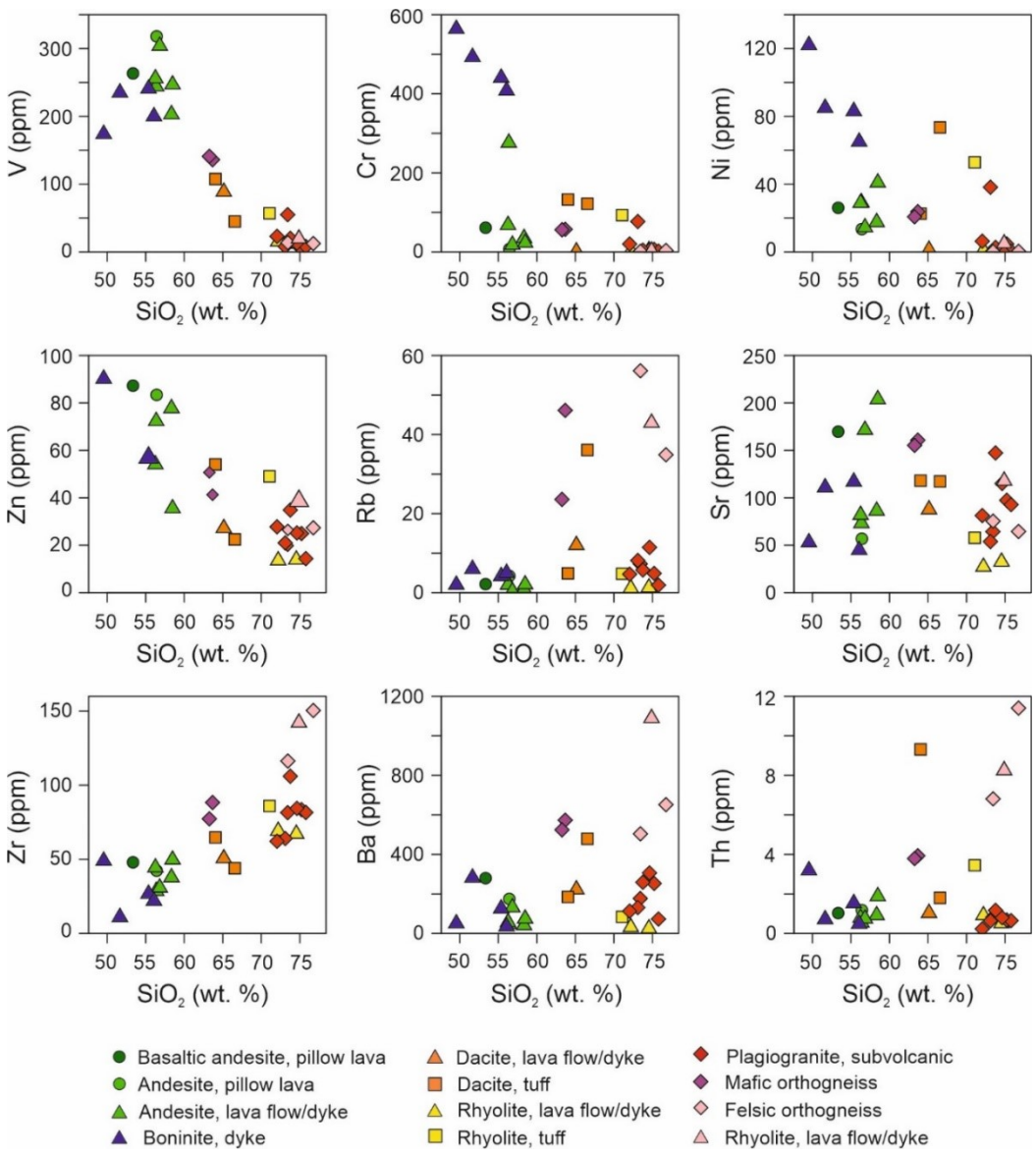

Figure 29. Variations of selected trace elements with SiO_2 contents of the DVC samples.

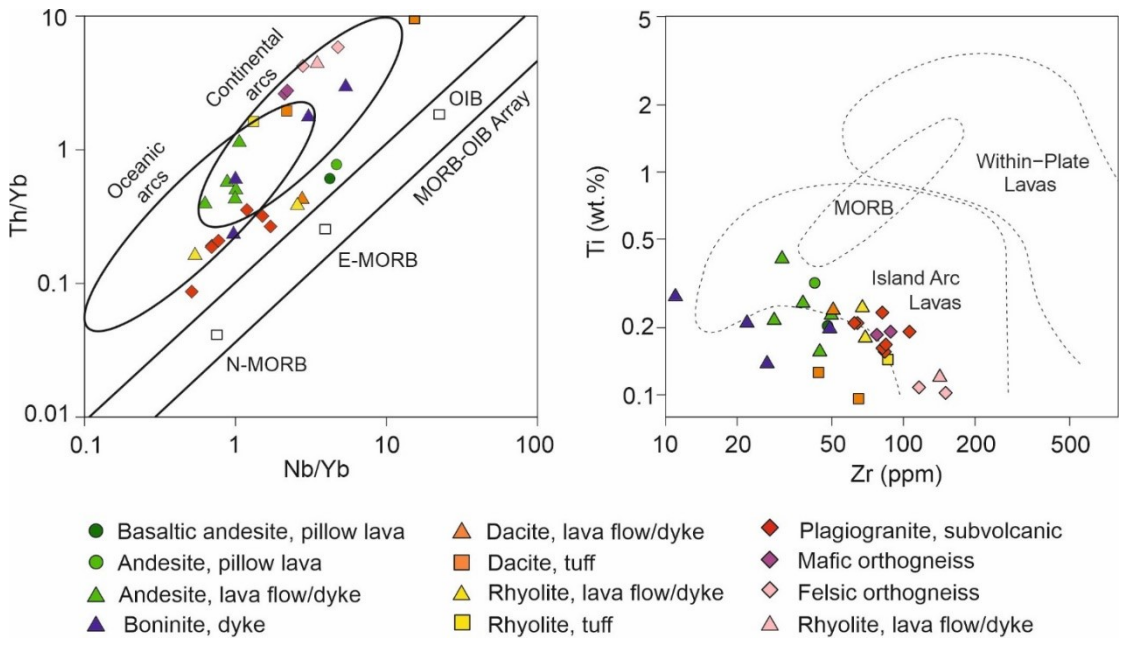

Figure 30. Geotectonic discrimination diagrams Th/Yb vs. Nb/Yb (Pearce, 2014) and Zr vs Ti (Pearce, 1982) showing subduction affinity of the DVC rocks.

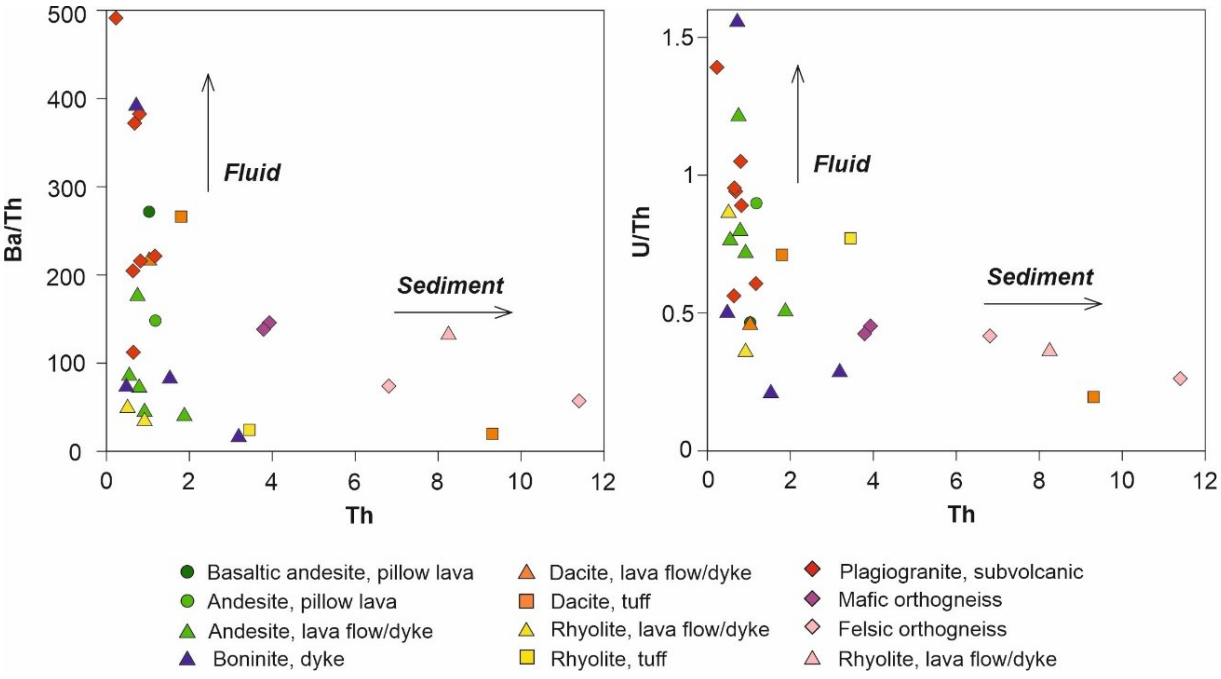

Figure 31. Melt source discrimination diagrams after (Hawkesworth et al., 1997). Most of the DVC samples follow the Ba/Th and U/Th enrichment trend arguing for fluid enriched source but orthogneisses and dacitic tuff 17CB29/1 follow Th enrichment trend which stands for magma source enriched in sediment derived melt.

6.4. Sr–Nd–Pb isotope geochemistry

The present-day as well as initial (~600 Ma) Sr-Nd-Pb isotopic data are listed in Tables 3 and 4. Different rock types distinguished above show variable isotopic signatures (Figure 32) and therefore, they are considered separately. Pillow lavas of andesite and basaltic andesite composition show highly positive ε_{Nd} values, +9.7 and +11.3, respectively, which is even higher then theoretical values of DM (Goldstein et al., 1984; Liew and Hofmann, 1988; Workman and Hart, 2005). Their initial $^{87}Sr/^{86}Sr$ values are 0.7064 and 0.7051, respectively. In contrast, other andesite samples have lower ε_{Nd} values ranging from –1.5 to +3.6 while their initial $^{87}Sr/^{86}Sr$ values are similar ranging from 0.7047 to 0.7064. Rhyolites, plagiogranites and dacitic lava sample 17CB27 have similar isotopic characteristics, with ε_{Nd} values ranging from +6.0 to +8.7 and two-stage DM model ages from 0.57 to 0.78 Ga, with one outlier (rhyolite V-472) having the ε_{Nd} value of +10.4. Their initial $^{87}Sr/^{86}Sr$ values are 0.7030–0.7049. The isotopic signatures of boninites are characterized by positive ε_{Nd} values +3.8 and +5.8 and initial $^{87}Sr/^{86}Sr$ values of ~0.7049. Mafic and felsic orthogneiss and related rhyolite show completely different isotopic characteristics than the rest of the suite having negative ε_{Nd} values from –5.1 to –3.1 and initial $^{87}Sr/^{86}Sr$ values 0.7054–0.7077.

Only several samples have been analyzed so far for Pb isotopic compositions, which do not permit to distinguish different reservoirs for various rock types, however, there are some characteristic features for the whole suite (Figure 32). Initial lead isotopic signature shows a wide scatter of the $^{206}Pb/^{204}Pb$ ratios (~17–19.5) but rather narrow interval of $^{207}Pb/^{204}Pb$ and $^{208}Pb/^{204}Pb$ ratios (~15.45–15.65 and ~36–39, respectively). Only a dacitic tuff sample 17CB29/1 provides a considerably lower $^{208}Pb/^{204}Pb$ ratio (~33.5). The analyzed samples approximately plot on the North Hemisphere Reference Line (NHRL, 600 Ma) on $^{208}Pb/^{204}Pb$ vs. $^{206}Pb/^{204}Pb$ diagram but above the NHRL (600 Ma) on $^{207}Pb/^{204}Pb$ vs. $^{206}Pb/^{204}Pb$ diagram, providing values close to the "SK" evolutionary curve of Stacey and Kramers (1975) (Figure 32).

Table 3

Sr-Nd isotopic compositions of the studied samples from the DVC.

Sample	Rock Type	Rb (ppm)	Sr (ppm)	$^{87}Sr/^{86}Sr$	$^{87}Sr/^{86}Sr$ (i)	Nd (ppm)	Sm (ppm)	$^{143}Nd/^{144}Nd$	ε_{Nd}	T_{DM} Nd (Ga)
17CB23	basaltic andesite	2.2	170	0.705378 ± 6	0.70506	4.7	1.4	0.513192 ± 11	11.3	0.36
17CB01/1	andesite	4.2	57	0.708232 ± 7	0.70639	6.0	1.9	0.513120 ± 7	9.7	0.49
V-470	andesite	0.82	86	0.705117 ± 5	0.70488	6.5	1.9	0.512657 ± 6	2.0	1.10
VG-473	andesite	2.0	73	0.705410 ± 8	0.70474	4.5	1.3	0.512766 ± 8	3.6	0.97
V-487	andesite	2.0	82	0.705268 ± 7	0.70467	8.2	2.3	0.512724 ± 7	3.0	1.02
V-1098	andesite	0.36	172	0.706465 ± 7	0.70641	8.4	2.2	0.512547 ± 10	-1.5	1.37
V-212	andesite	2.1	204	0.705774 ± 7	0.70552	8.4	2.1	0.512552 ± 6	1.5	1.14
17CB27	dacite	12	88	0.706880 ± 6	0.70348	11	3.9	0.513006 ± 8	6.2	0.76
17CB29/1	dacitic tuff	4.9	118	0.706271 ± 7	0.70524	6.7	1.3	0.512291 ± 21	0.8	1.19
17CB26	rhyolite	1.1	27	0.705517 ± 7	0.70450	6.5	2.3	0.513044 ± 9	8.4	0.59
V-472	rhyolite	1.3	33	0.705247 ± 8	0.70427	7.5	2.5	0.513167 ± 7	10.4	0.43
V-469	plagiogranite	7.3	64	0.707407 ± 8	0.70461	8.2	2.2	0.512866 ± 5	7.5	0.67
V-471	plagiogranite	4.9	97	0.705223 ± 9	0.70398	10	3.3	0.513075 ± 12	8.7	0.57
VG-475	plagiogranite	11	115	0.705698 ± 8	0.70323	8.6	2.7	0.512932 ± 9	6.9	0.71
V-648	plagiogranite	5.8	147	0.705862 ± 7	0.70490	13	3.4	0.512861 ± 8	6.0	0.78
V-488	plagiogranite	8.2	54	0.707159 ± 6	0.70342	11	3.2	0.512974 ± 22	7.3	0.68
V-490	plagiogranite	4.7	81	0.704415 ± 6	0.70299	7.1	2.3	0.513084 ± 12	8.4	0.59
17CB24	metaboninite	4.2	117	0.705782 ± 7	0.70490	3.0	0.9	0.512713 ± 8	5.8	0.80
X2	metaboninite	1.7	53	0.705813 ± 10	0.70488	2.4	0.8	0.512849 ± 9	3.8	0.96
V-107	mafic orthogneiss	46	161	0.713448 ± 6	0.70634	9.9	2.1	0.512217 ± 5	-3.1	1.50
V-102	mafic orthogneiss	24	155	0.709867 ± 6	0.70610	9.5	2.1	0.512229 ± 7	-3.2	1.51
X6	felsic orthogneiss	56	75	0.723904 ± 7	0.70545	11	2.2	0.512108 ± 10	-5.0	1.64
X7	rhyolite	43	118	0.715188 ± 6	0.70616	14	2.8	0.512136 ± 9	-5.1	1.65
X8	felsic orthogneiss	35	65	0.721080 ± 8	0.70767	17	3.4	0.512143 ± 8	-4.1	1.58
BCR-2	reference			0.705006 ± 6				0.512615 ± 4		
BCR-2	reference			0.705009 ± 6				0.512611 ± 5		

Table 4

Pb isotopic compositions of the studied samples from the DVC.

Sample	Rock Type	U/Pb	$^{206}Pb/^{204}Pb$	$^{207}Pb/^{204}Pb$	$^{208}Pb/^{204}Pb$	$^{206}Pb/^{204}Pb$ (i)	$^{207}Pb/^{204}Pb$ (i)	$^{208}Pb/^{204}Pb$ (i)
17CB23	basaltic andesite	0.17	19.160	15.577	37.960	18.088	15.512	37.226
17CB01/1	andesite	0.61	21.347	15.713	38.174	17.407	15.477	36.776
V-1098	andesite	0.23	19.941	15.620	38.433	18.481	15.532	38.045
17CB27	dacite	0.15	19.917	15.640	38.219	18.953	15.582	37.543
17CB29/1	dacitic tuff	0.49	20.461	15.660	38.544	17.349	15.473	33.474
V-472	rhyolite	0.61	20.996	15.741	39.118	17.037	15.504	37.653
V-471	plagiogranite	0.23	20.973	15.710	38.780	19.495	15.622	38.279
V-648	plagiogranite	0.57	20.578	15.689	39.223	16.916	15.470	37.296
V-488	plagiogranite	0.10	19.930	15.671	39.133	19.279	15.632	38.763
V-490	plagiogranite	0.19	19.165	15.620	38.326	17.968	15.548	38.051
V-107	mafic orthogneiss	0.21	19.520	15.610	38.316	18.219	15.532	37.400
BCR-2	reference		18.767	15.606	38.67			
BCR-2	reference		18.756	15.629	38.735			

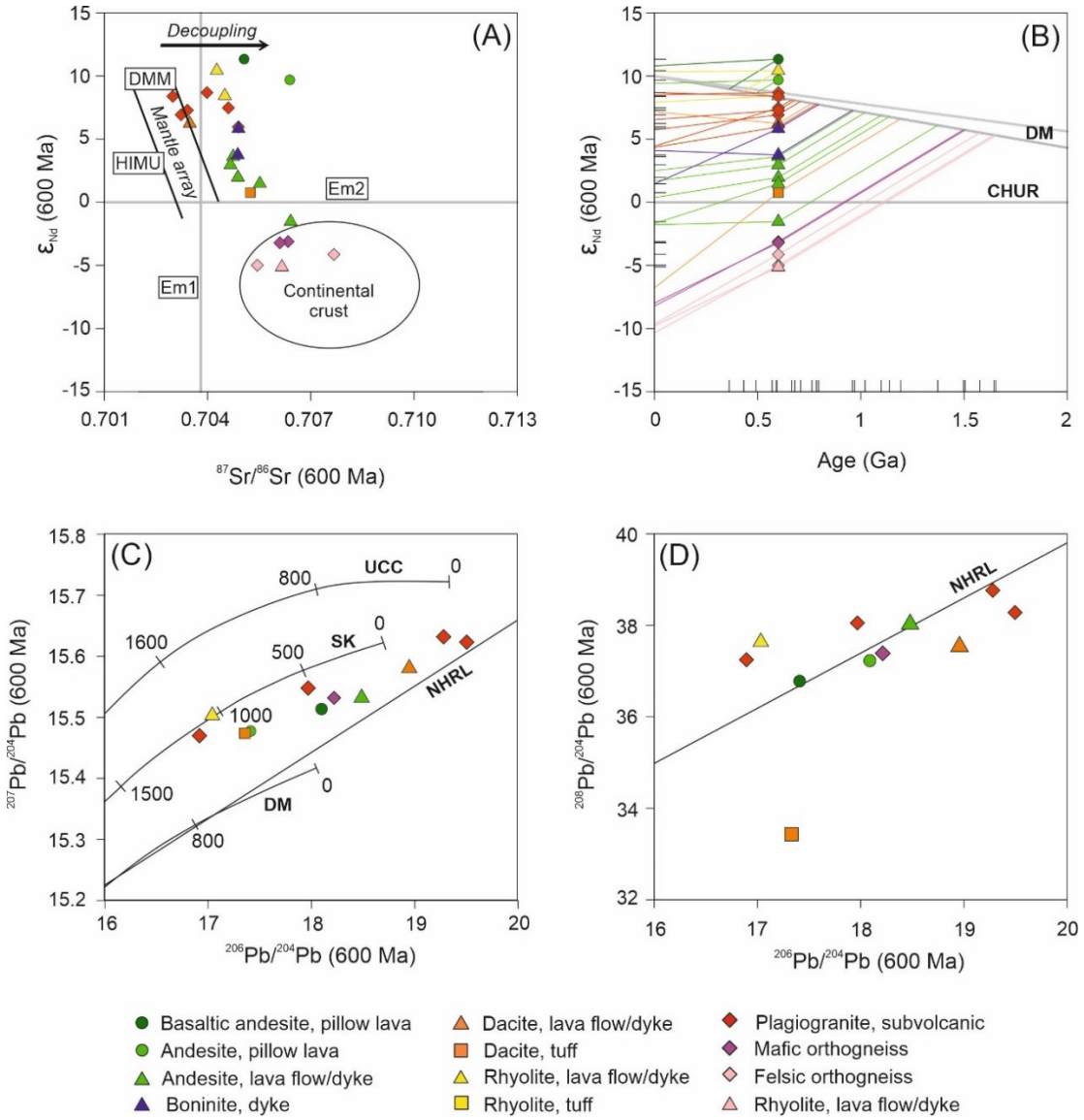

Figure 32. Sr-Nd-Pb isotopic compositions of the studied samples from the DVC. (A) ε_{Nd} vs $^{87}Sr/^{86}Sr$ (i) diagram with different geochemical reservoirs and a decoupling trend displayed. (B) ε_{Nd} vs. Age diagram showing curves of two-stage model ages (Liew and Hofmann, 1988). (C), (D) $^{207}Pb/^{204}Pb$ (i) vs. $^{206}Pb/^{204}Pb$ (i) and $^{208}Pb/^{204}Pb$ (i) vs. $^{206}Pb/^{204}Pb$ (i) diagrams, respectively, showing a wide scatter in $^{206}Pb/^{204}Pb$ (i) ratios likely caused by later disruption of the isotopic system, NHRL was calculated using equations from Rollinson (1993), curves of Upper continental crust (UCC) and Depleted mantle (DM) isotopic evolution are from Zartman and Doe (1981) and curve of two-stage lead isotope evolution (SK) is from Stacey and Kramers (1975).

7. Discussion

7.1. Metamorphism and its impact on the composition of the DVC

Three stages of metamorphism have been considered in the DVC: (1) hydrothermal alteration related to emplacement of primary magma and contact with seawater during late Neoproterozoic, (2) late-stage regional metamorphism connected most likely with early Variscan evolution of the Bohemian Massif while some imprint related to Cadomian orogenesis cannot be ruled out as well, and (3) contact metamorphism caused by the emplacement of Sázava suite of the Central Bohemian Plutonic Complex at ~350 Ma (Holub et al., 1997). Therefore, metamorphic overprint of the DVC is very complex and has been puzzling researchers for decades especially due to the very limited geochronological data obtained so far for the DVC magmatic rocks. For instance, regional metamorphism and deformation has been considered to be related to Cadomian orogeny but more detailed studies assigned the key deformational features to the Variscan tectonics (Rajlich et al., 1988; Žák et al., 2009, 2005a). Furthermore, basalts and basaltic andesites with elevated TiO_2 contents commonly found in DVC following tholeiitic trend were sometimes assigned to the Cadomian volcanic sequence while they rather represent dykes emplaced during Variscan magmatic activity, as inferred from their geochemical and petrographical similarity with dykes cross-cutting Paleozoic sequences in roof pendants of the Central Bohemian Plutonic Complex (Kachlík, 1992). This complexity resulted in several different interpretations concerning the metamorphic history of the DVC in the past (Fediukova and Fediuk, 2000; Röhlich, 1972; Waldhausrová, 1984).

Interaction with seawater is best preserved in the rocks that were least affected by the Variscan overprint. These are found in the Zbraslav area (Figure 6, Figure 8), which is in greater distance from the Central Bohemian Shear Zone. Andesitic pillow lavas from this area (sample 17CB01/1) retain almost undeformed shapes with radial cracks and they are composed mainly of fine-grained albite and chlorite (Figure 9), which is considered to originate by replacing primary minerals such as pyroxene and amphibole during the contact with seawater. Albite is most likely related to albitization of primary, more basic plagioclase (Mottl and Holland, 1978). Unfortunately, the primary modal composition is not preserved anywhere. Andesitic lava flow from this area (sample V-1098) retains spherulitic texture (Figure 10) that developed due to rapid undercooling during extrusion. These lavas also contain mainly albite and chlorite that replaced primary pyroxenes, amphiboles and presumably plagioclase. From the geochemical data, interaction with seawater can be well traced in all studied volcanic rocks through the marked Sr–Nd decoupled signature (radiogenic $^{87}Sr/^{86}Sr$ signatures at given ε_{Nd} values; Figure 32).

Early Variscan tectonics affected both, structure and mineralogy, in rocks near Central Bohemian Shear Zone (Kachlík, 1992; Žák et al., 2005a). Regional metamorphism in the DVC increases from NE, where plagiogranites are nearly unmetamorphosed and undeformed, to SW, where orthogneisses record greenschist to epidote amphibolite facies metamorphism and are considerably foliated. Regional metamorphism took place during early Variscan times; however, it is possible that the area was affected by similar metamorphic conditions during the Cadomian as well. In this respect, mineral that well-documents the extent of metamorphism is amphibole (Figure 35). In boninite, pyroxene is overgrown by actinolite, while in other rock types, actinolite is replacing chlorite or other mafic minerals that are not

preserved. In some rocks, epidote is found but distinguishing, whether it was formed as a result of Cadomian hydrothermal alteration or by later regional metamorphism is unfeasible.

The last stage of metamorphism that affected mostly the southeastern part of the DVC was contact metamorphism accompanied by extensive deformation. During the Variscan orogeny, Central Bohemian Plutonic Complex composed of several types of granitoids and subordinate gabbros was emplaced along Central Bohemian Shear Zone (Janoušek and Gerdes, 2003). Contact metamorphic aureole was investigated in detail in the NE part of the DVC by Röhlich and Morávek (Morávek and Röhlich, 1971; Röhlich, 1972). These authors proposed contact metamorphic zones based on petrographic study of epidote, chlorite, amphibole and pyroxene (Figure 33). Our study proves extensive HT–LP overprint of plagioclase and amphibole during metamorphism and assisted actinolite and albite breakdown to produce Ca-rich plagioclase but Ca-poor amphibole (Winter, 2010). This is documented by occurrence of andesine grains and hornblende-pargasite rims of amphibole grains in nearly all samples (Figure 9, Figure 17 andFigure 19). However, the innermost zone of thermal aureole is not documented since no samples were collected from this area. The deformation related to the emplacement of Sázava suite is characterized by large-scale folds preserved in the whole DVC and Štěchovice Group sediments and by Variscan cleavage preserved in the southeastern part (Jílové belt) and andesitic lava screens intercalating plagiogranite bodies (Figure 8) (Žák et al., 2005b). The Variscan granitic magmatism was also associated with Au–Ag–Pb–Zn–U mineralization in surrounding rocks (Škácha et al., 2009; Zachariáš et al., 2014, 2013) which might be also reflected by the largely perturbated Pb isotopic systematics (Figure 32).

The most complicated interpretation of metamorphic history regards the plagiogranite and equivalent volcanic rhyolite. Plagiogranite occurs not far from the Central Bohemian Shear Zone, but it was little affected by Variscan deformation due to its competent habitat. It contains mainly quartz, albite and chlorite. Since the albitization is not preserved in the Lečice Member shales intimately overlying DVC, Štěchovice Group or younger Paleozoic rocks, this process cannot be attributed to Variscan metamorphism. Albite is likely to form by hydrothermal alteration (Mottl and Holland, 1978) whereas its crystallization from primary melt is unlikely (Coleman and Donato, 1979; Winter, 2010). On the other hand, hydrothermal alteration usually creates alteration zones (Engvik et al., 2008) commonly reflected by the zonation of plagioclase crystals, which is neither present in the albites of DVC plagiogranite nor in albite phenocrysts of rhyolite lavas and tuffs (Figure 11). Furthermore, plagiogranite in the DVC forms large and homogenous intrusive bodies so the hydrothermal alteration would need to be very extensive, which is also quite unfavorable. In conclusion, chlorite might originate during some of the metamorphic stages by replacing amphibole or pyroxene (Winter, 2010), but albite is considered as a rather primary mineral.

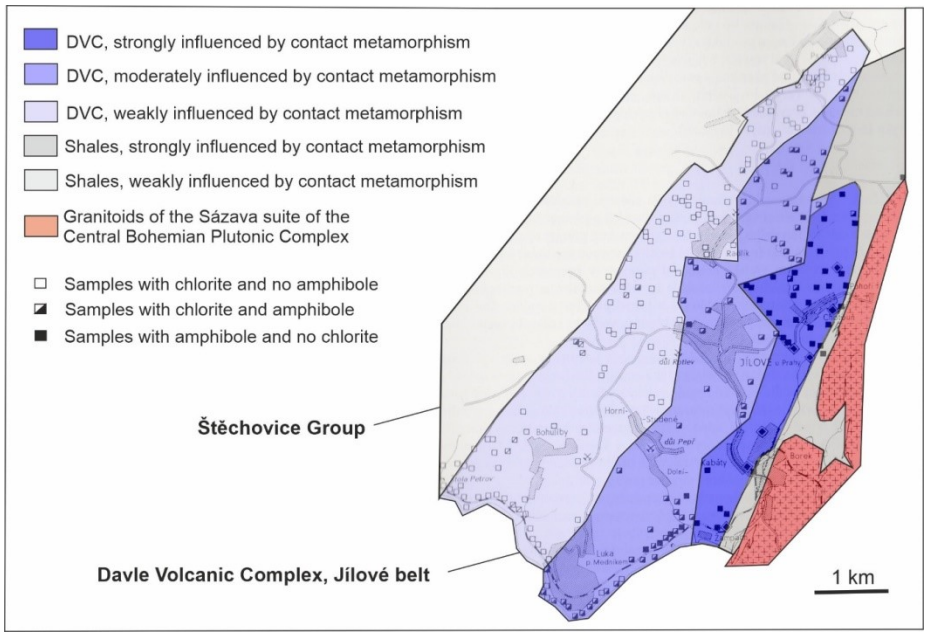

Figure 33. Zones of contact metamorphism in the northeastern part of the DVC, modified after Röhlich (1972).

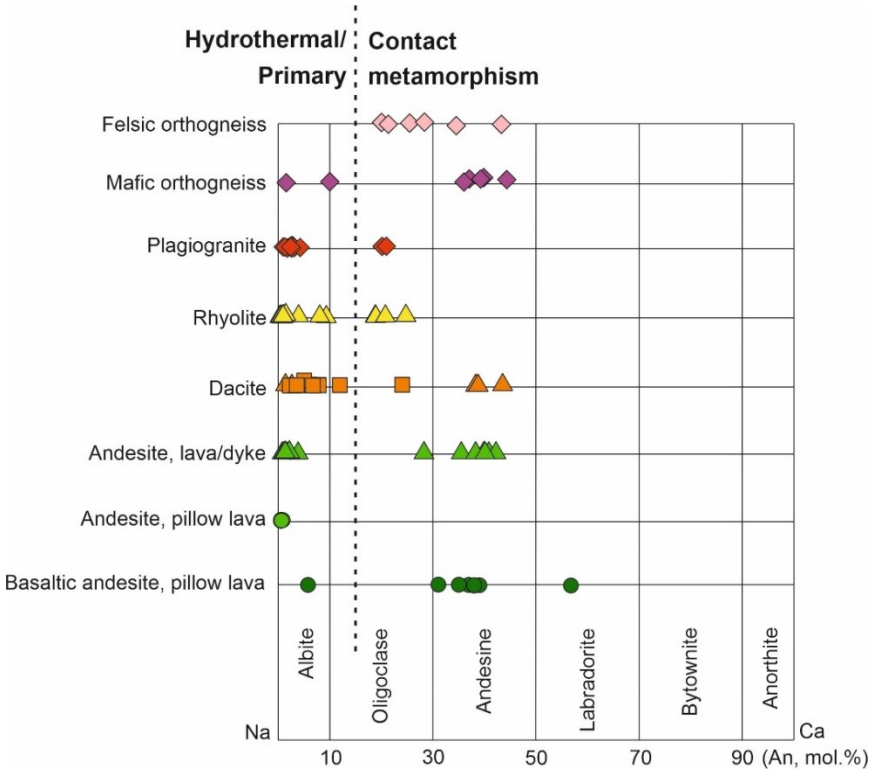

Figure 34. Relationship between composition of plagioclase from DVC magmatic rocks and metamorphic overprint.

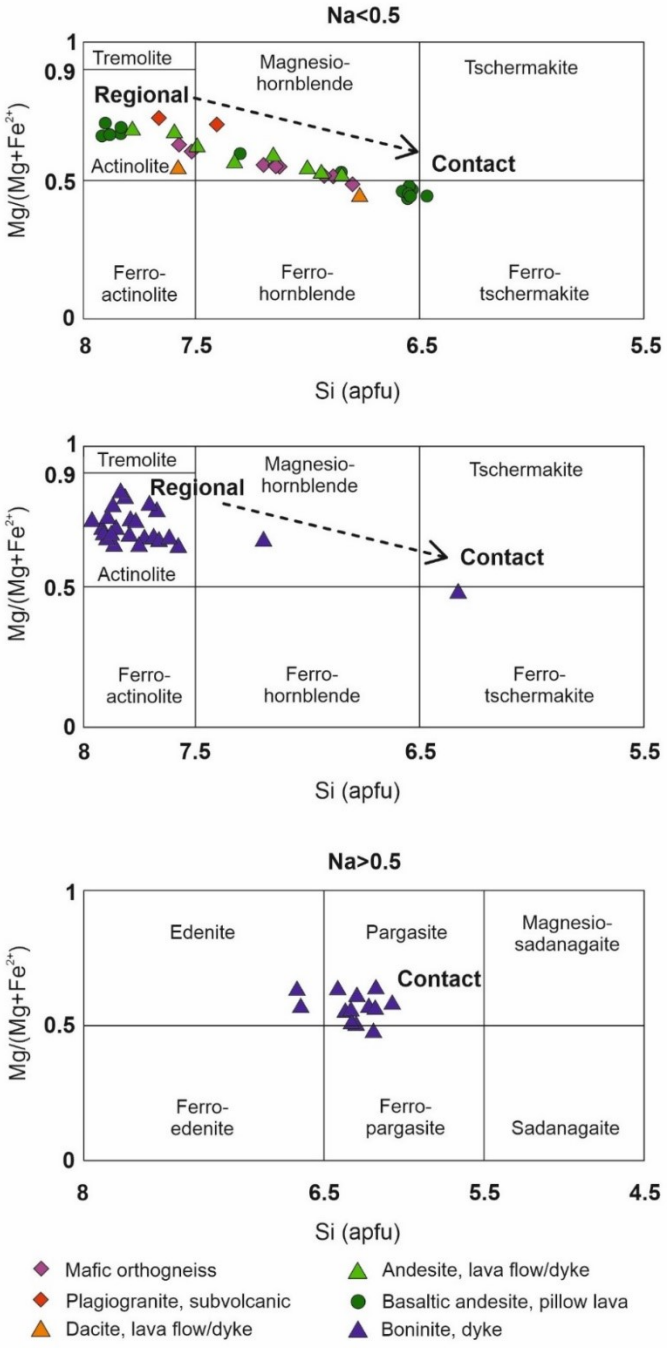

Figure 35. Relationship of amphibole composition and metamorphic evolution (regional vs. contact metamorphism) of the DVC.

7.2. Overview and new constrains on the temporal evolution of the DVC

In past years, a large number of geochronological data has been published from the TBU, but the prevalence of ages have been derived by U–Pb geochronology of sedimentary successions providing a rather decent insights into the timing of DVC volcanic activity (Ackerman et al., 2021; Drost et al., 2011; Hajná et al., 2019, 2018, 2017; Žák et al., 2020). The graywackes from the Blovice Accretionary Complex (BAC) contain large amounts of Neoproterozoic and Cambrian detrital zircons ranging from ~1000 to 500 Ma with a

prominent peak at around 600 Ma (Hajná et al., 2018, 2017) while the zircons extracted from the Štěchovice Group and Svrchnice Formation provided similar ages, yet containing youngest zircons with ages down to 545 Ma (Drost et al., 2011; Hajná et al., 2018; Sláma et al., 2008). Rhyolitic and trondhjemitic boulders from the Štěchovice Group and Svrchnice Formation conglomerates yield 585 ± 7 Ma and 568 ± 3 Ma (Dörr et al., 2002) and 610 ± 17 Ma (Sláma et al., 2008), respectively. However, the trondhjemite pebble has slightly different major and trace element compositions than DVC plagiogranite (this study) and therefore, its age cannot be unambiguously connected with DVC plagiogranite formation. Since the magmatic rocks of the DVC are commonly lacking zircons (this study), only one sample of rhyolitic tuff analyzed so far (Ackerman et al., 2021) marks the volcanic activity of DVC between 580 and 650 Ma with main cluster at around ~607 Ma and maximum depositional age at 583 +9/–15 Ma. As this tuffitic layer is directly overlain the black shales of the Lečice Member, the age of 583 +9/–15 Ma is therefore interpreted to mark the end of volcanic activity in at least the northern part of the DVC (Ackerman et al., 2021).

Our new data from the southern part of the DVC (Figure 6) provide ages of 608.3 ± 7.8 and 637 ± 11 Ma (Figure 20) for the mafic orthogneiss and for a rhyolitic dyke cross-cutting the felsic orthogneiss, respectively. These are in excellent agreement with previously published data from the BAC sedimentary rocks and further confirm that the maximum magmatic activity of DVC occurred between 580 and 650 Ma while it is possible that the rhyolitic dyke contain some population of older zircons from surrounding lithologies (J. Sláma, personal communication). The age of 637 ± 11 Ma can therefore be representative for the felsic orthogneiss protolith or older, yet unexposed lithologies.

However, many uncertainties related to the temporal evolution of DVC still remain. For example, the age of plagiogranite representing a prominent magmatic stage of DVC is still unknown as well as the temporal relationships between different rock types with special emphasis to andesitic rocks showing different $^{143}Nd/^{144}Nd$ signatures comparing to rest of DVC rocks (see below). It is also unclear, what was the source of sedimentary input into the arc-related basins if the volcanic activity of DVC ceased at around 580 Ma. It might been sourced from some scarcely exposed or unexposed parts of nowadays Bohemian Massif, most probably from the Moldanubian unit, where approximately 525 to 570 Ma old volcanic rocks have been found (Teipel et al., 2004). Nonetheless, the source for the sedimentary basins must have been geochemically evolved continental crust, since the Štěchovice Group siliciclastics exhibit negative ε_{Nd} values (Drost et al., 2007). The onset of subduction and related volcanic activity in the TBU remains uncertain as well. Sediments of the Štěchovice Group and BAC contain scarce zircons aging from ~1000 to 700 Ma, and it is uncertain, whether they were derived from local or distal sources and from which rock types. Therefore, the overall geotectonic environment of the TBU during this initial period remains deeply unexplored and will be target of complement investigation that will follow this thesis.

7.3. Petrogenesis of the DVC magmatic suite

The DVC consists of several different rock types with possible variable petrogenetic sources but there are some general characteristics typical for the whole suite. Based on geotectonic environment discrimination plots used, including AFM diagram, mantle-normalized spider plots, Nb/Yb vs Th/Yb (Pearce, 2014) and Zr vs TiO_2 (Pearce, 1982) plots

presented above, it can be concluded that all rocks of the DVC were derived from subduction-related environment. Therefore, their origin is intimately connected with processes related to arc formation and evolution. Notably, they follow calc-alkaline trend (Figure 23), exhibit negative Nb, Ta and Ti but positive Cs, Ba, U and Pb anomalies (Figure 26). Furthermore, REE characteristics and Yb_N vs $(La/Yb)_N$ plot (Martin, 1986), suggest that melts, from which the rocks of the DVC were generated, were not derived directly from the subducting plate but rather from the mantle wedge or crust source. Hereafter, the petrogenesis of the distinct rock types from the DVC is presented individually with respect to the observations derived from field work, petrography, bulk-rock composition and geochemical modelling applied.

7.3.1. Basaltic-andesitic and andesitic pillow lavas

Andesitic and basaltic andesitic pillow lavas are rather rare in the DVC, but they represent a remarkable rock member that can be intimately related to DVC parental magma compositions. Therefore, they are very important for understanding the processes leading to the origin of DVC. The pillow lavas are situated in the Zbraslav area (Figure 8) where they are accompanied by andesite dykes or lavas and overlain by felsic tuffs and in the Jílové belt. Their Sr–Nd isotopic characteristics indicate that they were derived from highly depleted mantle (Figure 32) while rather low Mg# of 35–36, Cr (7–62 ppm) and Ni concentrations (13–26 ppm) (Figure 29) suggest extensive fractionation of ferromagnesian minerals, especially olivine, orthopyroxene and clinopyroxene (Winter, 2010) from their parental melts. However, since chlorite and metamorphic amphibole are the only ferromagnesian minerals preserved in these rocks, primary mineral assemblage cannot be deciphered. Nevertheless, their island arc affinity is demonstrated by typical geochemical signatures recognized in geotectonic discrimination diagrams (Figure 23,Figure 30 andFigure 31) such as enrichment in LILE (Figure 31), while I note that Nb depletion is not as significant as in other samples (Figure 26). The absence of Nb depletion is difficult to explain. One possible explanation would be some contamination from the milling during sample processing but the other sample that show negative Nb anomalies were processed in the same way. Another possibility is less extensive fractionation of some Fe–Ti oxides from parental melt (e.g., rutile), however, this is not consistent with negative Ti anomalies observed (Figure 26). Therefore, the absence of negative Nb anomaly in these rocks remains unresolved. If the boninites are excluded (because they represent a later magmatic stage, see below), the pillow lavas are clearly the most primitive member of the volcanic suite due to their most depleted mantle isotopic characteristics, lowest SiO_2 and incompatible element contents and highest Al_2O_3, FeO_t, MnO, V, Co and Zn contents.

7.3.2. Andesite lavas and dykes

Massive andesitic lavas and dykes are one of the major constituents of the DVC. They are present in all exposed segments of the DVC and seem to be spatially associated with all rock types, including pillow lavas, felsic volcanics, plagiogranite, orthogneiss and boninite (Figure 5,Figure 6 Figure 7). However, their geochemical characteristics are unique showing largely variable ε_{Nd} signatures from –1.5 to +3.6 largely indicate derivation of the parental melts from a more complex source. Their rather low Th contents, U/Th and Ba/Th ratios argues for their derivation from subduction-related metasomatized mantle source without significant sediment or crustal melt contribution (Hawkesworth et al., 1997) (Figure 31). It is therefore possible that they formed from depleted mantle-derived melt assimilating an old but Th-depleted source, for example mafic lower crust. Moreover, they might represent multiple magma

pulses of yet unknown age which complicates the interpretation of their genesis until their exact age will be determined.

7.3.3. Dacitic lava and tuff

The analyzed samples of one dacitic lava and two dacitic tuffs show largely variable compositions. Sample 17CB29/1 of dacitic tuff from Pteč hill has anomalously high P_2O_5, Th and U concentrations and rather low alkali and Rb contents (Figure 22, Figure 29). Moreover, its La/Yb ratio is ~18, which is the highest of all samples. These characteristics together with primitive mantle Sr–Nd isotopic signature (Figure 32) set this sample a little apart from the rest of the suite. On the other hand, sample 17CB07/26 of dacitic tuff shows some geochemical features similar to the DVC orthogneiss like high K and Rb concentrations but also some distinctive features such as very low REE and low Th contents, which is more typical for the plagiogranite and rhyolite. All these aspects make very difficult to interpret the petrogenesis of dacitic tuff samples properly. Some characteristics, such as Na, K, Rb and Sr concentrations may be altered by seawater or metamorphic overprint but even the immobile elements provide unique signature which is hard to untangle. This is most likely related to tuffitic character of the rock that contains re-deposited mineral assemblages from different lava flows.

In contrast, the composition of dacitic lava sample 17CB27 correlates well with the rhyolite and plagiogranite in terms of its trace element and isotope characteristics (Figure 26, 27 and 32) suggesting similar petrogenesis. Highly depleted ε_{Nd} signature (+6.2, Figure 32) as well as depletion in Rb and Th (Figure 26), slightly negative Eu anomaly and La/Yb of ~2.5 (Figure 27) point to parental melt derivation from depleted mantle source and its close relationship to the plagiogranite and rhyolite discussed below.

7.3.4. Plagiogranite and rhyolite

Plagiogranite and rhyolite lavas/tuffs located in the northern part of DVC represent the most interesting and extraordinary rock types in the DVC especially due to their overall predominance in comparison to mafic members in the field. Here, I assumed that both types of rock represent the same magmatic pulse because of their conformable spatial occurrence and similar mineralogy and geochemistry (Figure 6, 26 and 32). The plagiogranite forms subvolcanic intrusions as documented by medium grained texture (Figure 12) and field relationships (Figure 8), whereas its extrusive equivalents formed rhyolitic domes, tuffs and pyroclastic breccias.

Oceanic plagiogranites were originally defined as granitic intrusions penetrating gabbro sequences in the ophiolite complexes (Coleman and Donato, 1979; Coleman and Peterman, 1975). These are characterized by high contents of CaO, Na_2O and Y and low contents of K_2O, FeO_t, Rb and Sr compared to continental granites (Coleman and Peterman, 1975). Numerous studies have proved that ophiolite complexes are usually formed at subduction related setting – back-arc basins or island arcs (Alabaster et al., 1982; Dilek and Furnes, 2011; Haase et al., 2016; Nguyen et al., 2019; Phelps and Avé Lallemant, 1980; Rollinson, 2009). This would be also the case of the DVC, although the DVC is not an ophiolite as it is completely missing ultramafic assemblage and having only a subordinate amount of mafic rock members.

In order to better constrain the source of plagiogranite magma and the processes that lead to plagiogranite magma generation, trace element geochemical modeling was performed.

Unfortunately, the obtained isotopic compositions cannot be used for modelling since obtained $^{87}Sr/^{86}Sr$ values have been largely modified by seawater alteration while wide range of Pb isotopic values (e.g., $^{206}Pb/^{204}Pb$ from 17 to 20; Figure 32) observed must be connected to large-scale perturbations related either to Variscan mineralization or sample processing (partial decomposition of rare Pb-rich minerals with highly radiogenic Pb isotopic signatures). The first assumption was that plagiogranite may represent a product of differentiation of mafic DVC pillow lavas. Therefore, several hypothetic scenarios were performed in this respect. On Figure 36, obtained fractional crystallization paths are presented on REE spider plots. Partial melting was also considered but, since partial melting and fractional crystallization result in similar REE patterns, only fractional crystallization model is displayed. Mean values of pillow lava were used as parental melt composition and the distribution coefficients related to fractionation of magma from Ersoy and Helvaci (2010) were applied. Pillow lava has similarly flat REE patterns as plagiogranite since supposed crystallizing minerals consisting of olivine, orthopyroxene, plagioclase and magnetite fractionate REEs evenly (only negative Eu anomaly is produced due to plagioclase fractionation). It can be recognized that to match the composition of plagiogranite, fractional crystallization of 20% olivine, 20% orthopyroxene, 50% plagioclase and 10% magnetite (Figure 36) would be necessary. However, such mineral assemblage crystallizing is very unlikely to develop in an island arc setting. Experimental study of Nandedkar et al. (2014) proved that in a water-saturated environment typical for subduction-related setting, clinopyroxene, plagioclase and possibly amphibole are the major fractionating minerals, whereas olivine and especially orthopyroxene are subordinate. Because MREEs and HREEs are compatible in clinopyroxene and amphibole during the fractionation of intermediate (and also felsic) magmas (Ersoy and Helvaci, 2010 and refs therein), removal of these elements into the crystallizing assemblage would result in their depletion in remaining melt. Therefore, generation of plagiogranite and equivalent volcanic rocks (rhyolite) through the fractional crystallization of DVC basaltic magmas is unlikely.

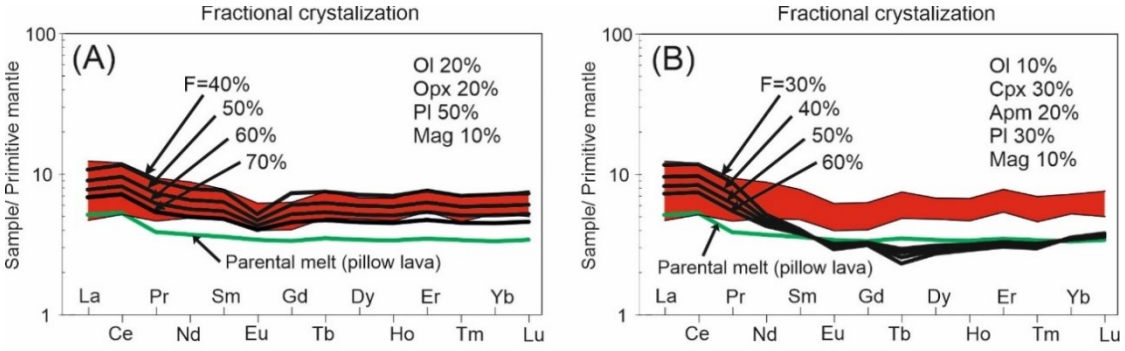

Figure 36. Results of geochemical modeling using mean DVC pillow lava composition to possibly explain the composition of plagiogranite. (A) and (B): REE spider diagrams normalized to primitive mantle (McDonough and Sun, 1995) with different proportion of crystalizing minerals. The red field stands for the range of plagiogranite composition and F stands for the fraction of remaining magma in percent. Ol=olivine, Opx=orthopyroxene, Cpx=clinopyroxene, Amp=amphibole, Pl=plagioclase, Mag=magnetite.

Since plagiogranite shows profoundly depleted mantle isotopic signatures (ε_{Nd} = 6.0–8.7), a model based on multistage fractionation of melt derived from an average depleted MORB mantle (DMM) reservoir of Workman and Hart (2005) was further performed (Figure 37). In the first step, DMM was used as source for partial melting with the modal composition of

constituent minerals (olivine, orthopyroxene and clinopyroxene) of the source as commonly reported (Winter, 2010) and distribution coefficients of Ersoy and Helvaci (2010) were applied. This approach would result in melts with REE distributions similar to MORB magmas (Sun et al., 1979), depleted in LREE with respect to HREE (La_N/Yb_N = ~0.3) overall depleted in incompatible elements (LILE) and Ti with respect to different partial melting degree (F) used.

In the second step, I used magma produced by 20% partial melting of DMM source as primary magma for subsequent fractional crystallization during its transport to the surface with proportion of 20% olivine, 10% orthopyroxene, 30% clinopyroxene, 30% plagioclase and 10% magnetite crystallized using distribution coefficients applicable to intermediate melts from Ersoy and Helvaci (2010). The selected minerals and their proportions were used to reflect theoretical mineral assemblage of Nandedkar et al. (2014) and because the fit of the modelled REE curves to that of plagiogranites. If amphibole was taken into account, MREEs became more depleted and thus, the resulting patterns became significantly U-shaped, which is not observed in the DVC plagiogranites. On the other hand, if more clinopyroxene and less orthopyroxene (or olivine) amounts were used, the resulting curves show higher LREEs and lower HREEs than observed in the DVC plagiogranites. The poor fit of the modelled patterns with respect to highly incompatible and especially fluid-mobile trace elements like Ba, U and Pb with that of DVC plagiogranite can be best explained by the fact, that the melt source has been variably enriched in these elements through a subduction-related metasomatism compared to DMM that occurs at different fluid-melt/rock ratios (Chin et al., 2018; Pearce and Peate, 1995; Workman and Hart, 2005).

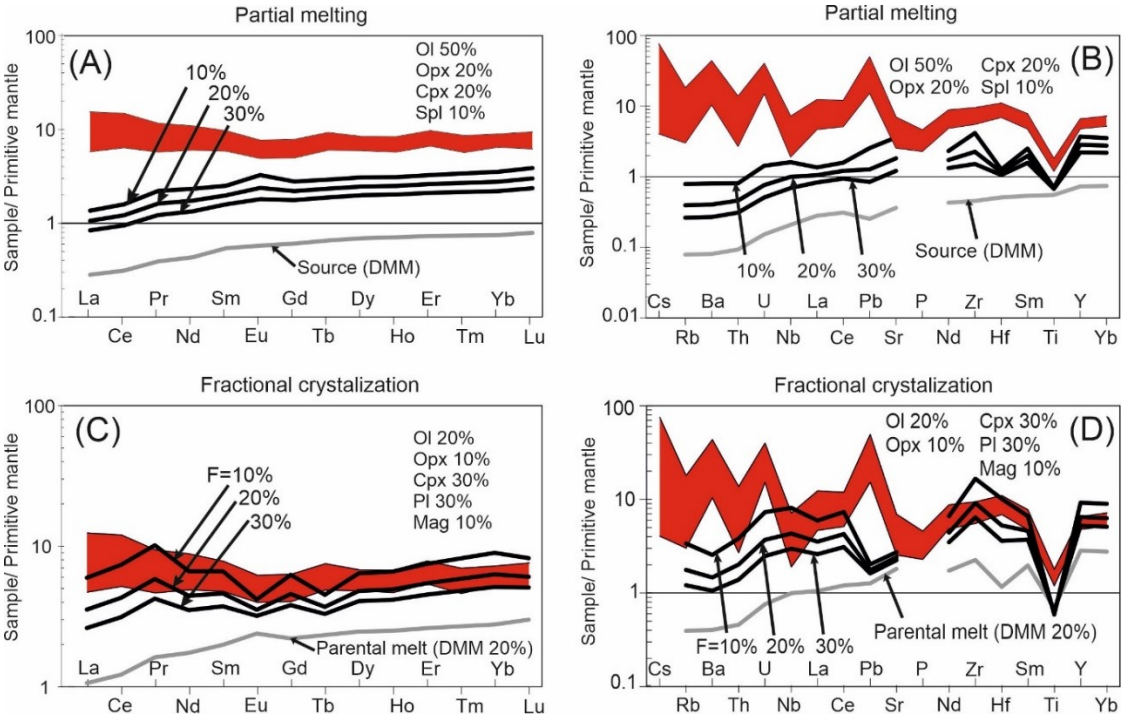

Figure 37. Results of geochemical modeling using average DMM (Workman and Hart, 2005) as source for partial melting in (A) and (B) and fractional crystallization of the melt produced by 20% partial melting of this source in (C) and (D). Presented spider diagrams are normalized to primitive mantle (McDonough and Sun, 1995), panels (A) and (C) show spider diagrams of REEs whereas panels (B) and (D) show other incompatible elements. The red

field stands for the range of plagiogranite composition and F in (C) and (D) stands for the fraction of remaining magma in percent. Ol=olivine, Opx=orthopyroxene, Cpx=clinopyroxene, Spl=spinel, Amp=amphibole, Pl=plagioclase, Mag=magnetite.

To conclude, the generation of the DVC plagiogranite seems to be explained by ~20% of melting of DMM-like source followed by variable degrees of fractional crystallization of this melt (or lower degrees of partial melting) with some incompatible element contents modifications related to subduction environment. These include enrichment in fluid-mobile elements like Cs, Rb, Ba, U and Pb (Pearce and Peate, 1995; Tatsumi, 2005; Zheng, 2019) and depletion in Nb and Ti due to sequester of these elements in Fe–Ti oxides (e.g., rutile) during melting of subducted slab (Foley et al., 2000) (Figure 26). Moreover, lower Th contents compared to Ba and U (Figure 31, Figure 37) can be attributed to the transfer of elements from the subducting plate to the melting column rather via aqueous fluids than silicious melt (Hawkesworth et al., 1997; Hermann et al., 2006; Pearce and Peate, 1995; Zheng, 2019).

Distinguishing, whether the final stage of differentiation was caused by fractional crystallization of mantle-derived magma or partial melting of thickened oceanic crust (e.g., lower crustal gabbros) is difficult for the several reasons: (1) the results of partial melting and fractional crystallization from geochemical modeling provide similar trace element patterns, (2) the plagiogranite from the DVC form large plutonic bodies intruding into the volcanic sequence (Figure 8), which can be attributed to both processes (Atherton and Petford, 1993; Nguyen et al., 2019; Rudnev et al., 2020), (3) their original relationships with surrounding rocks are hindered by Variscan tectonic and metamorphic overprint, (4) they cannot be with confidence linked to one differentiation series with mafic rocks of the DVC (pillow lavas, andesites, dacites or mafic orthogneisses), since each rock type is geochemically somehow distinct from the others. This is supported also by results of geochemical modelling (Figure 36), (5) complete reconstruction of differentiation series is difficult because the predominance of SiO_2-rich endmembers while intermediate rock types are largely missing (Figure 21) with only one reliable dacite lava sample (17CB27), (6) titanium content is widely used for discrimination of the two processes, where higher TiO_2 content predicts fractional crystallization (Koepke et al., 2007), but this cannot be used for arc-related magmas, since these magmas follow calc-alkaline trend and therefore are TiO_2 depleted regardless of the final stage of silicious magma generation (Foley et al., 2000; Nguyen et al., 2019), (7) higher Na_2O contents are usually related to partial melting at increasing depths (Atherton and Petford, 1993; Castillo, 2012), but they can be also acquired by a high degree of fractional crystallization (Nandedkar et al., 2014), and (8) highly positive ε_{Nd} values, characteristic for DVC silicious rocks (Figure 32), can reflect either derivation from depleted mantle or depleted oceanic crust (Nguyen et al., 2019; Rudnev et al., 2020).

Nevertheless, fractional crystallization is preferred here for the generation of the DVC plagiogranite and rhyolite for the following reasons. Although I conclude that deciphering the fractionation path for the rock suite with such limited SiO_2 contents variation is difficult, the REE concentrations for individual rock types exhibit some distinct features. On spider diagram, they show flat distributions (Figure 27) with no relationship between LREE with increasing SiO_2 but highly positive co-variation for HREE with increasing SiO_2 (Figure 28). These features are typical for fractional crystallization of parental mafic melts to originate plagiogranitic melts whereas it is distinct from dehydration melting origin (Brophy, 2008; Pu et al., 2014). Extremely high SiO_2 contents, so characteristic for the DVC plagiogranite and rhyolite can be also explained by fractional crystallization as Fe–Ti removal from the melt

will strongly enrich the residual melt in SiO_2 leading to a generation of SiO_2-rich melts (> 70 wt.%) despite their mantle origin (Chen et al., 2019; Nandedkar et al., 2014).

7.3.5. Orthogneiss and related rhyolite dyke

Mafic and felsic orthogneiss and related rhyolite dyke sampled in the southern section of the DVC (Figure 6) show very contrasting geochemical characteristics from the rest of the magmatic rocks appeared to the north. Notably, they have more elevated contents of incompatible elements like K, Rb, Ba, Th, U, Zr and LREE and lower contents of TiO_2, HREE (Figure 26) and Na_2O (Figure 22). When plotted in the discrimination diagram of O'Connor (1965), they fall into the field of tonalite and granodiorite (Figure 25). On geotectonic discrimination diagram by Pearce (2014), they fall into the field of continental arcs (Figure 30). All these characteristics are well in agreement with their negative ε_{Nd} signatures (down to –5.1; Figure 32) that argue for high degree of assimilation of crustal material or even direct derivation from continental crust.

These observations were tested by geochemical modeling. Assimilation-fractional crystallization (AFC) process was used taking minimum element concentrations of DVC andesite as primary magma (Figure 38) and the composition of bulk continental crust from Rudnick and Gao (2014) as the assimilant with r value (r = rate of assimilation to fractional crystallization) set to 0.5. Distribution coefficients applicable to evolution of intermediate magmas from Ersoy and Helvaci (2010) were used with 10% Orthopyroxene, 10% clinopyroxene, 20% amphibole, 50% plagioclase, 9% magnetite and 1% apatite as fractionating mineral assemblage. Using this model, REE as well as other incompatible trace element patterns of the orthogneisses nicely fit to the modelled patterns produced by 20–40% fractional crystallization of the used parental melt (F = 60–80%).

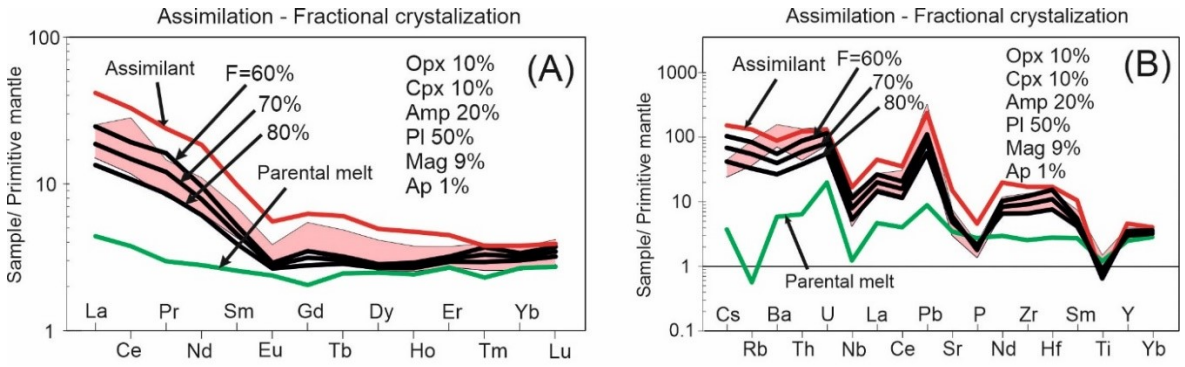

Figure 38. Results of geochemical modeling using average minimum values of andesite as primary magma for assimilation - fractional crystallization model. Presented spider diagrams, (A) for REEs and (B) for incompatible trace elements, are normalized to primitive mantle (W. F. McDonough and Sun, 1995). The pink field stands for the range of orthogneiss composition while F stands for the fraction of remaining magma (%). Opx=orthopyroxene, Cpx=clinopyroxene, Amp=amphibole, Pl=plagioclase, Mag=magnetite, Ap=apatite.

7.3.6. Boninite

Boninites are peculiar magmatic rocks occurring in some island arcs and fore- and back-arc basins (Beccaluva and Serri, 1988; Pearce and Reagan, 2019). They are defined by the

following major element characteristics: SiO_2 > 52 wt.%, MgO > 8 wt.% and TiO_2 < 0.5 wt.% (Le Maitre et al., 2002). Their derivation have been generally attributed to high degrees of melting (> 15%) of previously depleted mantle protolith at rather low pressures (< 15 kbar) and high temperatures (> 1250 °C) enriched in LREE, Zr, Ba, K, Rb and H_2O (Beccaluva and Serri, 1988; Crawford et al., 1989; Ishikawa et al., 2002; Pearce and Reagan, 2019; Wood and Turner, 2009).

The boninites in the DVC form dykes penetrating the whole volcanic sequence (V. Kachlík, personal communication). However, it is difficult to assure any field relationship interpretations since they are almost undistinguishable from the andesites in the field. Nevertheless, they can be distinguished by major element composition and especially from the petrographic observation. Overall, their composition can be characterized by enrichment in LILE (Cs, Ba, Th, U and Pb) and depletion in HFSE (Nb and Ti) (Figure 26), both features characteristic for arc-related magmas, but also enrichment in compatible elements (Cr, Co, Ni and Zn) (Figure 29) and positive ε_{Nd} values (Figure 32) related to high degree melting of depleted oceanic mantle. Unfortunately, in the studied DVC suite, the primary mineral assemblage is hard to recover since most of the ferromagnesian minerals are replaced by metamorphic amphiboles. Yet, the original ferromagnesian mineral is clinopyroxene with composition of diopside occurring as phenocrysts and diopside-hedenbergite dispersed in the rock matrix (Figure 14, Figure 18). All these characteristics are in agreement with previously published larger dataset of boninites from the Jílové belt (Fediuk, 1992).

7.4. Davle volcanic arc evolution and implications for the late Neoproterozoic–Cambrian evolution of Teplá-Barrandian unit

Based on above presented data, two sections that seem to represent different geotectonic environments can be distinguished in the DVC – (1) the northern with basaltic andesite and andesite pillow lavas, andesite lavas and dykes, plagiogranite, dacite and rhyolite lavas with their equivalent tuffs and (2) southern dominated by mafic and felsic orthogneiss and associated rhyolitic and andesitic lavas and dykes. Unfortunately, the stratigraphic and geotectonic relationships of these two contrasting lithologies are unclear as they are separated by transform faults intersecting the DVC and their boundary is intruded by the Central Bohemian Plutonic Complex (Figure 40). Nevertheless, constraining the new data I obtained within the framework of this study, I propose a new preliminary geotectonic model that might explains the late Neoproterozoic–Cambrian evolution of the DVC (Figure 39, Figure 40).

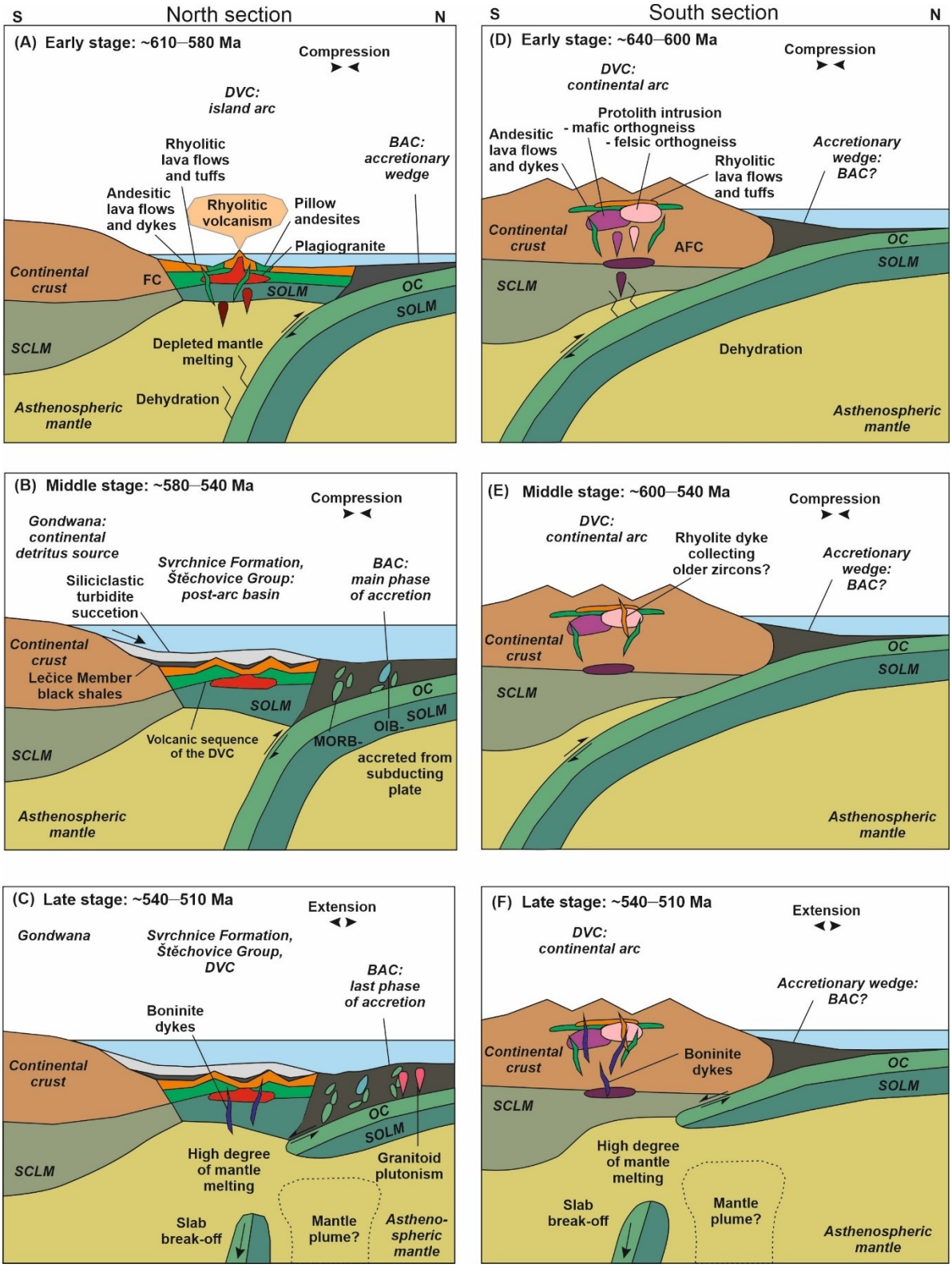

Figure 39. A sketch of the new geotectonic model proposed for the DVC evolution on the northern margin of Gondwana taking into account previous assumptions on the DVC evolution (Ackerman et al., 2021; Drost et al., 2011; Hajná et al., 2018, and refs. therein), not to scale. FC = fractional crystallization, AFC = assimilation–fractional crystallization, SCLM = subcontinental lithospheric mantle, OC = oceanic crust, SOLM = suboceanic lithospheric mantle

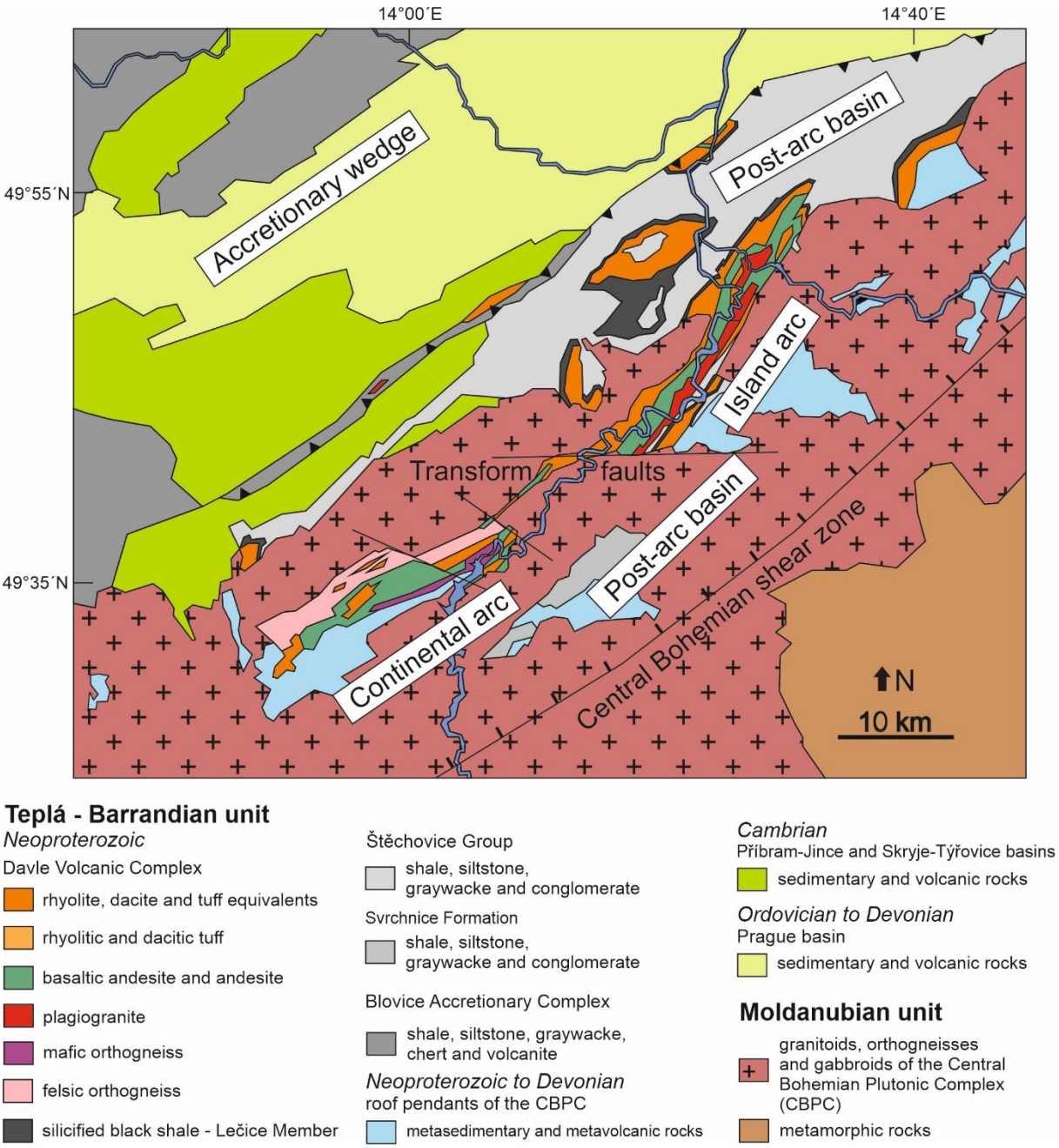

Figure 40. Geologic map of the DVC presenting the new geotectonic model, see text for details.

In this newly proposed model, the southern DVC section represents a continental magmatic arc formed on an active northern margin of Gondwana (Figure 39). Magmatic activity is represented by large volumes of plutonic and volcanic rocks metamorphosed during the Variscan orogeny (Žák et al., 2009, 2005a) including mafic and felsic orthogneiss and associated rhyolite dykes, andesites (e.g., sample V-212), dacitic tuff (e.g., sample 17CB29/1) and possibly boninite (e.g., samples M2 and K-8; Figure 6, Figure 40). New geochronological data suggest that the continental arc was active at least between ~640 and 600 Ma. A geotectonic setting of continental arc has been described from several Cadomian terranes in Europe (Abati et al., 2018; Chantraine et al., 2001; Errami et al., 2021; Linnemann et al., 2014; Soejono et al., 2017), and corroborated by some authors for the DVC as well (Drost et al., 2011; Fiala et al., 2014). Since the sedimentary and volcanic rocks in the Mirovice roof

pendant (Figure 6, Figure 7) that is adjacent to the south section of the DVC are poorly constrained, it is possible that they represent lithologies extruded or deposited on the northern margin of Gondwana during or after the main volcanic and plutonic activity in the southern DVC which needs to be confirmed or rejected by subsequent studies.

By contrast, the northern DVC section represents a magmatic arc formed in an intra-oceanic setting (island arc; oceanic vs. oceanic plate convergence). This is documented by subaqueous character of effusive rocks (pillow lavas) (Fiala, 1987) and Lečice Member black shales deposited intimately on the waning arc (Ackerman et al., 2021; Figure 8), highly radiogenic ε_{Nd} values of the arc volcanic members (Figure 32), Sr–Nd decoupled signature reflecting seawater alteration, low Th contents (Figure 26, Figure 31), flat REE patterns (Figure 27) typical for volcanic rocks derived from depleted mantle and geotectonic discrimination diagrams (Figure 30). Island arc geotectonic setting has been also reported from some other European Cadomian terranes (Chantraine et al., 2001; Errami et al., 2021) and it is also in agreement with most of the previous studies from the TBU (Ackerman et al., 2021; Hajná et al., 2011; Sláma et al., 2008). Nevertheless, after the termination of the DVC volcanic activity at around ~580 Ma (Ackerman et al., 2021), the area had to be close to Gondwana mainland since the overlying turbiditic sedimentary sequence of the Štěchovice Group exhibit negative ε_{Nd} compositions (–7.2 to –5.5) indicating derivation from evolved continental crust (Drost et al., 2011, 2007). The end of Cadomian accretionary processes in the TBU is linked with transition from compressional to extensional regime as documented by sedimentation in Cambrian wedge-top basins at ~515–506 Ma (Hajná et al., 2018) and granitic plutonism in the western part of the TBU at ~524–504 Ma (Dörr et al., 2002; Drost et al., 2011 and references therein).

However, there are several features that are characteristic for both sections, such as occurrence of andesitic dykes and lavas with largely variable, but overlapping geochemical characteristics and presence of boninite dykes. As the latter intersect lower Cambrian sequences present in the roof pendants of the Central Bohemian Plutonic Complex (Kachlík, 1992; Kachlík et al., 1999), they are contemporaneous with the end of Cadomian orogenesis in the TBU and therefore, document the change in geotectonic regime from convergence (active margin) to extension (Hajná et al., 2018). Several scenarios explaining the overturn in geotectonic regime have been proposed (Hajná et al., 2018 and refs. therein), the most recent one include trench-plume collision leading to slab break-off (Ackerman et al., 2019). This would explain the increased temperature in the mantle wedge required to generate boninitic melts (Pearce and Reagan, 2019; Sobolev and Danyushevsky, 1994). It is also important to note that boninite was also recently described from the Nové Město unit in the northeastern Bohemian Massif (Ilnicki et al., 2020) which was appointed as a back-arc basin adjacent to the TBU. However, these connections must be regarded with special caution (V. Kachlík, personal communication). The relationship of andesites to the rest of the volcanic suite is unclear. It has been assumed that, together with the rhyolites and plagiogranites, they represent the main phase of magmatic activity (Hajná et al., 2011; Röhlich, 1998, 1972). However, their highly variable ε_{Nd} values revealed in this study (Figure 32) that are in contrast to radiogenic ε_{Nd} values for surrounding volcanic/plutonic rocks of the DVC, indicate that they must be derived from a different source with enhanced continental crust input. Moreover, geochemically similar andesites are found in both sections (north and south) whereas plagiogranite and related Na-rich rhyolite is found only in the northern section (Figure 6). The andesites might therefore represent either multiple magmatic pulses including early volcanic activity intruded by plagiogranites and caped by rhyolitic pyroclastics or younger (Cambrian?) dykes similarly to the boninites. Therefore, a further detailed study involving more andesite samples from the southern section of DVC is required to solve this controversy.

The newly proposed preliminary model for the Neoproterozoic–Cambrian evolution of the DVC may be the most favorable at present state of knowledge, though certainly not the only one. Since we have not acquired precise geochronological data from the northern section and there are no geochronological or geochemical data from the sedimentary sequences of the Mirovice roof pendant that stratigraphically overlie the southern section, the temporal relationships of the northern and southern sections are still vague. Furthermore, both sections contain some rocks of similar geochemical characteristics (andesite and boninite) that may be considered as spatially related while their different compositions (orthogneiss vs. plagiogranite) may be explained by temporal changes in subduction mode and magma sources. Hence, the contrasting sections may represent just a different erosion level of the same magmatic arc and additional research is needed to shed more light into this controversy.

8. Conclusions

In this study, a variety of methods including fieldwork, optical microscopy, rock-forming mineral microanalysis, major and trace element analysis, Sr–Nd–Pb isotopic systematics and U–Pb zircon geochronology was applied to explain the Neoproterozoic evolution of the Davle Volcanic Complex (DVC), resulting in the following conclusions:

(1) The DVC consists of Neoproterozoic to Cambrian volcanic, subvolcanic and plutonic rocks comprising basaltic andesite and andesite pillow lava, andesitic lava and dykes, dacitic and rhyolitic lava and tuff, plagiogranite, mafic and felsic orthogneiss and boninite dykes metamorphosed to various extent. All studied rocks are enriched in LILE, depleted in HFSE and follow calc-alkaline trend suggesting their subduction affinity.

(2) Basaltic rocks and rocks following tholeiitic trend previously described from the DVC (Waldhausrová, 1984) are newly ascribed to younger, possibly Variscan, events since they penetrate Paleozoic successions in neighboring basins (Kachlík, 1992).

(3) At least three-stage metamorphism of the DVC magmatic rocks must be considered: a seawater alteration due to extrusion on the sea floor during Neoproterozoic, regional metamorphism related to Variscan orogeny increasing to the southeast and contact metamorphism due to intrusion of the Variscan Central Bohemian Plutonic Complex close to the SE contact of the DVC.

(4) Mafic and felsic volcanic and subvolcanic rocks including peculiar silicious Na-rich plagiogranite and rhyolite with primary albite grains from the northern section of the DVC exhibit highly radiogenic ε_{Nd} values (+6 to +11.3) characteristic for derivation from depleted mantle while their trace element signatures are characteristic for a subduction-related setting. These findings also provide insights into the origin of island arc-related silicious rocks from the mafic mantle melts.

(5) Mafic and felsic orthogneiss with related rhyolite dyke from the southern section yield negative ε_{Nd} values (–5.1 to –3.1) ultimately connected with their derivation either through direct melting of continental crust or containing high proportion of such endmember. Together with their trace element signatures, they can be best interpreted to originate at active continental margin setting. Two samples, mafic orthogneiss and rhyolite dyke, were dated using ICP-MS U–Pb zircon geochronology and yield ages of 608 ± 8 Ma and 637 ± 11 Ma, respectively, providing evidence for Cadomian age.

(6) Andesites found in both sections exhibit ε_{Nd} values from –1.5 to +3.6 indicating their derivation through complex processes that involves variable contribution of continental crust member.

(7) The volcanic suite and adjacent sedimentary basins are penetrated by boninite dykes with ε_{Nd} values from +3.7 to +5.8. Likely, these rocks formed during high degree melting of depleted mantle source related to slab break-off and input of hot mantle source.

(8) Newly introduced preliminary geotectonic model for the Neoproterozoic–Cambrian evolution of the DVC suggests that the northern (island arc) and southern (continental arc) sections of the DVC were spatially separated segments.

9. References

Abati, J., Arenas, R., Fernández, R.D., Albert, R., Gerdes, A., 2018. Combined zircon U–Pb and Lu–Hf isotopes study of magmatism and high-P metamorphism of the basal allochthonous units in the SW Iberian Massif (Ossa-Morena complex). Lithos.

Ackerman, L., Hajná, J., Žák, J., Erban, V., Sláma, J., Polák, L., Kachlík, V., Strnad, L., Trubač, J., 2019. Architecture and composition of ocean floor subducted beneath northern Gondwana during Neoproterozoic to Cambrian : A palinspastic reconstruction based on Ocean Plate Stratigraphy (OPS). Gondwana Res. 76, 21.

Ackerman, L., Pašava, J., Žák, J., Žák, K., Kachlík, V., Šebek, O., Trubač, J., Svojtka, M., Veselovský, F., Strnad, L., Santolík, V., 2021. Arc-related Black Shales as Sedimentary Archives of Sea-level Fluctuations and Plate Tectonics During the Late Neoproterozoic: An Example from the Bohemian Massif. Mar. Pet. Geol. 123.

Alabaster, T., Pearce, J.A., Malpas, J., 1982. The volcanic stratigraphy and petrogenesis of the Oman ophiolite complex. Contrib. to Mineral. Petrol. 81, 168–183.

Arakawa, Y., 1998. Sr – Nd isotopic and chemical characteristics of the silicic magma reservoir of the Aira pyroclastic eruption , southern Kyushu , Japan 179–194.

Arakawa, Y., Kurosawa, M., Takahashi, K., Kobayashi, Y., Tsukui, M., Amakawa, H., 1998. Sr-Nd isotopic and chemical characteristics of the silicic magma reservoir of the Aira pyroclastic eruption, southern Kyushu, Japan. J. Volcanol. Geotherm. Res.

Atherton, M.P., Petford, N., 1993. Generation of sodium rich magmas from newly underplated basaltic crust. Nat. 333, 816–824.

Balintoni, I., Balica, C., 2016. Peri-Amazonian provenance of the Euxinic Craton components in Dobrogea and of the North Dobrogean Orogen components (Romania): A detrital zircon study. Precambrian Res. 278, 34–51.

Bao, Z.., Bai, Z.H., Wang, Q., Xiong, X.L., Qiao, Y.L., Wyman, D.A., Zhao, Z.H., 2007. Underplating-related adakites in Xinjiang Tianshan, China. Lithos 102, 374–391.

Barnes, S.J., Roeder, P.L., 2001. The range of spinel compositions in terrestrial mafic and ultramafic rocks. J. Petrol. 42, 2279–2302.

Beard, J.S., 1986. Characteristic mineralogy of arc-related cumulate gabbros : Implications for the tectonic setting of gabbroiic plutons and for andesite genesis. Geology 14, 848–851.

Beccaluva, L., Serri, G., 1988. Boninitic and low-Ti subduction-related lavas from intraoceanic arc-backarc systems and low-Ti ophiolites: a reappraisal of their petrogenesis and original tectonic setting. Tectonophysics 146, 291–315.

Bénard, A., Arculus, R.J., Nebel, O., Ionov, D.A., McAlpine, S.R.B., 2017. Silica-enriched mantle sources of subalkaline picrite-boninite-andesite island arc magmas. Geochim. Cosmochim. Acta 199, 287–303.

Bodinier, J.L., Godard, M., 2003. Orogenic, Ophiolitic, and Abyssal Peridotites, in: Holland, H.D., Turekian, K.K. (Eds.), Treatise on Geochemistry. p. 568.

Brophy, J.G., 2008. A study of rare earth element (REE)-SiO2 variations in felsic liquids generated by basalt fractionation and amphibolite melting: A potential test for discriminating between the two different processes. Contrib. to Mineral. Petrol. 156, 337–357.

Castillo, P.R., 2012. Adakite petrogenesis. Lithos 134–135, 304–316.

Cháb, J., Pelc, Z., 1968. Lithology of Upper Proterozoic in the NW limb of the Barrandian area. Krystalinikum 6, 141–167.

Chaib, L., Lahna, A.A., Admou, H., Youbi, N., Moume, W. El, Celso, C., Tassinari, G., Angelo, M., Basei, S., Sato, K., Marzoli, A., Bodinier, J., Gärtner, A., Boumehdi, M.A., Bensalah, M.K., Soulaimani, A., Hefferan, K., Maacha, L., Bajddi, A., 2021. Geochemistry and Geochronology of the Neoproterozoic Backarc Basin Khzama Ophiolite (Anti-Atlas Mountains, Morocco): Tectonomagmatic Implications. Minerals 11.

Chantraine, J., Egal, E., Thiéblemont, D., Le Goff, E., Guerrot, C., Ballèvre, M., Guennoc, P., 2001. The Cadomian active margin (North Armorican Massif, France): A segment of the North Atlantic Panafrican belt. Tectonophysics 331, 1–18.

Chen, Y., Niu, Y., Al, C.E.T., 2019. Petrogenesis of ODP Hole 735B (Leg 176) Oceanic Plagiogranite : Partial Melting of Gabbros or Advanced Extent of Fractional Crystallization ?

Geochemistry , Geophysics , Geosystems 2717–2732.
Chin, E.J., Shimizu, K., Bybee, G.M., Erdman, M.E., 2018. On the development of the calc-alkaline and tholeiitic magma series: A deep crustal cumulate perspective. Earth Planet. Sci. Lett. 482, 277–287.
Coleman, R.G., Donato, M.M., 1979. Oceanic plagiogranite revisited. Dev. Petrol. 6, 149–168.
Coleman, R.G., Peterman, Z.E., 1975. Oceanic plagiogranite. J. Geophys. Res. 80, 1099–1108.
Collett, S., Štípská, P., Schulmann, K., Míková, J., Kröner, A., 2021. Tectonic significance of the Variscan suture between Brunovistulia and the Bohemian Massif. Geol. Soc. London, Spec. Publ. 22.
Crawford, A.J., Falloon, T.J., Green, D.H., 1989. Classification, petrogenesis and tectonic setting of boninites, in: Boninites: And Related Rocks. pp. 1–49.
Dalziel, I.W.D., 1997. Neoproterozoic-Paleozoic geography and tectonics: Review, hypothesis, environmental speculation. Bull. Geol. Soc. Am. 109, 16–42.
Deer, W.A., Howie, R.A., Zussman, J., 1992. An Introduction to the Rock Forming Minerals.
Defant, M.J., Drummond, M.S., 1990. Derivation of some modern arc magmas by melting of young subducted lithosphere. Nature 347, 662–665.
Dempírová, L., 2010. Evaluation of SiO2, Na2O, MgO, K2O determinations in silicate samples by z-score obtained from nineteen interlaboratory tests. Geosci. Res. Reports 2009 323–326.
DePaolo, D.J., 1981. Trace element and isotopic effects of combined wallrock assimilation and fractional crystallization. Earth Planet. Sci. Lett. 53, 189–202.
Didier, J., Duthou, J.L., Lameyre, J., 1982. Mantle and crustal granites: Genetic classification of orogenic granites and the nature of their enclaves. J. Volcanol. Geotherm. Res. 14, 125–132.
Dilek, Y., Furnes, H., 2011. Ophiolite genesis and global tectonics : Geochemical and tectonic fingerprinting of ancient oceanic lithosphere 387–411.
Dilek, Y., Thy, P., 2009. Island arc tholeiite to boninitic melt evolution of the Cretaceous Kizildag (Turkey) ophiolite: Model for multi-stage early arc-forearc magmatism in Tethyan subduction factories. Lithos 113, 68–87.
Dörr, W., Zulauf, G., Fiala, J., Franke, W., Vejnar, Z., 2002. Neoproterozoic to Early Cambrian history of an active plate margin in the Teplá-Barrandian unit - A correlation of U-Pb isotopic-dilution-TIMS ages (Bohemia, Czech Republic). Tectonophysics 352, 65–85.
Drost, K., 2008. Sources and geotectonic setting of Late Neoproterozoic – Early Palaeozoic volcano-sedimentary successions of the Teplá-Barrandian unit (Bohemian Massif): Evidence from petrographical, geochemical, and isotope analyses Petrographische,. Geol. Saxonica 54, 1–168.
Drost, K., Gerdes, A., Jeffries, T., Linnemann, U., Storey, C., 2011. Provenance of Neoproterozoic and early Paleozoic siliciclastic rocks of the Teplá-Barrandian unit (Bohemian Massif): Evidence from U-Pb detrital zircon ages. Gondwana Res. 19, 213–231.
Drost, K., Romer, R.L., Linnemann, U., Fatka, O., Kraft, P., Marek, J., 2007. Nd-Sr-Pb isotopic signatures of neoproterozoic - Early paleozoic siliciclastic rocks in response to changing geotectonic regimes: A case study from the Barrandian area (Bohemian Massif, Czech Republic). Spec. Pap. Geol. Soc. Am. 423, 191–208.
Dunstan, L.P., Gramlich, J.W., Barnes, I.L., Purdy, W.C., 1980. Absolute Isotopic Abundance and the Atomic Weight of a Reference Sample of Thallium. J. Res. Natl. Bur. Stand. (1934). 85, 1–10.
Ebinger, C.J., Sleep, N.H., 1998. Cenozoic magmatism throughout east Africa resulting from impact of a single plume. Nature 395, 788–791.
Elliott, T., Plank, T., Zindler, A., White, W., Bourdon, B., 1997. Element transport from slab to volcanic front at the Mariana arc. J. Geophys. Res. 102, 14,991-15,018.
Engvik, A.K., Putnis, A., Fitz Gerald, J.D., Austrheim, H., 2008. Albitization of granitic rocks: The mechanism of replacement of oligoclase by albite. Can. Mineral. 46, 1401–1415.
Errami, E., Linnemann, U., Hofmann, M., Gärtner, A., Zieger, J., Gärtner, J., Mende, K., El Kabouri, J., Gasquet, D., Ennih, N., 2021. From pan-african transpression to cadomian transtension at the west african margin: New U–PB zircon ages from the eastern saghro inlier (anti-atlas, Morocco). Geol. Soc. Spec. Publ. 503, 209–233.
Ersoy, Y., Helvaci, C., 2010. FC-AFC-FCA and mixing modeler: A Microsoft® Excel© spreadsheet program for modeling geochemical differentiation of magma by crystal fractionation, crustal assimilation and mixing. Comput. Geosci. 36, 383–390.

Eyüboğlu, Y., 2010. Late Cretaceous high-K volcanism in the eastern Pontide orogenic belt: Implications for the geodynamic evolution of NE Turkey. Int. Geol. Rev. 52, 142–186.
Faryad, S.W., Kachlík, V., 2013. New evidence of blueschist facies rocks and their geotectonic implication for Variscan suture(s) in the Bohemian Massif. J. Metamorph. Geol. 31, 63–82.
Faure, G., 1986. Principles of Isotope Geology.
Fediuk, F., 1992. Metaboninite in the Proterozoic Jílové Belt in Central Bohemia. Věstník českého Geol. ústavu 67.
Fediukova, E., Fediuk, F., 2000. Assemblages and chemical composition of amphiboles in rocks of the Jilove Belt, Central Bohemia. J. Czech Geol. Soc.
Fernández-Suárez, J., Gutiérrez-Alonso, G., Pastor-Galán, D., Hofmann, M., Murphy, J.B., Linnemann, U., 2014. The Ediacaran-Early Cambrian detrital zircon record of NW Iberia: Possible sources and paleogeographic constraints. Int. J. Earth Sci. 103, 1335–1357.
Fiala, F., 1987. Structures and textures of the Upper Proterozoic volcanics of the Barrandian area. Sborník Geol. věd 9–40.
Fiala, J., Henjes-Kunst, F., Müller-Sigmund, H., Vejnar, Z., 2014. Lithogeochemistry and Sr-Nd isotopic composition of Neoproterozoic metasedimentary rocks of the Teplá Crystalline Complex, western Bohemian Massif: A geotectonic interpretation. J. Geosci. (Czech Republic) 59, 293–311.
Foley, S.F., Barth, M.G., Jenner, G.A., 2000. Rutile/melt partition coefficients for trace elements and an assessment of the influence of rutile on the trace element characteristics of subduction zone magmas. Geochim. Cosmochim. Acta 65, 933–938.
Franke, W., 1989. Variscan plate tectonics in Central Europe-current ideas and open questions. Tectonophysics 169, 221–228.
Friedl, G., Finger, F., Paquette, J.L., von Quadt, A., McNaughton, N.J., Fletcher, I.R., 2004. Pre-Variscan geological events in the Austrian part of the Bohemian Massif deduced from U-Pb zircon ages. Int. J. Earth Sci. 93, 802–823.
Frost, B.R., Barnes, C.G., Collins, W.J., Arculus, R.J., Ellis, D.J., Frost, C.D., 2001. A geochemical classification for granitic rocks. J. Petrol. 42, 2033–2048.
Frost, C.D., Frost, B.R., Beard, J.S., 2016. On silica-rich granitoids and their eruptive equivalents. Am. Mineral. 101, 1268–1284.
Gao, S., Rudnick, R.L., Xu, W., Yuan, H., Liu, Y., Walker, R.J., Puchtel, I.S., Liu, X., Huang, H., Wang, X., Yang, J., 2008. Recycling deep cratonic lithosphere and generation of intraplate magmatism in the North China Craton. Earth Planet. Sci. Lett. 270, 41–53.
Gill, J.B., 1981. Orogenic Andesites and Plate Tectonics. Springer-Verlag.
Goldstein, S.L., Nions, R.K.O., Hamilton, P.J., 1984. A Sm-Nd isotopic study of atmospheric dusts and particulates from major river systems 70, 221–236.
Grove, T.L., Chatterjee, N., Parman, S.W., Médard, E., 2006. The influence of H2O on mantle wedge melting. Earth Planet. Sci. Lett. 249, 74–89.
Gürsu, S., Möller, A., Göncüoglu, M.C., Köksal, S., Demircan, H., Köksal, F.T., Kozlu, H., Sunal, G., 2015. Neoproterozoic continental arc volcanism at the northern edge of the Arabian Plate, SE Turkey. Precambrian Res. 258, 208–233.
Haase, K.M., Freund, S., Beier, C., Koepke, J., Erdmann, M., Hauff, F., 2016. Constraints on the magmatic evolution of the oceanic crust from plagiogranite intrusions in the Oman ophiolite. Contrib. to Mineral. Petrol. 171, 1–16.
Hajná, J., Žák, J., Ackerman, L., Svojtka, M., Pašava, J., 2019. A giant late Precambrian chert-bearing olistostrome discovered in the Bohemian Massif: a record of Oceanic Plate Stratigraphy (OPS) disrupted by mass-wasting along an outer trench slope. Gondwana Res. in print.
Hajná, J., Žák, J., Dörr, W., 2017. Time scales and mechanisms of growth of active margins of Gondwana: A model based on detrital zircon ages from the Neoproterozoic to Cambrian Blovice accretionary complex, Bohemian Massif. Gondwana Res. 42, 63–83.
Hajná, J., Žák, J., Dörr, W., Kachlík, V., Sláma, J., 2018. New constraints from detrital zircon ages on prolonged, multiphase transition from the Cadomian accretionary orogen to a passive margin of Gondwana. Precambrian Res. 317, 159–178.
Hajná, J., Žák, J., Kachlík, V., 2014. Growth of accretionary wedges and pulsed ophiolitic mélange formation by successive subduction of trench-parallel volcanic elevations. Terra Nov. 26, 322–

Hajná, J., Žák, J., Kachlík, V., 2011. Structure and stratigraphy of the Teplá-Barrandian Neoproterozoic, Bohemian Massif: A new plate-tectonic reinterpretation. Gondwana Res. 19, 495–508.
Hawkesworth, C., Cawood, P., Kemp, T., Storey, C., Dhuime, B., Mazur, E., 2009. A Matter of Preservation. Science (80-.). 323, 49–50.
Hawkesworth, C., Cawood, P.A., Dhuime, B., 2019. Rates of generation and growth of the continental crust. Geosci. Front. 10, 165–173.
Hawkesworth, C., Turner, S., Peate, D., McDermott, F., Van Calsteren, P., 1997. Elemental U and Th variations in island arc rocks: Implications for U-series isotopes. Chem. Geol. 139, 207–221.
Hermann, J., Spandler, C., Hack, A., Korsakov, A. V., 2006. Aqueous fluids and hydrous melts in high-pressure and ultra-high pressure rocks: Implications for element transfer in subduction zones. Lithos 92, 399–417.
Hofmann, A.W., 1997. Mantle geochemistry: the message from oceanic magmatism. Nature 385, 219–229.
Holub, F. V., Cocherie, A., Rossi, P., 1997. Radiometric dating of granitic rocks from the Central Bohemian Plutonic Complex (Czech Republic): constraints on the chronology of thermal and tectonic events along the Moldanubian-Barrandian boundary. Earth Planet. Sci. 325, 19–26.
Horn, I., Rudnick, R.L., McDonough, W.F., 2000. Precise elemental and isotope ratio determination by simultaneous solution nebulization and laser ablation-ICP-MS: Application to U-Pb geochronology. Chem. Geol. 164, 281–301.
Horton, B.K., Hassanzadeh, J., Stockli, D.F., Axen, G.J., Gillis, R.J., Guest, B., Amini, A., Fakhari, M.D., Zamanzadeh, S.M., Grove, M., 2008. Detrital zircon provenance of Neoproterozoic to Cenozoic deposits in Iran: Implications for chronostratigraphy and collisional tectonics. Tectonophysics 451, 97–122.
Hrouda, F., Faryad, S.W., Kubínová, Š., Verner, K., Chlupácová, M., 2019. Simultaneous free flow and forcefully driven movement of magma in lamprophyre dykes as indicated by magnetic anisotropy: Case study from the central bohemian dyke swarm, Czech Republic. Geosciences 9.
Ilnicki, S., Szczepański, J., Pin, C., 2020. Tholeiitic- and boninite-series metabasites of the Nové Město Unit and northern part of the Zábřeh Unit (Orlica–Śnieżnik Dome, Bohemian Massif): petrogenesis and tectonic significance. Int. J. Earth Sci. 109, 1247–1271.
Ishikawa, T., Nagaishi, K., Umino, S., 2002. Boninitic volcanism in the Oman ophiolite: Implications for thermal condition during transition from spreading ridge to arc. Geology 30, 899–902.
Jackson, S.E., Pearson, N.J., Griffin, W.L., Belousova, E.A., 2004. The application of laser ablation-inductively coupled plasma-mass spectrometry to in situ U-Pb zircon geochronology. Chem. Geol. 211, 47–69.
Jacobsen, S.B., Wasserburg, G.J., 1980. Sm-Nd isotopic evolution of chondrites. Earth Planet. Sci. Lett. 50, 139–155.
Janoušek, V., Farrow, C.M., Erban, V., 2006. Interpretation of whole-rock geochemical data in igneous geochemistry: Introducing Geochemical Data Toolkit (GCDkit). J. Petrol. 47, 1255–1259.
Janoušek, V., Gerdes, A., 2003. Timing the magmatic activity within the Central Bohemian Pluton, Czech Republic: Conventional U-Pb ages for the Sázava and Tábor intrusions and their geotectonic significance. J. Czech Geol. Soc. 48, 70–71.
Jedlicka, R., Faryad, S.W., 2017. Felsic granulite with layers of eclogite facies rocks in the Bohemian Massif; did they share a common metamorphic history? Lithos 286–287, 408–425.
Jochum, K.P., Nohl, U., 2008. Reference materials in geochemistry and environmental research and the GeoReM database. Chem. Geol. 253, 50–53.
Kachlík, V., 1992. Litostratigraphy, paleogeography, and metamorphism of roof pendants in the NE part of the Central Bohemian Pluton. Charles University in Prague.
Kachlík, V., Heřmánek, R., Vítková, P., Janoušek, V., 1999. Petrology, Geochemistry and Palaeotectonic Setting of Metavolcanic Rocks at the Teplá-Barrandian-Moldanibian Boundary: Evidence from the NE Part of the lslet Zone. Central Bohemian Pluton. Geolines 8, 34–35.
Kay, R.W., 1978. Aleutian magnesian andesites: Melts from subducted Pacific ocean crust. J. Volcanol. Geotherm. Res. 4, 117–132.
Kelemen, P.B., Dick, H.J.B., Quick, J.E., 1992. Formation of harzburgite by pervasive melt/rock

reaction in the upper mantle. Nature 358, 635–641.
Kelemen, P.B., Hanghøj, K., Greene, A.R., 2003. One View of the Geochemistry of Subduction-Related Magmatic Arcs, with an Emphasis on Primitive Andesite and Lower Crust. Treatise on Geochemistry 3–9, 2–70.
Klaver, M., Lewis, J., Parkinson, I.J., Elburg, M.A., Vroon, P.Z., Kelley, K.A., Elliott, T., 2020. Sr isotopes in arcs revisited: tracking slab dehydration using δ88/86Sr and 87Sr/86Sr systematics of arc lavas. Geochim. Cosmochim. Acta 288, 101–119.
Koepke, J., Berndt, J., Feig, S.T., Holtz, F., 2007. The formation of SiO2-rich melts within the deep oceanic crust by hydrous partial melting of gabbros. Contrib. to Mineral. Petrol. 153, 67–84.
Košler, J., Fonneland, H., Sylvester, P., Tubrett, M., Pedersen, R.B., 2002. U-Pb dating of detrital zircons for sediment provenance studies - A comparison of laser ablation ICPMS and SIMS techniques. Chem. Geol. 182, 605–618.
Košler, J., Konopásek, J., Sláma, J., Vrána, S., 2014. U-Pb zircon provenance of Moldanubian metasediments in the Bohemian Massif. J. Geol. Soc. London. 171, 83–95.
Košler, J., Sylvester, P.J., 2003. Present trends and the future of zircon in geochronology: Laser ablation ICPMS. Zircon 53, 243–275.
Kříbek, B., Pouba, Z., Skoček, V., Waldhausrová, J., 2000. Neoproterozoic of the Teplá-Barrandian unit as a part of the cadomian orogenic belt: A review and correlation aspects. Věstník českého Geol. ústavu 75, 175–196.
Kröner, A., Hegner, E., Hammer, J., Haase, G., Bielicki, K.H., Krauss, M., Eidam, J., 1994. Geochronology and Nd-Sr systematics of Lusatian granitoids: significance for the evolution of the Variscan orogen in east-central Europe. Geol. Rundschau 83, 357–376.
Kroner, U., Romer, R.L., 2013. Two plates - Many subduction zones: The Variscan orogeny reconsidered. Gondwana Res. 24, 298–329.
Le Bas, M.J., Le Maitre, R.N., Streckeisen, A., Zanettin, B., 1986. A Chemical Classification of Volcanic Rocks Based on the Total Alcali-Silica Diagram. J. Petrol. 27, 745–750.
Le Maitre, R.W., Streckeisen, A., Zanettin, B., Bas, M.J. Le, Bonin, B., Bateman, P., Bellieni, G., Dudek, A., Efremova, S., Keller, J., Lameyre, J., Sabine, P.A., Schmid, R., Soressen, H., Woolley, A.R., 2002. Igneous Rocks a Classification and Glossary of Terms, Journal of Chemical Information and Modeling.
Leake, B.E., Woolley, A.R., Birch, W.D., Hawthorne, F.C., Kato, A., Kisch, H.J., Krivovichev, V.G., Petersburg, S., Linthout, R.K., LAmD, J., 1997. Nomenclature of Amphiboles: Report of the Subcommittee on Amphiboles of the International Mineralogical Association Commission on New Minerals and Mineral Names. Mineral. Mag. 61, 295–321.
Leat, P.T., Smellie, J.L., Millar, I.L., Larter, R.D., 2003. Magmatism in the South Sandwich Arc, in: Intra-Oceanic Subduction Systems: Tectonic and Magmatic Processes. Geological Society, London, pp. 285–313.
Liew, T.C., Hofmann, A.W., 1988. Precambrian crustal components, plutonic associations, plate environment of the Hercynian Fold Belt of central Europe: Indications from a Nd and Sr isotopic study. Contrib. to Mineral. Petrol. 98, 129–138.
Linnemann, U., Gerdes, A., Hofmann, M., Marko, L., 2014. The Cadomian Orogen: Neoproterozoic to Early Cambrian crustal growth and orogenic zoning along the periphery of the West African Craton-Constraints from U-Pb zircon ages and Hf isotopes (Schwarzburg Antiform, Germany). Precambrian Res.
Liu, L., Li, Y., Santosh, M., Yang, X., Hu, Q., Chu, G., 2018. Mesozoic High- and Low-SiO2 Adakites and A-Type Granites in the Lower Yangtze River Belt, Eastern China: Implications for Petrogenesis and Metallogeny. Minerals 8, 328.
Lugmair, G.W., Marti, K., 1978. Lunar Initial 143Nd-144Nd: differential evolution of the lunar crust and mantle 39, 349–357.
Ma, J., Tian, Y., Zhao, D., Liu, C., Liu, T., 2019. Mantle Dynamics of Western Pacific and East Asia: New Insights from P Wave Anisotropic Tomography. Geochemistry, Geophys. Geosystems 20, 3628–3658.
Maierová, P., Schulmann, K., Štípská, P., Gerya, T., Lexa, O., 2021. Trans-lithospheric diapirism explains the presence of ultra-high pressure rocks in the European Variscides. Commun. Earth Environ. 2, 1–9.

Martens, U., Weber, B., Valencia, V.A., 2010. U/Pb geochronology of devonian and older paleozoic beds in the southeastern maya block, central America: Its affinity with peri-gondwanan terranes. Bull. Geol. Soc. Am. 122, 815–829.
Martin, H., 1986. Effect of steeper Archean geothermal gradient on geochemistry of subduction-zone magmas. Geology 14, 753–756.
Martin, H., Smithies, R.H., Rapp, R., Moyen, J.F., Champion, D., 2005. An overview of adakite, tonalite-trondhjemiten-granodiorite (TTG), and sanukitoid: Relationships and some implications for crustal evolution. Lithos 79, 1–24.
Matte, P., 1991. Accretionary history and crustal evolution of the Variscan belt in Western Europe. Tectonophysics 196, 309–337.
Mazur, S., Kryza, R., Turniak, K., Bröcker, M., Pin, C., 2003. Pre-Variscan metaigneous rocks of the Kłodzko Metamorphic Complex - A vestige of Cadomian subduction in the Central Sudetes, SW Poland. J. Czech Geol. Soc. 48, 90–91.
Mazur, S., Turniak, K., Szczepański, J., McNaughton, N.J., 2015. Vestiges of Saxothuringian crust in the Central Sudetes, Bohemian Massif: Zircon evidence of a recycled subducted slab provenance. Gondwana Res. 27, 825–839.
McDonough, W. F., Sun, S. S., 1995. The composition of the Earth. Chem. Geol. 120, 223–253.
McInnes, B.I.A., Gregoire, M., Binns, R.A., Herzig, P.M., Hannington, M.D., 2001. Hydrous metasomatism of oceanic sub-arc mantle, Lihir, Papua New Guinea: Petrology and geochemistry of fluid-metasomatised mantle wedge xenoliths. Earth Planet. Sci. Lett. 188, 169–183.
Meng, F., Gao, S., Song, Z., Niu, Y., Li, X., 2018. Mesozoic high-Mg andesites from the Daohugou area, Inner Mongolia: Upper-crustal fractional crystallization of parental melt derived from metasomatized lithospheric mantle wedge. Lithos 302–303, 535–548.
Moghadam, H.S., Li, X.H., Santos, J.F., Stern, R.J., Griffin, W.L., Ghorbani, G., Sarebani, N., 2017. Neoproterozoic magmatic flare-up along the N. margin of Gondwana: The Taknar complex, NE Iran. Earth Planet. Sci. Lett. 474, 83–96.
Morávek, P., Röhlich, P., 1971. Geology of the northern part of the Jílové zone. Sborník Geol. věd 20, 101–141.
Morimoto, N., 1988. Nomenclature of Pyroxenes. Mineral. Petrol. 39, 55–76.
Mottl, M.J., Holland, H.D., 1978. Chemical exchange during hydrothermal alteration of basalt by seawater-I. Experimental results for major and minor components of seawater. Geochim. Cosmochim. Acta 42, 1103–1115.
Moyen, J.F., 2009. High Sr/Y and La/Yb ratios: The meaning of the “adakitic signature.” Lithos 112, 556–574.
Moyen, J.F., Martin, H., 2012. Forty years of TTG research. Lithos 148, 312–336.
Mráček, M., 2015. Vulkanity jihovýchodního křídla barrandienského neoproterozoika v okolí Dobříše. Univerzita Karlova.
Nance, D.R., Murphy, B.J., 2019. Supercontinents and the case for pannotia. Geol. Soc. Spec. Publ. 470, 65–85.
Nance, R.D., Gutiérrez-alonso, G., Keppie, J.D., Linnemann, U., Murphy, J.B., Quesada, C., Strachan, R.A., Woodcock, N.H., 2010. Evolution of the Rheic Ocean. Gondwana Res. 17, 194–222.
Nance, R.D., Linnemann, U., 2008. The Rheic Ocean: Origin, evolution, and significance. GSA Today 18, 4–12.
Nance, R.D., Murphy, J.B., Strachan, R.A., D’Lemos, R.S., Taylor, G.K., 1991. Late Proterozoic tectonostratigraphic evolution of the Avalonian and Cadomian terranes. Precambrian Res. 53, 41–78.
Nandedkar, R.H., Ulmer, P., Müntener, O., 2014. Fractional crystallization of primitive, hydrous arc magmas: An experimental study at 0.7 GPa. Contrib. to Mineral. Petrol. 167, 1–27.
Nguyen, Q.M., Feng, Q., Zi, J.-W., Zhao, T., Tran, H.T., Ngo, T.X., Tran, D.M., Nguyen, H.Q., 2019. Cambrian intra–oceanic arc trondhjemite and tonalite in the Tam Ky–Phuoc Son Suture Zone, central Vietnam: Implications for the early Paleozoic assembly of the Indochina Block. Gondwana Res. 70, 151–170.
O’Connor, J., 1965. A classification for quartz-rich igneous rocks based on feldspar ratios. US Geol. Surv. Prof. Pap. B 525, 79–84.
Pearce, J.A., 2014. Immobile element fingerprinting of ophiolites. Elements 10, 101–108.

Pearce, J.A., 1982. Trace Element Characteristics of Lavas from Destructive Plate Boundaries, in: Andesites. pp. 525–548.
Pearce, J.A., Peate, D.W., 1995. Tectonic implications of the composition of volcanic arc magmas. Annu. Rev. Earth Planet. Sci. 23, 251–286.
Pearce, J.A., Reagan, M.K., 2019. Identification, classification, and interpretation of boninites from Anthropocene to Eoarchean using Si-Mg-Ti systematics. Geosphere 15, 1008–1037.
Pearce, J.A., Stern, R.J., Bloomer, S.H., Fryer, P., 2005. Geochemical mapping of the Mariana arc-basin system: Implications for the nature and distribution of subduction components. Geochemistry, geophysics, geosystems, 6.
Phelps, D.A.V.I.D., Avé Lallemant, H.G., 1980. The Sparta ophiolite complex, northeast Oregon: a plutonic equivalent to low K2O island-arc volcanism. Am. J. Sci. 345–358.
Piccardo, G.B., Zanetti, A., Müntener, O., 2007. Melt/peridotite interaction in the Southern Lanzo peridotite: Field, textural and geochemical evidence. Lithos 94, 181–209.
Pin, C., Gannoun, A., Dupont, A., 2014. Rapid, simultaneous separation of Sr, Pb, and Nd by extraction chromatography prior to isotope ratios determination by TIMS and MC-ICP-MS. J. Anal. At. Spectrom. 29, 1858–1870.
Pin, C., Waldhausrová, J., 2007. Sm-Nd isotope and trace element study of Late Proterozoic metabasalts ("spilites") from the Central Barrandian domain (Bohemian Massif, Czech Republic). Geol. Soc. Am. Spec. Pap. 423, 231–247.
Price, R.C., Gamble, J.A., Smith, I.E.M., Stewart, R.B., Eggins, S., Wright, I.C., 2005. An integrated model for the temporal evolution of andesites and rhyolites and crustal development in New Zealand ' s North Island. J. of Volcan. 140, 1–24.
Pu, X., Brophy, J.G., Tsujimori, T., 2014. Rare earth element–SiO2systematics of island arc crustal amphibolite migmatites from the Asago body of the Yakuno Ophiolite, Japan: a field evaluation of some model predictions. Contrib. to Mineral. Petrol. 168, 1–12.
Qian, Q., Hermann, J., 2013. Partial melting of lower crust at 10-15 kbar: Constraints on adakite and TTG formation. Contrib. to Mineral. Petrol. 165, 1195–1224.
Rajlich, P., Schulmann, K., Synek, J., 1988. Strain analysis on conglomerates from the Central Bohemian Shear Zone. Krystalinikum 19, 119–134.
Rapp, R.P., Shimizu, N., Norman, M.D., Applegate, G.S., 1999. Reaction between slab-derived melts and peridotite in the mantle wedge: Experimental constraints at 3.8 GPa. Chem. Geol. 160, 335–356.
Reynard, B., 2013. Serpentine in active subduction zones. Lithos 178, 171–185.
Röhlich, P., 1998. The jílové belt: A neoproterozoic volcanic rift zone in Central Bohemia. Acta Univ. Carolinae, Geol. 42, 489–493.
Röhlich, P., 1972. Petrografické poměry v severní části jílovského pásma. Sborník Geol. věd 22, 7–64.
Rollinson, H., 2009. New models for the genesis of plagiogranites in the Oman ophiolite. Lithos 112, 603–614.
Rollinson, H.R., 1993. Using geochemical data: Evaluation, Prasentation, Interpretation.
Rudnev, S.N., Malkovets, V.G., Belousova, E.A., Tretiakova, I., Serov, P.A., Kiseleva, V.Y., Gibsher, A.A., Nikolaeva, I. V., 2020. Geochemistry, Sm–Nd, Rb–Sr, and Lu–Hf Isotopes, Sources, and Conditions of Formation of Early Paleozoic Plagiogranitoids in the South of the Lake Zone in Western Mongolia. Russ. Geol. Geophys. 61, 119–138.
Rudnick, R.L., Gao, S., 2014. Composition of the Continental Crust, 2nd ed, Treatise on Geochemistry: Second Edition. Elsevier Ltd.
Samson, S.D., Inglis, J.D., D'Lemos, R.S., Admou, H., Blichert-Toft, J., Hefferan, K., 2004. Geochronological, geochemical, and Nd–Hf isotopic constraints on the origin of Neoproterozoic plagiogranites in the Tasriwine ophiolite, Anti-Atlas orogen, Morocco. Precambrian Res. 135, 133–147.
Sawyer, Edward, W., 2008. Atlas of migmatites. NRC Research Press.
Schaltegger, U., Schmitt, A.K., Horstwood, M.S.A., 2015. U-Th-Pb zircon geochronology by ID-TIMS, SIMS, and laser ablation ICP-MS: Recipes, interpretations, and opportunities. Chem. Geol. 402, 89–110.
Schiano, P., Clocchiatti, R., Shimizu, N., Maury, R.C., Jochum, K.P., Hofmann, A.W., 1995. Hydrous, silica-rich melts in the sub-arc mantle and their relationship with erupted arc lavas. Nature 377.

Schulmann, K., Konopásek, J., Janoušek, V., Lexa, O., Lardeaux, J.M., Edel, J.B., Štípská, P., Ulrich, S., 2009. An Andean type Palaeozoic convergence in the Bohemian Massif. Comptes Rendus - Geosci. 341, 266–286.
Shukuno, H., Tamura, Y., Tani, K., Chang, Q., Suzuki, T., Fiske, R.S., 2006. Origin of silicic magmas and the compositional gap at Sumisu submarine caldera , Izu – Bonin arc , Japan 156, 187–216.
Sisson, T.W., Grove, T.L., 1993. Experimental investigations of the role of H2O in calc-alkaline differentiation and subduction zone magmatism. Contrib. to Mineral. Petrol. 113, 143–166.
Škácha, P., Goliáš, V., Sejkora, J., Plášil, J., Strnad, L., Škoda, R., Ježek, J., 2009. Hydrothermal uranium-base metal mineralization of the Jánská vein, Březové Hory, Příbram, Czech Republic: Lead isotopes and chemical dating of uraninite. J. Geosci. 54, 1–13.
Sláma, J., Dunkley, D.J., Kachlík, V., Kusiak, M.A., 2008. Transition from island-arc to passive setting on the continental margin of Gondwana: U-Pb zircon dating of Neoproterozoic metaconglomerates from the SE margin of the Teplá-Barrandian Unit, Bohemian Massif. Tectonophysics 461, 44–59.
Sobolev, A. V., Danyushevsky, L. V, 1994. Petrology and Geochemistry of Boninites from the North Termination of the Tonga Trench : Constraints on the Generation Conditions of Primary High-Ca Boninite Magmas. J. Petrol. 35, 1183–1211.
Soejono, I., Janoušek, V., Žáčková, E., Sláma, J., Konopásek, J., Machek, M., Hanžl, P., 2017. Long - lasting Cadomian magmatic activity along an active northern Gondwana margin : U – Pb zircon and Sr – Nd isotopic evidence from the Brunovistulian Domain , eastern Bohemian Massif. Int. J. EARTH Sci. 106, 2109–2129.
Spandler, C., Pirard, C., 2013. Element recycling from subducting slabs to arc crust: A review. Lithos 170–171, 208–223.
Stacey, J.S., Kramers, J.D., 1975. Approximation of terrestrial lead isotope evolution by a two-stage model. Earth Planet. Sci. Lett. 26, 207–221.
Steiger, R.H., Jäger, E., 1977. Subcommission on geochronology: Convention on the use of decay constants in geo- and cosmochronology. Earth Planet. Sci. Lett. 36, 359–362.
Sun, S.S., Nesbitt, R.W., Sharaskin, A.Y., 1979. Geochemical characteristics of mid-ocean ridge basalts. Earth Planet. Sci. Lett. 44, 119–138.
Syracuse, E.M., van Keken, P.E., Abers, G.A., Suetsugu, D., Bina, C., Inoue, T., Wiens, D., Jellinek, M., 2010. The global range of subduction zone thermal models. Phys. Earth Planet. Inter. 183, 73–90.
Tatsumi, Y., 2005. The subduction factory: How it operates in the evolving Earth. GSA Today 15, 4–10.
Teipel, U., Eichhorn, R., Loth, G., Rohrmüller, J., Höll, R., Kennedy, A., 2004. U-Pb SHRIMP and Nd isotopic data from the western Bohemian Massif (Bayerischer Wald, Germany): Implications for Upper Vendian and Lower Ordovician magmatism. Int. J. Earth Sci. 93, 782–801.
Thompson, M.D., Crowley, J.L., 2020. Avalonian arc-to-platform transition in southeastern New England: U-Pb geochronology and stratigraphy of Ediacaran Cambridge “argillite,” Boston Basin, Massachusetts, USA. Am. J. Sci. 320, 405–449.
Todt, W., Cliff, R.A., Hanser, A., Hofmann, A.W., 1996. Evaluation of a 202Pb - 205Pb Double Spike for High - Precision Lead Isotope Analysis. Geophys. Monogr. Ser. 95, 429–437.
Tollan, P.M.E., Dale, C.W., Hermann, J., Davidson, J.P., Arculus, R.J., 2017. Generation and modification of the mantle wedge and lithosphere beneath the West Bismarck Island Arc: Melting, metasomatism and thermal history of peridotite xenoliths from Ritter Island. J. Petrol. 58, 1475–1510.
Tomek, F., Žák, J., Chadima, M., 2015. Granitic magma emplacement and deformation during early-orogenic syn-convergent transtension: The Staré Sedlo complex, Bohemian Massif. J. Geodyn. 87, 50–66.
Vogt, K., Gerya, T. V., Castro, A., 2012. Crustal growth at active continental margins: Numerical modeling. Phys. Earth Planet. Inter. 192–193, 1–20.
Wada, I., Behn, M.D., Shaw, A.M., 2012. Effects of heterogeneous hydration in the incoming plate, slab rehydration, and mantle wedge hydration on slab-derived H 2O flux in subduction zones. Earth Planet. Sci. Lett. 353–354, 60–71.
Waldhausrová, J., 1984. Proterozoic volcanics and intrusive rocks of the Jílové zone in Central

Bohemia. Krystalinikum 17, 77–97.
Waldron, J.W.F., Schofield, D.I., Pearson, G., Sarkar, C., Luo, Y.A.N., Dokken, R., 2019. Detrital zircon characterization of early Cambrian sandstones from East Avalonia and SE Ireland: Implications for terrane affinities in the peri-Gondwanan Caledonides. Geol. Mag. 156, 1217–1232.
Wendt, I., Kroner, U., Fiala, J., Todt, W., 1993. Evidence from zircon dating for existence of approximately 2.1 Ga old crystalline basement in southern Bohemia, Czech Republic. Geol. Rundschau 82, 42–50.
White, C.E., Barr, S.M., Hamilton, M.A., Murphy, J.B., 2021. Age and tectonic setting of Neoproterozoic granitoid rocks, Antigonish Highlands, Nova Scotia, Canada: implications for Avalonia in the northern Appalachian orogen. Can. J. Earth Sci. 58, 396–412.
Wiedenbeck, M., Allé, P., Corfu, F., Griffin, W.L., Meier, M., Oborli, F., Quadt, A. VON, Roddick, J.C., Spiegel, W., 1995. Three Natural Zircon Standards for U-Th-Pb, Lu-Hf, Trace Element and Ree Analyses. Geostand. Newsl. 19, 1–23.
Wilson, M.B., 1989. Igneous petrogenesis, a Global Tectonic Approach. Springer Science & Business Media.
Winter, J.D., 2010. Principles of Igneous and Metamorphic Petrology.
Wood, B.J., Turner, S.P., 2009. Origin of primitive high-Mg andesite: Constraints from natural examples and experiments. Earth Planet. Sci. Lett. 283, 59–66.
Workman, R.K., Hart, S.R., 2005. Major and trace element composition of the depleted MORB mantle (DMM). Earth Planet. Sci. Lett. 231, 53–72.
Zachariáš, J., Morávek, P., Gadas, P., Pertoldová, J., 2014. The Mokrsko-West gold deposit, Bohemian Massif, Czech Republic: Mineralogy, deposit setting and classification. Ore Geol. Rev. 58, 238–263.
Zachariáš, J., Žák, K., Pudilová, M., Snee, L.W., 2013. Multiple fluid sources/pathways and severe thermal gradients during formation of the Jílové orogenic gold deposit, Bohemian Massif, Czech Republic. Ore Geol. Rev. 54, 81–109.
Žák, J., Dragoun, F., Verner, K., Chlupáčová, M., Holub, F. V., Kachlík, V., 2009. Forearc deformation and strain partitioning during growth of a continental magmatic arc: The northwestern margin of the Central Bohemian Plutonic Complex, Bohemian Massif. Tectonophysics 469, 93–111.
Žák, J., Holub, F. V., Verner, K., 2005a. Tectonic evolution of a continental magmatic arc from transpression in the upper crust to exhumation of mid-crustal orogenic root recorded by episodically emplaced plutons: The Central Bohemian Plutonic Complex (Bohemian Massif). Int. J. Earth Sci. 94, 385–400.
Žák, J., Schulmann, K., Hrouda, F., 2005b. Multiple magmatic fabrics in the Sázava pluton (Bohemian Massif, Czech Republic): A result of superposition of wrench-dominated regional transpression on final emplacement. J. Struct. Geol. 27, 805–822.
Žák, J., Sláma, J., 2018. How far did the Cadomian 'terranes' travel from Gondwana during early Palaeozoic? A critical reappraisal based on detrital zircon geochronology. Int. Geol. Rev. 60, 319–338.
Žák, J., Svojtka, M., Hajná, J., Ackerman, L., 2020. Detrital zircon geochronology and processes in accretionary wedges. Earth-Science Rev. 207, 103214.
Zartman, R.E., Doe, B.R., 1981. Plumbotectonics - the model. Tectonophysics 75, 135–162.
Zhang, X., Wilde, S.A., Zhang, H., Zhai, M., 2011. Early Permian high-K calc-alkaline volcanic rocks from NW Inner Mongolia, North China: Geochemistry, origin and tectonic implications. J. Geol. Soc. London. 168, 525–543.
Zhao, Y., Zheng, J., Xiong, Q., 2019. Zircon from Orogenic Peridotite: An Ideal Indicator for Mantle-Crust Interaction in Subduction Zones. J. Earth Sci. 30, 666–678.
Zheng, Y.F., 2019. Subduction zone geochemistry. Geosci. Front. 10, 1223–1254.